SM 87-13

DYNAMIC FRACTURE INITIATION AND PROPAGATION IN METALS: EXPERIMENTAL RESULTS AND TECHNIQUES

Thesis by
Alan T. Zehnder

In Partial Fulfillment
of the Requirements for the Degree of
Doctor of Philosophy

California Institute of Technology
Pasadena, California
1987

(Submitted May 22, 1987)

ACKNOWLEDGEMENTS

I would like to thank Professor Rosakis for giving me the opportunity to pursue this research, for the many hours he spent teaching me fracture mechanics, and for working with me closely on our research. I am grateful to Professor Knauss for the use of the high speed camera and other optics, and to Richard Pfaff for improvements to the high speed camera and advice on interferometry. To all my fellow graduate students in Solid Mechanics I am grateful and I would especially like to thank Sridhar Krishnaswamy who worked closely with me on several projects, and Dr. R. Narasimhan who provided me with the numerical results presented here. This research was carried out with the funding of the Office of Naval Research, Contract No. N00014-85-K-0596 and the National Science Foundation, Grant No. MSM-8451204. I am grateful to Caltech for a TRW Advanced Technologies Fellowship and for a Charles Lee Powell Fellowship. And I am especially grateful to my best friend Susan, my wife, for her support of my endeavors.

ABSTRACT

Dynamic fracture initiation and propagation in ductile and brittle materials was studied experimentally using the optical method of caustics in conjunction with high speed photography. The drop weight impact test, previously used only for studies of fracture initiation, was adapted to study both dynamic fracture initiation and dynamic fracture propagation.

The results show that for a relatively brittle, quenched and tempered, high strength 4340 steel the dynamic fracture propagation toughness depends on crack tip velocity through a relation that is a material property. In addition, the effect of stress waves on the dynamic response of different specimen geometries is discussed and the micromechanisms of failure for this heat treatment of 4340 steel are investigated.

Extension of the optical method of caustics to applications in elastic-plastic fracture was studied with the goal of learning how to measure dynamic fracture initiation toughness in tough, ductile materials. Static experiments were performed on different specimen geometries of a ductile 4340 steel and 1018 cold rolled steel, and were compared to small scale yielding, plane stress, finite element results. Issues studied that are related to the applicability of caustics are the extent of the dominance of the plane stress HRR field, the effect of plasticity on the accuracy of caustics from the elastic region outside the plastic zone, and the extent of the crack tip region of three dimensionality.

The above approach to caustics in ductile materials was based on the assumption of validity of the HRR field. A novel approach to the use of caustics with ductile materials was taken that eliminates the concerns over the region of dominance of the HRR field, etc. In this approach a calibration experiment was performed relating the caustic diameter to the J integral for a particular specimen geometry under conditions of large scale yielding. This approach was successfully applied to optically measure for the first time the J integral under dynamic loading. Measurement of the J integral by means of strain gages was developed and applied to obtain J simultaneously with the caustics measurement.

At the same time (and on the same specimens) additional measurements were made including, load, load-point displacement, strains near the crack tip and out of plane displacements (measured with interferometry). These results are compared with excellent agreement to a three dimensional finite element simulation of the specimen.

TABLE OF CONTENTS

LIST OF FIGURES

LIST OF TABLES

LIST OF SYMBOLS

Symbol	Description	Reference Eqn. No.
a	Crack length	
$\dot{a}$	Crack propagation speed	(2.12)
$\ddot{a}$	Crack propagation acceleration:Fig. 4.8	
b	Uncracked ligament length	Fig.4.8
c_1, c_2, c_3	Parameters for determination of crack speed	Sec. 3.4.1
C_l	Longitudinal wave speed	(2.16)
C_s	Shear wave speed	(2.16)
$C(\alpha_l)$	Function of crack speed	(2.18)
D	Caustic diameter	(2.6)
E	Modulus of elasticity	(2.5)
$E_{rr}, E_{\theta\theta}$	Dimensionless functions	(2.8)
$f(x_1, x_2)$	Shape of reflector surface	(2.1)
$F(\dot{a})$	Function of crack speed	(2.15)
h	Thickness of test specimen	(2.5)
I_n, S_n	Numerical factors dependent on n	(2.9, 2.10)
J	J integral	(2.9, 6.1)
J_{BC}	Static J integral evaluated from boundary conditions	Fig. 4.12
J_{caus}	Static J integral evaluated with caustics	Fig. 4.12
J_c	Critical fracture initiation value of J	
J_d	Dynamic J integral	(6.3)
K_{caus}	Static stress intensity factor evaluated from caustics	Fig. 4.11
K_{BC}	Static stress intensity factor evaluated from boundary conditions	Fig. 4.11
K_I	Mode-I (opening mode) stress intensity factor	
K_I^d	Dynamic stress intensity factor	(3.1)
K_{Ic}^d	Dynamic fracture toughness	(3.1)

K^d_{IIIc}	Dynamic fracture toughness for anti-plane shear crack growth	Fig. 3.1
n	Strain hardening exponent	(2.8)
P	Load	(4.1d)
P_o	Limit load	(4.1d)
r,θ	Polar coordinates	(2.5)
r_o	Initial curve radius	(2.7)
r_m	Characteristic distance behind crack tip	Fig. 3.2
r_p	Plastic zone size	Sec. 4.1.1
s	Distance between specimen supports	(3.3), Fig. 4.8
S	Optical path length	(2.1)
u_1,u_2	In plane displacements	Sec. 4.1
u_3	Out of plane displacement	(2.5)
w	Height of specimen ($w=a+b$)	(3.2, 3.3)
w	Strain energy density	(6.1)
x_1, x_2, x_3	Coordinate system in specimen	(2.1)
X_1, X_2, X_3	Coordinate system on reference plane	(2.1)
z_o	Distance from specimen to reference plane, or equivalently from specimen to plane of focus	(2.1)
α	Ramberg-Osgood material law parameter	(2.8)
α_l,α_s	Functions of crack speed and wave speed	(2.16)
γ_f	Critical plastic strain	Fig. 3.1
δ_c	Critical crack opening displacement	Fig. 3.2
$\underline{\varepsilon}, \varepsilon_{ij}$	Strain tensor	
ε_o	Yield strain	(4.1)
λ	Wavelength	Sec. 3.6, 5.1
ν	Poisson's ratio	(2.5)
$\underline{\sigma}, \sigma_{ij}$	Stress tensor	
σ_o	Yield stress in tension	(2.9)
τ	Natural period of oscillation	(3.3)
τ_o	Yield stress in shear	Sec. 4.1.1
ϕ	Diameter of initial crack tip	Fig. 3.12

Chapter 1

INTRODUCTION

Dynamic fracture mechanics is concerned with problems involving cracks in bodies when inertial or strain rate effects are important. This includes bodies with stationary cracks subjected to dynamic loading due to impact or explosions, and bodies containing rapidly propagating cracks subjected to static or dynamic loading. A rapidly propagating crack can be defined as one for which the propagation speed is greater than some fraction of the wave speed. Interest in dynamic fracture mechanics seems to be steadily increasing. Several recent journal issues and conferences were devoted exclusively to dynamic fracture [1,2,3].

For practical purposes the study of dynamic fracture is concerned with investigating fracture criteria, or critical fracture toughness values. There are questions regarding which criteria are applicable, and once a criterion is chosen, what are the critical values and how are they measured or computed. Toughness parameters of interest are criteria for predicting fracture initiation, fracture propagation and fracture arrest. On the road to determining these failure criteria many issues must be investigated such as experimental techniques, numerical models, crack tip stress and strain fields, stress-strain behavior of materials under high loading rates, material failure mechanisms and others.

One of the premises of fracture mechanics is that under the proper conditions, toughness results obtained from one structure or test specimen will apply to other structures to predict fracture behavior. Thus fracture toughness tests are usually performed on conveniently sized test specimens and the results are applied to larger structures. This is the approach taken here; all of the experiments used laboratory sized test specimens.

The experiments reported here were performed at room temperature with test specimens cut from flat plates. Various heat treatments of 4340 steel and a cold rolled 1018 steel were used. The optical method of caustics was used as the principal experimental tool. Caustics were applied to both static experiments and to dynamic experiments in conjunction with high speed photography. Additional techniques including interferometry and strain gages were also used. Some of this research was carried in parallel to a numerical study by Narasimhan [4]. Where applicable numerical results are included here and compared to experimental results.

In the first part of this thesis dynamic fracture propagation criteria are investigated by using established experimental techniques. In the second part new experimental techniques to measure fracture initiation criteria for dynamically loaded cracks are investigated.

The organization of this thesis is as follows: In Chapter 2 the method of caustics is reviewed up to the current state of the art. Only applications relevant to this thesis are discussed.

In Chapter 3 dynamic fracture initiation and propagation in an elastic material is investigated. The drop weight impact test was adapted for this purpose and is proposed as a new testing configuration for dynamic fracture propagation experiments. Also investigated were static approaches to dynamic fracture, fracture initiation and growth starting from a fatigue crack, study of the effect of stress waves generated by crack growth and a study of the micromechanisms of failure.

Chapter 4 investigates the application of caustics for measuring the intensity of the crack tip strains, the J integral [5], for plastically deforming materials. The motivation for this study was to learn when caustics can be accurately applied for this measurement. When this was known it was planned to apply caustics to measure J for dynamically loaded cracks. Related issues that were studied are the region of validity of the asymptotic stress and strain fields (the HRR field [6,7]) and the

effect of three dimensionality of the crack tip deformation field on the accuracy of the J measurement. The investigation was both experimental and numerical; where appropriate, results from both approaches are compared.

It was found that the original approach to caustics in ductile materials (Chapter 4) was not very useful for measuring the J integral, and thus in Chapter 5 a new approach was used with success. In this chapter both numerical and experimental results are presented for a statically loaded crack. Some additional experimental techniques and results using interferometry and strain gages are also presented.

In Chapter 6 the method of caustics as discussed in Chapter 5 is applied to measure the J integral under dynamic loading. Comparison is made to a technique based on strain gages. The limitations of this application of caustics are discussed by looking at results from some "unsuccesful" experiments.

Each chapter has a brief introduction and Chapters 2, 3, and 4 contain a review of papers and results that are relevant to these chapters. Portions of Chapters 3 and 4 are published elsewhere [8,9,10].

Chapter 2

THE OPTICAL METHOD OF CAUSTICS

A number of optical methods are available for the study of stress and strain fields in planar, deformable bodies. The most well known of these methods is photoelasticity. One of the least known is the method of caustics. Techniques such as photoelasticity yield information over any area of interest. The wealth of information such techniques produce tends to complicate the determination of parameters such as the stress intensity factor. The method of caustics, on the other hand, is usually specialized to investigating the fields near a crack tip and typically the determination of stress intensity factors or other strain concentration factors requires that only one measurement be made from the recorded optical patterns. For static experiments caustics has few advantages over traditional techniques, but for dynamic experiments caustics has many advantages. Thus caustics have mostly been applied to dynamic fracture mechanics.

Caustics were initially introduced by Schardin [11] and Manogg [12] and in recent years have been applied to a number of interesting fracture mechanics problems by a variety of investigators [13-17]. Manogg, who was the first to apply the technique quantitatively, used caustics in a transmission arrangement. He was able to record changes in the optical path of rays traveling through transparent material at the vicinity of a crack tip, where the elastic stress field introduces changes in the refractive index as well as changes of thickness. The resulting difference in optical path produces a caustic pattern on a screen placed behind the specimen. He showed that the geometrical characteristics of the caustic depend on the nature and intensity of the crack tip singularity and was able to measure the intensity of the near-tip, elastic stress field.

The method of caustics can be used in either a reflection or a transmission arrangement and thus can be applied to the investigation of both opaque and transparent materials. Manogg's result was later applied to the study of reflected caustics. His analysis, obtained on the basis of a transmission arrangement, was assumed to describe both transmission and reflection caustics. The adaptation of Manogg's equation for the reflection problem involved a number of simplifying assumptions [13,14] that are discussed in detail in [18].

In the following, attention is focused on the study of caustics obtained by reflection of parallel light rays from the mirrored surface of a solid, however the general concepts and analysis hold true for transmitted caustics as well.

2.1. General Principles.

Consider a initially planar body lying in the x_1,x_2 plane at $x_3=0$. The deformed configuration of the body is such that it causes a non-uniform change in the optical path of light transmitted through it, or reflected from its surface. For a transparent material the change in optical path is due to non-uniform changes in thickness of the body and also due to to gradients in the index of refraction of the material. For an opaque material the change in optical path is due to a non-uniform surface elevation of the body.

Consider further light travelling in the $-x_3$ direction normally incident on the body at $x_3=0$, as illustrated in Figure 2.1. This is equivalent to a family of plane waves incident on the body. A light ray is parallel to the vector normal to a surface representing wave fronts of light. If $S(x_1,x_2,x_3)$ represents the optical path of the light ray, then the wave front is given by $S(x_1,x_2,x_3)$ = Const. The vector $\underline{\nabla} S(x_1,x_2,x_3)$, where $\underline{\nabla}$ is the gradient operator, is then normal to S and thus parallel to the light ray passing through S at point (x_1,x_2,x_3). For a transparent material, the plane waves travel through the material and are distorted due to the introduced variations in optical path. This causes light rays passing through the body to be deflected. (Equivalently, waves reflected from the surface of an opaque solid are

distorted due to nonuniform surface elevation.) If a screen is placed at a distance z_o behind the medium, then the light ray intersecting the body at the point $\underline{x} = (x_1,x_2)$ will be mapped to a point $\underline{X} = (X_1,X_2)$ on the screen. The (X_1,X_2) coordinate system is identical to the (x_1,x_2) system, except that the origin of the former has been translated by $x_3 = -z_o$. Assuming that the body is of infinitesimal thickness, and using the geometry of Figure 2.2, the mapping is given by

$$\underline{X} = \underline{x} - z_o \left(\frac{\underline{\nabla} S(x_1,x_2,0)}{(\underline{\nabla} S(x_1,x_2,0),\underline{e}_3)} - \underline{e}_3 \right) , \tag{2.1}$$

where $\underline{e}_3$ is the unit vector along the x_3 axis, and $(\underline{\nabla} S,\underline{e}_3)$ denotes the scalar product of vectors $\underline{\nabla} S$ and $\underline{e}_3$.

2.1.1. *Caustics by Reflection.* It can be shown that for the specific case of light reflected from a body whose surface is specified by $x_3 = -f(x_1,x_2)$ the optical mapping is [18]

$$\underline{X} = \underline{x} - 2(z_o - f) \cdot \frac{\underline{\nabla} f}{1 - |\underline{\nabla} f|^2} \ . \tag{2.2}$$

The above expression describes the optical mapping of points (x_1,x_2) of the reflector on to points (X_1,X_2) of the "screen". The choice of the sign of z_o depends on whether the image is real or virtual. The use of a virtual image (positive z_o) and a reflection arrangement, is used in experiments on opaque solids.

When $z_0 \gg f$ as is usually the case in fracture mechanics experiments, the above mapping simplifies to [18]

$$\underline{X} = \underline{x} - 2z_o \underline{\nabla} f \ . \tag{2.3}$$

It is this simplified mapping that will be used for the rest of the analysis.

2.2. Application to Fracture Mechanics.

In fracture mechanics the principal application of the method of caustics is to the measurement of stress intensity factors in cracked, elastic bodies. Mode I and Mode II stress intensity factors may be measured for stationary or for propagating cracks under both static and dynamic loading conditions. A newer application of caustics is to the measurement of the J integral in elastic-plastic bodies. Measurement of the J integral is not a well established technique; much of this thesis is devoted to exploring this application of caustics.

To relate the observed caustic patterns to the crack tip stresses and strains the near crack tip fields must be known to within a scalar amplitude factor. For elastically deforming materials under Mode I loading this is done by assuming that the asymptotic, stress intensity factor field [19] (or K_I field):

$$\sigma_{ij} \rightarrow \frac{K_I}{\sqrt{2\pi r}} f_{ij}(\theta) , \quad r \rightarrow 0 ,$$

is valid over some finite region near the crack tip, where σ_{ij} are components of the stress tensor, r and θ are polar coordinates centered at the crack tip (see Figure 2.3) and f_{ij} is a dimensionless function of θ. The scalar amplitude factor in this case is the stress intensity factor K_I.

For monotonically loaded, stationary cracks in elastic-plastic materials it is assumed that the asymptotic, HRR field [6,7]

$$\sigma_{ij} \rightarrow \sigma_0 \left[\frac{JE}{\sigma_0^2 I_n r} \right]^{\frac{1}{n+1}} \Sigma_{ij}(n,\theta) , \quad r \rightarrow 0$$

is valid, where σ_0 is the yield stress in tension, I_n is a dimensionless numerical factor, and Σ_{ij} is a dimensionless function of strain hardening exponent, n, and θ. In this case the J integral is the amplitude factor of the near crack tip field. The

assumption of dominance of the HRR field turns out to be too restrictive for many situations, thus in this thesis an analysis based on a full field elastic-plastic solution will be presented. In addition, for both elastic and elastic-plastic cases plane stress conditions are assumed to prevail. The restrictions associated with this assumption are also explored.

Consider again a set of parallel light rays normally incident on a planar, reflective specimen as illustrated in Figure 2.3. The specimen surface was initially optically flat but it is deformed due to the tensile crack tip loading. The deformed shape of the specimen surface is such that the virtual extension of the reflected light rays forms an envelope in space as illustrated in Figure 2.4. This surface, called the "caustic surface" is the locus of points of maximum luminosity. Its intersection with a plane located a distance z_o behind the specimen is called the "caustic curve". This curve bounds a dark region, called the "shadow spot". By placing a camera in front of the specimen to collect the reflected light rays and by focusing the camera behind the specimen the caustic can be photographed. As discussed in [18] a caustic curve will exist if and only if the Jacobian determinant J of the mapping vanishes,

$$J(x_1,x_2,z_o) = \det\left[\frac{\partial X_\alpha}{\partial x_\beta}\right] = 0. \tag{2.4}$$

The locus of points on the specimen satisfying $J = 0$ is called the "initial curve". All points on the initial curve map onto the caustic curve. In addition all points inside and outside the initial curve map outside the caustic. Since the light that forms the caustic curve is reflected from the initial curve, essential information conveyed by the caustic comes from this curve only. Equation (2.4), defining the initial curve depends on z_o. Thus by varying z_o the initial curve position may be varied. If z_0 is large then the initial curve will be located far away from the crack tip. If z_o is small then the initial curve will be close to the crack tip.

2.2.1. *Elastic-Static Fracture.* When a thin, cracked plate deforms in a purely elastic manner or when small scale yielding conditions are satisfied and the initial curve is well outside the crack tip plastic zone the analysis of caustics based on the linear elastic K_I field may be used. In such cases the Mode-I, plane stress, out of plane displacement field is given by [19]

$$f = u_3 = \frac{-\nu h K_I}{E\sqrt{2\pi r}} \cos\frac{\theta}{2}, \tag{2.5}$$

where E is the elastic modulus, ν is Poisson's ratio, and h is the specimen thickness. By substituting equation (2.5) into equations (2.3) and (2.4) it is found that the caustic is an epicycloid and that K_I is related to the caustic diameter D (width of the caustic in the direction perpendicular to the crack line, see Figure 2.5) by [12,13]

$$K_I = \frac{ED^{5/2}}{10.7 z_o \nu h}. \tag{2.6}$$

The initial curve is circular and its radius r_o is

$$r_o = 0.316D = \left[\frac{3h\nu K_I z_o}{2\sqrt{2\pi}E}\right]^{2/5}. \tag{2.7}$$

In Figure 2.5 both theoretical and experimental examples of caustics for elastic materials are shown.

Plane stress is a key assumption in the analysis of caustics. It is known [20] that due to the three-dimensional nature of the near crack tip field, the initial curve radius r_o must satisfy $r_o > 0.5\,h$, where h is the specimen thickness, for the plane-stress analysis of caustics to be accurate. Figure 2.6 shows the error in K_I for stationary cracks as measured with reflected caustics, due to three-dimensional effects when $r_o < 0.5h$. The curve of Figure 2.6 was used as a correction for calculating K_I

when $r_o<0.5h$.

2.2.2. *Static Elastic-Plastic Fracture.* When the initial curve is within a region of dominance of the plane stress HRR field an alternate analysis of caustics must be used. For a material with a stress strain curve that may be described by the Ramberg-Osgood model

$$\frac{\epsilon}{\epsilon_o} = \frac{\sigma}{\sigma_o} + \alpha\left(\frac{\sigma}{\sigma_o}\right)^n, \tag{2.8}$$

where σ_o and ϵ_o are the yield stress and yield strain in tension, the asymptotic, out of plane displacement is given by [6,7]

$$u_3 = \frac{\alpha\sigma_o h}{2E}\left[\frac{JE}{\alpha\sigma_o^2 I_n r}\right]^{\frac{n}{n+1}}\left[E_{rr}(\theta,n) + E_{\theta\theta}(\theta,n)\right], \tag{2.9}$$

where E_{rr} and $E_{\theta\theta}$ are dimensionless functions of θ and n. Substitution of the above equation into equations (2.3) and (2.4) yields [21]

$$J = S_n \frac{\alpha\sigma_o^2}{E}\left[\frac{E}{\alpha\sigma_o z_o h}\right]^{\frac{n+1}{n}} D^{\frac{3n+2}{n}}, \tag{2.10a}$$

where S_n is a numerical factor dependent on n and given in Table 2.1. For a non-hardening material [22]

$$J = \frac{\sigma_o D^3}{13.5 z_o h}. \tag{2.10b}$$

The caustic for a hardening exponent of n=9 is shown in Figure 2.7. Figure 2.7a shows the predicted caustic and Figure 2.7b shows the caustic observed in an experiment. The plastic zone can be seen surrounding the caustic of Figure 2.7b

demonstrating that the caustic came from light reflected from within the plastic zone.

Unlike the elastic case the initial curve, sketched in Figure 2.8, is no longer circular; it depends on the hardening level of the material. The point on the initial curve that maps to the maximum value of X_2 on the caustic curve is located at an angle θ_{max} from the x_1 axis. Let the distance to this point from the crack tip be called r_o, the initial curve size. It is important to know the location of this point since it is mapped to the maximum diameter of the caustic, which is used in the interpretation of the results. It was shown in [23] that θ_{max} varies from 72^o to 56^o as n varies from 1 to ∞. For a power law hardening material [23]

$$r_o = \begin{cases} 0.385D & n=9 \\ 0.40D & n=50 \end{cases} . \tag{2.11}$$

Note that equations (2.5)-(2.11) are based on the assumption of the validity of particular asymptotic fields. In Chapter 4 an attempt is made to eliminate this restriction by constructing caustics based on a full field numerical solution.

2.2.3. *Elasto-Dynamic Fracture.* For a dynamically propagating crack in an elastic material under plane-stress conditions the asymptotic crack tip u_3 displacement field is given by [24]

$$u_3 = \frac{\nu h}{E} \frac{K_I^d}{\sqrt{2\pi r_I}} \cos\frac{\theta_I}{2} \cdot \frac{1}{F(\dot{a})} , \tag{2.12}$$

where K_I^d, the dynamic stress intensity factor, is the amplitude factor of the near tip fields,

$$r_l = \left[x_1^2+\alpha_l^2 x_2^2\right]^{1/2} \quad , \tag{2.13}$$

$$\theta_l = \tan^{-1}\frac{\alpha_l x_2}{x_1} \quad , \tag{2.14}$$

$$F(\dot{a}) = \frac{4\alpha_l\alpha_s-(1+\alpha_s^2)^2}{(1+\alpha_s^2)(\alpha_l^2-\alpha_s^2)}, \tag{2.15}$$

$$\alpha_{l,s} = \left[\ 1 - (\frac{\dot{a}}{C_{l,s}})^2\ \right]^{1/2}, \tag{2.16}$$

x_1,x_2 move with the crack tip, $\dot{a}$ is the crack propagation speed, and C_l and C_s are the longitudinal and shear wave speeds. By substituting the above into equations (2.3) and (2.4) one can determine the shape of the caustic and can relate K_I^d to the caustic diameter D. The relation is given by [17]

$$K_I^d = \frac{ED^{5/2}}{10.7 z_o \nu h}\cdot F(\dot{a})\cdot C(\alpha_l) \quad , \tag{2.17}$$

where

$$C(\alpha_l) = \frac{(6.8+14.4\alpha_l-2.6\alpha_l^2)}{18.6}. \tag{2.18}$$

The initial curve is very nearly circular and its radius is closely approximated by [13]

$$r_o = F(\dot{a})^{-2/5}\ \ r_o^{stat} \tag{2.19}$$

where r_o^{stat} is the radius of the initial curve for stationary cracks given by equation (2.7). As $\dot{a} \rightarrow 0$ equations (2.17) and (2.19) reduce to the caustics equations for stationary cracks. A set of caustics recorded during a dynamic crack propagation experiment is shown in Figure 2.9.

Table 2.1 Sn Values, Equation (2.9), from [21]

n	Sn
1	.0277
2	.0513
3	.0611
4	.0660
5	.0687
6	.0701
7	.0710
8	.0715
9	.0718
10	.0719
15	.0719
20	.0717
25	.0714

Chapter 3

DYNAMIC FRACTURE INITIATION AND PROPAGATION

To predict the history of fracture propagation and arrest in a structure some fracture criterion must be postulated and a means of determining whether this criterion is met must be available. For dynamic crack propagation under mode I small scale yielding conditions this can be done by equating the amplitude K_I^d of the crack tip stress field to a critical value K_{IC}^d, which is usually assumed to be a material property. The quantity K_{IC}^d represents the resistance of the material to crack growth and its magnitude is expected to depend on crack speed and on properties of the material.

The fracture criterion is thus assumed to be

$$K_I^d\Big(a(t),\dot{a}(t),P(t)\Big) = K_{IC}^d\Big(\dot{a}(t)\Big) \ , \tag{3.1}$$

where $a(t)$ is is the crack length, $\dot{a}(t)$ is the crack tip speed, and P(t) is a dynamic generalized load. The above hypothesis states that if the instantaneous value of the stress intensity factor K_I^d is set equal to the dynamic fracture toughness $K_{IC}^d(\dot{a})$, then the resulting differential equation is an equation of motion for the crack tip [25]. Fracture arrest is also covered by equation (3.1) since if at any time $K_I^d(t) < K_{IC}^{d(MIN)}$, where $K_{IC}^{d(MIN)}$ is the minimum value of $K_{IC}^d(\dot{a})$, then the crack will no longer propagate.

The stress intensity factor K_I^d is in principle calculable through a purely elastodynamic analysis. However, the dynamic fracture toughness cannot be determined purely by analysis and thus it must be determined by experiment or by micromechanical modelling of the fracture process [26]. Thus the goal of many dynamic fracture experiments is to measure K_{IC}^d in order to investigate the validity

of the criterion (3.1) and to determine the nature of the relation $K_{IC}^{d}(\dot{a})$ if one exists.

In typical laboratory test specimens K_I^d cannot be determined from analytical solutions; thus direct measurements of K_I^d or dynamic numerical analyses are needed in order to interpret dynamic fracture experiments. Direct measurements of K_I^d can be made using optical techniques such as photoelasticity, or caustics, combined with high speed photography. Both techniques have been proven to be reliable and through their application important results have been obtained. These optical methods do not depend on the specimen boundary conditions which are in general time dependent in a complicated manner.

The available experimental results for dynamic crack propagation in metals are very limited. Several investigators [27-29] have used combined experimental and numerical techniques in which the boundary conditions applied to the specimen are measured (or assumed) and the crack length versus time is measured. These measurements are used in conjunction with a dynamic numerical model to calculate $K_I^d(t)$. Direct optical measurements using caustics or photoelasticity, combined with high speed photography, have been used extensively for investigating crack growth in transparent materials [13,30,31]. However, few direct optical measurements have been performed on metallic fracture specimens. Photoelastic coatings [32] and the method of reflected caustics [17] have been used to study crack growth in double cantilever beam (DCB) specimens of 4340 steel. In both cases high dynamic effects due to reflected stress waves were present. Such effects are more pronounced in metallic specimens [33] and complicate the interpretation of experimental results. Thus no definitive statements regarding the existence of a unique K_{Ic}^{d} vs. $\dot{a}$ relation have yet been made for metals.

In this chapter dynamic fracture initiation and propagation experiments using the method of caustics are described. A new configuration for crack propagation experiments is used. This configuration, consisting of a three point bend specimen loaded in a drop weight tower, was found to produce repeatable and reliable results

without the problems caused by the strong dynamic effects present when testing wedge loaded double cantilever beam (DCB) specimens. A review of relevant results and issues is presented first and then the experiments are presented and discussed.

3.1. Review of K_{IC}^{d} *vs.* $\dot{a}$ Relationship and Data..

A student of fracture mechanics would be well justified in asking why should there be a relationship between the crack tip speed and the stress intensity factor. In the most simplistic terms one might say that if the stresses at the crack tip are higher then the crack should advance more rapidly. However this simple approach does not explain much. Many effects combine to determine the dynamic fracture behavior of a material. Some of the effects are the interaction of crack tip plasticity and inertia, strain rate sensitivity, and local heating at the crack tip.

For crack propagation in elastic-plastic solids under conditions of small scale yielding some theoretical speculations can be made about the nature of the dependence of the dynamic fracture toughness on crack tip speed. It can be argued from a purely intuitive point of view that in the fracture of rate independent elastic-plastic materials the plastic zone surrounding the crack tip will give rise to greater inertial forces as the speed of crack propagation increases and also that the effect will be much larger than in purely elastic materials. Approaching the problem from both an analytical and numerical point of view, Freund and Douglas [34] were able to study the steady state motion of antiplane shear cracks, (mode-III) propagating dynamically in an elastic, perfectly-plastic solid.

The results were concerned both with the full deformation field, which was determined by means of the finite element method, and with the deformation on the crack line within the active plastic zone, which was determined analytically. Although the full field numerical analysis was conducted under the asumption of small scale yielding, the analytical result did not depend on this restriction. The main observation on the strain distribution was that the level of plastic strain is

significantly reduced from its corresponding slow crack growth levels due to material inertia. If this result is combined with the requirement of a fixed level of plastic strain at a critical distance in front of the crack tip it can be expected that for crack growth to occur, the far field stress intensity factor would necessarily increase with increasing crack speed. To quantify this idea the remotely applied stress intensity factor was related to the plastic zone strain distribution through the full-field numerical solution. The result, displayed here in Figure 3.1, demonstrates the variation of K^d_{IIIc} with crack tip velocity. The parameters appearing in Figure 3.1 are the elastic shear wave speed C_s, the critical plastic strain γ_f, and the level of applied stress intensity K_{IIIc} required to satisfy the same fracture criterion for crack initiation in the same material.

With a similar view toward developing a theoretical relation between K^d_{Ic} and crack tip speed, Lam and Freund [26] analyzed the elastic-plastic, plane strain, Mode-I problem. In their work the stress intensity factor was related to the near tip crack opening displacement through a full field numerical solution. A critical crack tip opening angle growth criterion was imposed. As in the Mode III problem, the approach was based on the requirement that the same growth criterion can be applied to both initiation and to crack propagation in the same material. The results are presented here in Figure 3.2. The figure shows the variation of K^d_{Ic} / K_{Ic} with normalized crack speed for different values of the ratio δ_c / r_m where δ_c is the critical value of the crack opening displacement at a characteristic distance r_m measured from the crack tip along the crack faces. Figures 3.1 and 3.2 demonstrate $K^d_C(\dot{a})$ relationships that are very similar to experimental results.

The strain rates at the tip of a dynamically propagating crack are very high, perhaps 10^6 or 10^7/sec. [35]. Thus one expects strain rate sensitivity to affect dynamic fracture toughness. In an extension of the work of [34], Freund and Douglas [36] studied antiplane shear cracks in a rate sensitive material. It was found that "the influence of strain rate sensitivity is greatest at the lower crack speeds, where the influence of inertia is least." At higher crack speeds the toughness continues to

increase but not as rapidly as for the rate independent material.

Using a rate sensitive constitutive model of a different type than [36], Freund and Hutchinson [35] investigated dynamic propagation of a tensile crack. For the material model used it was shown that the elastic strain rates dominate near the crack tip. Thus the near crack tip field has the same $r^{-1/2}$ singularity as an elastic material, but with a different amplitude factor, denoted in [35] by K_{tip}. The fracture toughness, expressed in terms of energy release rate, has a minimum value at some crack speed greater than zero. This is very different from the corresponding rate insensitive results. At higher crack speeds the toughness increases sharply with increasing crack speed, similar to the rate independent materials. Again it is seen that the strain rate effects are most important at low crack speeds.

A third potentially important effect on dynamic fracture toughness is local heating at the crack tip due to the high rate of plastic work occuring there. Although there exist no good measurements of the temperature rise some analytical estimates place the maximum rise at 400°C [37] to 1000°C [38] for dynamically propagating cracks under small scale yielding conditions. Materials are generally tougher at higher temperatures, thus the crack tip heating may contribute to increasing the toughness with increasing crack speed.

Since cracks do not always propagate under steady state conditions, other inertial effects not taken into account in the analyses of [26,34-36] might be important. A set of experiments were recently performed by Brickstad [27] to investigate whether K_{IC}^{d} depends on the crack tip acceleration, $\ddot{a}$ as well as $\dot{a}$. By using a stretching screw on the side of the specimen away from the machined precrack, an initially increasing and subsequently decreasing K field was obtained. This produced both acceleration and deceleration phases of crack growth and allowed the study of the sensitivity of the dependence of the fracture toughness on $\ddot{a}$. Results from a single specimen are presented in Figure 3.3 where both K_{I}^{d} and $\dot{a}$ are given as functions of crack length. As is obvious from this figure, the crack tip velocity

and K_I^d vary in phase both in the acceleration and deceleration regimes of the crack growth history, clearly indicating a relation between the two quantities. To demonstrate this more clearly, the collective data from many specimens are presented in Figure 3.4 where a clear relation between K_{Ic}^d and $\dot{a}$ is indicated while no dependence on acceleration is observed.

Additional confidence in the existence of a unique K_{Ic}^d vs. $\dot{a}$ relation in steel is obtained by Kanazawa et al. [28]. They performed experiments using both DCB and large single edge notched (SEN) specimens subjected to uniform tension. The crack tip position was recorded by the use of gages spaced 3 cm apart. This information produced an *average* velocity record that was used in conjunction with a dynamic finite difference code. By computing the energy variation, the dynamic energy release rate was obtained by a global energy balance in the specimen. Of particular interest are results corresponding to SEN specimens tested with a linear temperature gradient varying from -100^oC on one side to $+50^oC$ on the other, the temperature increasing with crack length. As the crack propagated into the higher temperature region it decelerated and eventually stopped. The family of K_{Ic}^d vs. $\dot{a}$ relations presented in Figure 3.5a, corresponding to different temperatures, can explain the observed deceleration behavior of the cracks. The fracture toughness $K_{Ic}^d(\dot{a})$ increases with temperature (and hence crack length in these tests), however the stress intensity factor K_I^d available was nearly constant, thus to satisfy equation (3.1) the crack must slow down until $K_{Ic}^d(\dot{a}) = K_I^d$. Cumulative results for -40^oC are given in Figure 3.5b. Although the results of Figure 3.5 may seem convincing, a close examination of Figure 3.5a reveals a very imaginative use of lines to "connect" the experimental data.

Behavior very similar to the above was also reported by Bilek [29] who performed tests with DCB specimens of 4340 steel. Despite the large scatter due to the many different tests being presented, the variation of K_I^d with crack tip speed, illustrated here in Figure 3.6 follows the same trend as in [17] and [27] and compares well with the superimposed results of Hahn et al. [39] and Angelino [40].

Kobayashi et al. recently performed some experiments on small specimens of 4340 steel [41]. In their paper $K_{IC}^{d}(\dot{a})$ results are reported that are very similar to those in Figures 3.5 and 3.6.

Birefringent coatings were first used in the study of the dynamic fracture of steel by T. Kobayashi and Dally [30]. As discussed in their work, the use of a single coating covering the surface of the metal specimen raises questions concerning the relative position of the crack tip in the plastic coating and in the metal specimen. However, they overcame this problem by cementing a pair of coatings to the surface of the grooved 4340 steel specimen, one on either side of the groove. As the crack advanced, using a Cordin high-speed framing camera, they recorded the isochromatic patterns, from which they calculated the stress intensity as a function of time. They were also able to determine crack length and hence the crack velocity at each position. The results indicate large oscillations in the value of K_I^d corresponding to abrupt changes in the crack tip velocity. As discussed in detail in [33], the oscillations in K_I^d and in crack speed are in phase and are caused by the interaction of reflected stress waves with the propagating crack tip. Results from three different specimens are presented in Figure 3.7 where the variation of K_{Ic}^{d} with $\dot{a}$ is illustrated. The results follow the same qualitative trend of those reported by Bilek for a similar heat treatment of the 4340 steel. The specimen labeled 375 gave anomalous results, which were attributed by the authors to a different heat treatment.

The method of caustics was first applied to the study of the arrest process in high-strength steels, by Beinert and Kalthoff [13], but a relation between K_{Ic}^{d} and $\dot{a}$ was not reported. More recently Rosakis, Duffy, and Freund [17] used reflected caustics to study the dynamic behavior of cracks propagating rapidly in double cantilever beam specimens of 4340 steel. The caustic patterns formed during the course of the experiments were recorded by means of a high speed camera of the Cranz-Schardin type. The instantaneous value of the dynamic stress intensity factor and the crack tip position were thus recorded. The results of the experiments

indicate that the dynamic fracture toughness is an increasing function of crack tip speed.

Despite the results, both experimental and analytical that support a $K_{IC}^{d}(\dot{a})$ material property there is still much debate and doubt about this issue. The experiments are difficult to perform and analyze and many of the results may be questioned for one or more reasons. Indeed some recent papers [42,43] investigating crack growth in steel would lead one to say that there is no $K_{IC}^{d}(\dot{a})$ relation. But these results can also be questioned due to the choice of specimen configuration as well as measurement and analysis techniques.

The question of $K_{IC}^{d}(\dot{a})$ relations is of more than academic interest. Attempts are currently being made to apply dynamic fracture mechanics to the prediction of crack growth and arrest in critical applications such as nuclear power plants [44]. For the very ductile materials used in power plant piping $K_{IC}^{d}(\dot{a})$ is not likely to be an applicable criterion. However, if a single parameter criterion such as $K_{IC}^{d}(\dot{a})$ cannot be used sucessfully in linear elastic fracture mechanics, it is unlikely that a similar simple criterion will be useful for more complicated cases.

In this chapter an experiment is presented where many of the complications of previous experiments are eliminated. Thus the results have a high degree of reliability. The data presented here do support a $K_{IC}^{d}(\dot{a})$ relationship, however since they were obtained for a particular specimen geometry one can question whether these results are enough to demonstrate a unique $K_{IC}^{d}(\dot{a})$.

3.2. Description of Experiments.

The experimental apparatus, consisting of a drop weight tower, digital recording oscilloscope, pulsed laser, and high speed camera is sketched in Figure 3.8.

The specimen size was 30.4 $\times$ 12.8 $\times$ 0.95 cm with an initial crack length of 3.73 cm. The crack tip notch diameter was 0.3 mm for specimens 36, 37, and 39, and 1.4 mm for specimens 33, 34, and 38. One surface of the specimen was ground, lapped,

polished to a mirror finish, and vacuum coated with aluminum. The aluminum coating is an optional step but it increases the reflectivity by 50%. The material composition and properties are given in Table 3.1. The uniaxial tension stress-strain curves for the heat treatment of 4340 steel used in this chapter and for other heat treatment used in this thesis are given in Figure 3.9. This heat treatment of 4340 steel fractures in a relatively brittle manner, but not without some plastic deformation prior to fracture. Thus it represents a model material for investigation of dynamic crack growth under small scale yielding conditions.

The test specimens were dynamically loaded in 3-point bending by a Dynatup 8100A drop weight tester. The drop weight is variable, from 1910 N to 4220 N (430 lb-950 lb) and the maximum impact velocity is 10 m/s (32 ft/s). In the present experiments the weight was 1910 N and the velocity was 5.0 m/s. The tup (impact hammer) is instrumented allowing the dynamic impact force to be recorded on a Nicolet 2090 digital oscilloscope.

Two LED-Photodiode switches mounted on the drop weight tower provide trigger signals for the camera and oscilloscope. A flag mounted on the falling weight interrupts the light going from the LED to the photodiode causing a trigger pulse. One switch is positioned so that it triggers when the tup hits the specimen. This signal triggers the oscilloscope and the pulsing of the laser. The camera's mechanical capping shutter must be open before the impact, thus a second switch is mounted higher on the tower to provide a trigger for the shutter 20 ms before impact.

The rotating mirror high speed camera can record 200 frames at up to 200,000 frames per second. Although it operates with an open shutter as a streak camera, discreet frames are obtained by pulsing the laser light source. Due to the short pulse width of the laser the exposure time of each frame is very short (15 ns), resulting in sharp photographs.

To photograph the caustics the camera is placed in front of the specimen to collect the reflected light and then focused at a distance z_o behind the specimen, i.e., focused on the reference plane of Figure 2.4. In all of these tests $z_0 \approx 2.5m$ was used. Photographs of the caustics as they appear directly on the film are shown in Figure 3.10. The sequence covers the entire test from the moment of impact, fracture initiation and fracture propagation. Selected photographs obtained from a single test are shown in Figure 3.11. The area covered by each frame is approximately $3\ cm \times 9\ cm$. The bright curve surrounding each shadow spot is the caustic curve. Taking the moment of impact as $0\ \mu s$, it is seen that from $42\ \mu s$ to $252\ \mu s$ the shadow spot grew indicating that K_I was increasing. At $259\ \mu s$ the crack began to propagate. The shadow spot moves with the crack tip, thus by measuring the location of the shadow spot the crack length may be determined. As the crack propagates it leaves behind a wake of plastic deformation causing the tail-like shadow patterns seen in the figure.

3.3. Dynamic Crack Initiation.

Instrumented drop weight testing can be used to determine the energy absorbed by a material prior to fracture or to determine the dynamic fracture initiation toughness K_{Ic}^d.

The records of two impact tests are shown in Figure 3.12. Specimen 34 had a crack tip diameter of 1.4 mm and specimen 36 had a diameter of 0.3 mm. The true stress intensity factors, measured from caustics are presented along with the stress intensity factors calculated by using the dynamic tup load P(t) in a statically derived formula [45]

$$K_I(t) = P(t)\frac{3s}{2w^{3/2}}\ f(a/w), \qquad \textit{where}\quad f(0.3) = 0.95, \tag{3.2}$$

s = distance between supports, w = height of specimen, and a = crack length. In these tests a/w=0.3 and s/w=2.4. The caustics results are only given up to the time

of fracture initiation. Thus from the figure it is seen that the specimen with a blunted crack fractured at t=640μs and that the sharper specimen fractured at t=240μs. Up to the time of initiation for specimen 36, the $K_I^d(t)$ records for both tests are nearly identical demonstrating the repeatability of the test. It is seen from the caustics records that the crack tip does not begin to be loaded until 40 μs after impact, approximately the minimum time it takes for stress waves generated by the impact to reflect from the specimen boundaries to the crack tip. This point is also demonstrated in Figure 3.11 where it is seen that at 42 μs a caustic is just starting to appear indicating that the crack is being loaded.

It was proposed in [46] that if the time to fracture, t_f, is large enough, $t_f > 3\tau$, where τ is the natural period of oscillation of the specimen, then $K_I^d(t)$ may be calculated from equation (4.2). The critical initiation value of K_{Ic}^d is then assumed to be the value corresponding to the maximum load. The period τ can be calulated approximately by using the empirical formula [47]

$$\tau = \frac{1.68(swhCE)^{1/2}}{C_0} \quad , \tag{3.3}$$

where s is the support span, w is the specimen width, h is the thickness, C is the specimen compliance, and C_0 is the bar wave speed, 5000 m/s for steel. For these specimens the period τ was approximately 180μs, or 3τ=540μs. Figure 3.12 shows that throughout the tests, even for $t > 3\tau$, K_I^d from caustics and from the tup load do not agree. Equivalent results were reported by Kalthoff et al., [48,49], who made more extensive tests with metals and polymers. Note that $K_I^d(t)$ from caustics has oscillations that have a period near the calculated period of the specimen, showing that the oscillations are due in part to vibrations of the specimen.

Figure 3.12 also shows that fracture initiation occurs about 60μs prior to the time of peak load. By studying the crack propagation record it was found that the load began to drop rapidly at the time when the crack had propagated almost

completely through the specimen. Thus the peak load is associated not with fracture initation but with fracture completion.

The energy absorbed by the specimen prior to fracture can be calculated by integrating the load-displacement record up to the time of peak load. In the experiments presented here the energy of the falling weight was large enough so that the weight moved with very nearly constant velocity during impact. As a result, the load-time record, P(t), also corresponds to a load-displacement record. Integration of the record for specimen 36 shows that the energy absorbed by the time of peak load ($300\mu s$) is 25% greater than the energy absorbed at the actual time of fracture ($240\mu s$). For the blunted specimen 34, the relative difference between t_f ($640\mu s$) and the time of peak load ($700\mu s$) is smaller, but the absorbed energy is still overestimated by 10%.

As is clear from the above, calculation of fracture toughness by means of impact load measurements and static analyses results in serious errors. Alternatives to optical techniques require complete determination of the boundary conditions (including supports) and the use of a fully elastodynamic analysis.

3.4. Dynamic Crack Propagation.

3.4.1. *Results.* The crack length a(t), crack tip speed $\dot{a}(t)$, and $K_I^d(t)$ records for a typical test (specimen 34) are given in Figures 3.13 and 3.14. The crack length record is differentiated using the incremental polynomial fit method described in the ASTM Test for Constant-Load-Amplitude Fatigue Crack Growth Rates above 10^{-8} m/cycle (E647-81). To find the velocity at data point $a(t_i)$, a curve $a=C_1+C_2t + C_3t^2$ is least squares fit to points $\{a(t_{i-m}), \ldots a(t_i), \ldots a(t_{i+m})\}$ where m is usually 1,2, or 3. The crack tip velocity is then $\dot{a}(t_i)=C_2+2C_3t_i$. It is clear that this method cannot be used on the first and last data points; thus a graphical method was used for those points.

If a(t) is such that different differentiation techniques produce widely different $\dot{a}(t)$ records then the results are subject to interpretation. In Figure 3.14 $\dot{a}(t)$ for 5 point (m=2) and 3 point (m=1) fits are compared. It is seen that fitting more points results in more smoothing but the two $\dot{a}(t)$ records differ by less than 5% indicating that in this example $\dot{a}(t)$ is relatively insensitive to differentiation technique.

The smooth velocity record gives confidence in these results because it shows that such records are not as subject to interpretation as are similar results for DCB specimens. As discussed in [50] and in section 3.4.3 changes in $\dot{a}$ in DCB specimens may occur on time scales smaller than the measurement interval causing the interpretation of the data to be rather subjective.

Note that the $K_I^d(t)$ and $\dot{a}(t)$ records vary in phase in Figure 3.14 demonstrating a strong relation between K_I^d and $\dot{a}$. Cross plotting of the results of Figure 3.14 produces the relation between K_{Ic}^d and $\dot{a}$ shown in Figure 3.15 The error bars in the figure indicate the uncertainty in the experimental data. See Appendix A for details of the uncertainty analysis.

The consistency of the present tests is illustrated in Figure 3.16 where $\dot{a}(t)$ and

$K_I^d(t)$ are shown for specimens 33 and 34, identical blunted crack tip specimens. Due to a small difference in the initial crack tip conditions the cracks initiated at slightly different times (time difference= 45 μs) and slightly different levels of K_I^d. Even so, the results of the two tests generally agree, demonstrating the reproducibility and reliability of these tests. As before, $\dot{a}(t)$ and $K_I^d(t)$ vary in phase.

The effect of the crack tip bluntness on stress intensity factor and velocity history is demonstrated in Figures 3.12, 3.13, and 3.17 where the results for specimens 34 and 36 are compared. The initial crack tip diameter was 1.4 mm for specimen 34 and 0.3 mm for specimen 36. Figure 3.13 demonstrates that by increasing the crack bluntness the average crack velocity is increased. Similarly Figure 3.17 demonstrates that higher levels of K_I^d may be obtained by blunting the crack. Generally the specimens containing sharp initial crack tips fractured with velocities in the range of 600-800 m/s. To cover a higher velocity range the blunted specimens were tested, fracturing with velocities of 800-1200 m/s.

3.4.2. K_{IC}^d versus $\dot{a}$ Relation. The relation between K_{Ic}^d and $\dot{a}$ for a single experiment (specimen 34) is shown in Figure 3.15. Figure 3.15 suggests a clear dependence of K_{Ic}^d on crack tip velocity. The repeatability of such a result for different load and velocity histories is necessary for assuming that the dynamic fracture toughness depends on velocity through a relation which is purely a material property as is usually assumed for the right hand side of equation (3.1).

Repeatability is indeed demonstrated in the results of Figure 3.18. This figure displays the collective results from the present experiments. These results, which correspond to a variety of velocity histories, follow a definite trend. Superimposed are the results from [17] obtained from experiments performed on DCB specimens of the same material and heat treatment. The data point corresponding to specimen 32 ($\dot{a}$=0) is the value of steady state crack propagation toughness obtained from a quasistatic test.

Although this heat treatment of 4340 steel fractures under nominally elastic conditions, a plastic zone of 1-2 mm propagates with the crack tip and the fracture mechanism is a mix of ductile hole growth and cleavage fracture. (See sec. 3.7 for a discussion of the micromechanisms of the fracture.) Conditions of ductile fracture were simulated by the analysis of dynamic crack growth given in [26] where the existence of a K_{Ic}^{d} vs. $\dot{a}$ relationship is demonstrated. Note that experiments performed on double cantiliever beam specimens of a similar 4340 steel [29,32] produced K_{Ic}^{d} versus $\dot{a}$ relations qualitatively similar to the results obtained here. This agreement of results from different sources and specimen configurations provides strong evidence for the existence of a unique $K_{Ic}^{d}(\dot{a})$ relationship for this steel. However, for materials that fracture in a truly brittle manner where the micromechanism of fracture is pure cleavage, the results of [26] do not necessarily apply and the existence of a $K_{Ic}^{d}(\dot{a})$ relationship has been questioned [31].

3.4.3. *Comparison with DCB Tests.* Most of the previous dynamic crack propagation tests in metals were performed with compact tension or double cantilever beam (DCB) specimens [17,29,32,51,52]. The DCB specimen was often chosen for its relative ease of analysis by means of a dynamic beam model. However the small size of most DCB specimens results in undesirable dynamic effects. Due to the closeness of the specimen boundaries to the crack tip, stress waves released when the crack begins to propagate reflect back to the crack tip causing abrupt changes in $\dot{a}(t)$ and $K_I^d(t)$. Visual evidence of such reflected waves is seen in Figure 3.19. When the crack is initiated from a blunted notch the initial stress waves that are emitted are very strong. In the DCB specimen the initial surface waves reflect back to the crack tip distorting the caustic. The surface wave patterns suggest that body waves, which will affect K_I^d but cannot be detected by photography, are also present.

In preliminary experiments performed at Caltech on DCB specimens the dynamic effects and wave reflections were found to cause many difficulties in the interpreta-

tion of the results [50]. The problems were so great that DCB experiments were abandoned in favor of drop weight testing. Results from the DCB experiments are shown in Figure 3.20. In these tests the specimen size was 23 cm x 7.6 cm x 1 cm thick and the specimens were made of the same heat treatment of 4340 steel that the drop weight specimens were made of. The specimen had a blunted initial crack and was wedge loaded.

If the interval of measurement is not small enough, then large errors may result due to variations of crack tip speed on time scales smaller than the measuring interval. This can be expected to cause problems in small specimens where reflections of stress waves from the boundaries may cause abrupt changes in crack tip position. Consider the $a(t)$ records in Figure 3.20. For this record data were obtained every 7 μs. In Figure 3.20a a smooth curve is drawn through the points producing one $\dot{a}(t)$ record. In Figure 3.20b kinks are allowed in the $a(t)$ record at times where the first reflected stress waves arrive at the crack tip. This was done by fitting smooth curves to the left and right of the wave arrival time and then matching the curves at the wave arrival, allowing a discontinuity in slope. As can be seen the second interpretation produces a much different $\dot{a}(t)$ record. To resolve these differences the measuring intervals would need to be reduced to 1 or 2 μs, which is much faster than the capability of any existing high speed cameras that are suitable for caustics.

In contrast, the drop weight specimen has fewer undesired dynamic effects. The set of photographs from a drop weight test shown in Figure 3.11 shows only outgoing surface waves. Due to the longer lateral dimensions of the 3-point bend specimen, no strong reflected stress waves are seen interacting with the crack tip. In addition the results of Figures 3.13, 3.14, 3.16, and 3.17 show smoothly varying $\dot{a}(t)$ and $K_I^d(t)$ records making the interpretation of these results straightforward.

Another advantage of drop weight testing combined with high speed photography is that the time of fracture initiation can be found within 5 μs (time between frames = 5 μs). In DCB testing the data recording is triggered by the breaking of a trip wire glued on the specimen ahead of the crack. Thus data for the first part of propagation and for the initiation are lost. As is seen from Figure 3.11, the drop weight experiments combine the crack loading, initiation and propagation in a single test. Thus unlike the DCB specimen no data on crack initiation and on the beginning stages of crack growth are lost.

3.5. Initiation and Propagation from a Fatigue Crack.

In the previous sections tests were described of specimens with machined crack tips with diameters of 0.3 mm and 1.4 mm. These machined cracks were used to delay the onset of crack propagation until a time when the crack tip stresses had built up to a high enough level to cause the initially blunted crack to propagate very fast when it did initiate. In many situations of engineering importance a dynamically propagating crack is likely to start from a pre-existing flaw, surface crack, or fatigue crack. Since fracture propagation from sharp cracks is so important in practice a few tests were made to study dynamic fracture initiation and growth starting from a fatigued crack.

Two tests were made, using specimens 54 and 63. Due to some difficulties with the optical arrangement only partial results were obtained for specimen 54, thus the discussion here will concentrate on specimen 63. The dimensions of specimen 63 are the same as the previous specimens. The heat treatment and the fatiguing conditions are given in Table 3.2. Unfortunately when the series of experiments described in secs. 3.2-3.4 was completed all of the original hot rolled 4340 steel was used up. Thus a new order of 4340 steel was used in the tests described in this section. The new steel came in a cold-rolled condition and has important material property differences that make direct comparison of the results from specimens 54

and 63 to results from specimens 32-39 impossible.

The experiments were carried out under the same conditions as the tests described previously. The only differences were some improvements to the camera optics and a change in the specimen supports. The new specimen supports, which are instrumented with semiconductor strain gages to allow for measuremement of the support loads, are more compliant than the previous ones causing some slight changes in the loading history.

Some of the features of the crack tip loading may be deduced by examining results from different tests. In Figure 3.21 $K_I^d(t)$ is shown for three tests: specimen 34 (blunted specimen, old supports), specimen 60 (blunted specimen, new supports), and specimen 63 (fatigued specimen, new supports). The dimensions of each specimen were the same and all were tested with the same weight and impact speed. It was found that the $K_I^d(t)$ record for tests made with the more compliant supports deviated from the record for tests made with the old supports only after approximately 110 μs. In separate tests it was found that the support load is zero until approximately 110 μs. This shows that the initial response of the specimen does not depend on the supports, but once the supports start to exert a force on the specimen the response is affected; $K_I^d(t)$ increases more slowly when the more compliant supports are used. Further examination of Figure 3.21 shows that at 125 μs the fatigue crack results (specimen 63) begin to deviate from the blunted crack results. The crack length history, graphed in Figure 3.22, reveals the reason for this difference. The crack begins to propagate very slowly at 100 μs. As the crack length increases the compliance of the specimen increases. By 125 μs the crack has grown to .19 cm, enough to start to significantly decrease the specimen compliance, resulting in a lower rate of loading of $K_I(t)$.

The $K_I(t)$ record and the crack tip speed history are graphed as functions of crack length in Figures 3.23 and 3.24. Unlike cracks initiating from blunted notches

the crack initially propagates quasi-statically while the stress intensity factor increases to levels high enough to cause dynamic crack growth. It is seen that when K_I does reach high values, approximately 125 MPa$\sqrt{m}$ at a = 2 cm, the crack tip did not immediately begin to propagate rapidly, but accelerated from 100 m/s to 750 m/s during the interval from 2 cm to 4 cm. During this time K_I was nearly constant. This result is consistant with the horizontal portion of the $K_{IC}^d(\dot{a})$ relationship shown in Figure 3.18, where it is seen that $\dot{a}$ can increase up to approximately 800 m/s without a significant increase in K_I^d.

Observation of the fracture surface showed that the shear lips were relatively large during the period of slow crack growth. The shear lips were measured to determine their extent quantitatively. The fraction of the specimen surface covered by shear lips is shown in Figure 3.25. Comparison of Figures 3.23, 3.24, and 3.25 suggests that there may be a correlation between the shear lips, $\dot{a}$ and $\frac{K_I}{\sigma_0}$. Indeed a significant correlation was found between the shear lip fraction and the quantity $\frac{K_I^2/\sigma_0^2}{\dot{a}}$. (Correlation coefficient = .53 for 17 samples, indicates less than 1 in 50 chance of random relationship.) Experience with cracks initiated at high speeds from blunted notches of the same 4340 steel shows that the shear lips are smaller for fast crack growth. Since the size of the shear lips is roughly related to the ductility of the specimen, it seems that dynamic crack growth serves to restrict the amount of plasticity at the crack tip.

3.6. Stress Waves Emitted during Dynamic Crack Growth.

When a dynamically propagating crack is initiated from a blunt notch, strong stress waves are released into the body. In addition to the body waves emitted, Rayleigh-like surface waves are emitted. If the crack propagated under steady state conditions no further stress waves will be emitted. However, fracture propagation in polycrystalline metals is never truly steady state, at least on the microstructural

scale. Thus in practice one may expect continuous stress wave emission as the crack propagates. In Figures 3.11, 3.12, and 3.19 many surface waves are visible during dynamic crack propagation. The surface waves are visible because the sharpness of the Rayleigh wavefronts produces large out of plane displacement gradients on the specimen surface causing the reflection of light from the waves to form caustics.

To be sure that the observed surface waves were Rayleigh waves the wavespeed and wavelength were measured. The measured surface wave speed was between 2800 m/s and 3100 m/s and the wavelength was $\lambda \approx 0.20$ *cm*. Note that the Rayleigh wave speed for steel is 2980 m/s and the shear wave speed is 3220 m/s. The wavelength λ was approximately 1/5 of the specimen thickness, small enough so that the surface wave speed is unchanged by the finite specimen thickness.

In dynamic fracture tests of transparent materials longitudinal waves as well as surface waves can be detected with the method of caustics. In experiments performed by Theocaris and Georgiadis [53] on PMMA, longitudinal waves were observed to be emitted only at the time of initiation of the crack from a notch. However, Rayleigh waves were emitted continously. The presence of Rayleigh waves suggests that body waves are present even though they were not observed in the PMMA experiments. The reason for this opinion is that the longitudinal wavefront is diffuse and thus if the stress wave is weak it is much harder to detect with caustics that are the sharp-fronted Rayleigh waves.

It is evident from the wave patterns seen in Figures 3.11 and 3.12 that the waves emitted after crack initiation are much weaker than the wave emitted at crack initiation. As discussed previously, in small specimens such as DCB specimens, stress waves reflected from the specimen boundaries interact with the crack causing difficulties in the experiments. Examination of Figure 3.19 shows that the reflection of the strong initiation stress wave is the one that gives the most problems. After

initiation, stress waves are emitted but they are weak enough so that their reflections are of less consequence in the interpretation of caustics.

3.7. Micromechanisms of Fracture.

In discussing dynamic fracture toughness results it is important to know some details of the mechanisms of fracture. As was suggested in [50], unique $K_{IC}^{d}(\dot{a})$ relationships may exist for materials that fracture in a small scale yielding, ductile manner but not for materials that are truly brittle. Thus, in this section the microstructure of the material and the failure mechanisms are investigated. Rate effects and the differences in toughness between two different heats of 4340 steel are also studied. Both scanning electron microscope (SEM) photographs of the fracture surface and optical micrographs of the material were examined.

The orientation of the samples cut from the test specimens is shown in Figure 3.26. Due to the high hardness of the material and the large test specimen size, difficulties were encountered in cutting the specimens into samples small enough to be examined. These difficulties were overcome by mounting a metallographic, abrasive cutoff wheel on a surface grinder in place of the grinding wheel. This allows cuts to be made over long lengths.

3.7.1. *Microstructure.* The samples used for the optical micrographs were mounted, polished to a 1/4 μm finish, and then etched in 5% Nitol. Two of the micrographs are shown in Figure 3.27. It is seen that the microstructure of this heat treatment of 4340 steel is martensitic. Comparing the micrographs from specimens 34 and 63 to each other it is seen that the microstructures of the two steels differ very little.

Although it is impossible to discern the grain boundaries from the photographs, the SEM photographs indicate that the grain diameters are 5-10 μm. Thus it was observed that the martensite plate lengths are of a subgrain size scale.

In several samples internal cracks perpendicular to the thickness direction of the plates (x_3 direction in Figure 3.26) were found. One of these cracks is shown in Figure 3.28. Since the plates were rolled, the planes parallel to the plate surface are weakened. In the interior of the plate, near the crack, tip the σ_{33} stress component is tensile and is approximately 1/3 the magnitude of the opening stress σ_{22} [54]. The combination of tensile stress in the thickness direction and of planes weakened by rolling allows the internal cracks to form.

3.7.2. *Scanning Electron Microscopy.* SEM photographs of the fracture surface were taken in order to investigate the micromechanisms of fracture for this particular steel. The photographs were examined to discern what are the differences between the two steels tested and whether there are any changes in the fracture surface due to differences in crack propagation speed.

Two of the SEM photographs are reproduced here in Figure 3.29. All of the photographs are from the flat fracture region. The shear lips look completely different; the failure there is ductile shearing.

For the tempered 4340 steel of Figure 3.29 the fracture is a mixture of cleavage and dimpled rupture. The areas of cleavage are the dark regions and the ductile areas are the light regions in the figure. Note that this is not pure cleavage, but is cleavage in the presence of and initiated by plastic deformation. It appears that the cleaved regions are linked by regions of ductile fracture; and that the cleaved regions are both transgranular and intergranular. Thus there is a mix of ductile and brittle mechanisms. This mix has been investigated extensively by previous authors [55-57]. In Figure 3.30 a chart is reproduced from [55] (original source is [56]) showing the percentage of fracture modes for 4340 steel. For the tempering temperature of 315^{0}C (600^{0}F) the room temperature fracture is described as 15% cleavage, 40% intergranular and 45% ductile. Note also that there is a decrease in the Charpy impact energy for tempering temperatures between 500^{0}F and 700^{0}F.,

showing that the steel tested here is in the temper embrittlement range. Although a quantitative analysis of the SEM photographs was not performed it appears that the percentage of dimpled rupture on specimen 34 (Figure 3.29a) is much less than 45%. However on specimen 63 (Figure 3.29b) the percentage of dimpled rupture may very well be close to 45%.

It appears that the micromechanisms of fracture are the same for the different 4340 steels of specimens 34 and 63. However the mix of ductile versus cleavage fracture is greater for the steel of specimen 63. The different mix of fracture modes is consistent with results that show that the steel of specimen 63 is as much as 50% tougher than the steel of specimen 34. The reasons for the diference in fracture modes between the two steels have not been established. However, surely the differences are not just random, but are related to the different chemical compositions and processing.

Note also that since much of the fracture is intergranular some individual grains may be discerned from the SEM photographs. In this way it was found the the grain diameters are on the order of 5-10 μm.

To determine if there are any rate effects on the fracture modes SEM photographs of surfaces that fractured with different crack speeds were examined. The speeds ranged from 0 to 1200 m/s. No significant differences were found between slow crack growth and fast crack growth surfaces even though the macroscopic fracture surface was always rougher for the fast crack growth regions.

3.8. Conclusions.

Dynamic fracture initiation and propagation in a high strength 4340 steel were investigated. The drop weight test, previously used only for fracture initiation studies, was adapted to study dynamic crack growth. This test produces reliable results and has many advantages over the commonly used DCB configuration. The results presented here support the existence of a unique $K_{IC}^{d}(\dot{a})$ relationship for

high strength steels. Unstable crack growth from a fatigue crack was found to start with slow (< 100 m/s) growth, then the crack accelerates to high speed (approx. 700 m/s). This is in contrast to cracks initiated from blunted notches that propagate very fast (> 1000 m/s) from the start. The micromechanism of fracture for this heat treatment of 4340 steel is a mixture of cleavage (mostly intergranular) and ductile modes. The ratio of the mix varied between two different batches of 4340 steel. The steel showing the higher mix of ductile fracture modes had a higher toughness.

Table 3.1. Material Properties 4340 Steel,
Aircraft Quality, Vacuum Degassed, Hot Rolled Annealed,
(Specimens 32-39)

Chemical Composition, %

C	Mn	P	S	Si	Ni	Cr	Mo	Cu	Fe
.39	.72	.015	.011	.21	1.87	.83	.25	.12	balance

Heat Treatment : 843°C 1 1/2 hour, oil quench
315°C 1 hour, oil cool.

Material Properties : Hardness = 50 HRC
Tensile Strength = 1490 MPa
Fracture Initiation Toughness, K_{Ic} = 47 MPa$\sqrt{m}$
Quasi-Static Propagation Toughness, K_I^* = 62 MPa$\sqrt{m}$
Stress-strain behavior is rate insensitive

Table 3.2. Specimen 63 Material Properties,
4340 Steel, Aircraft Quality, Vacuum Deoxidized, Cold Drawn

Chemical Composition, %

C	Mn	P	S	Si	Ni	Cr	Mo	Cu	Sn	Al	Fe
.42	.71	.007	.013	.23	1.78	.83	.25	.12	.005	.033	balance

Heat Treatment : $843^{o}C$ 1 1/2 hour, oil quench
$315^{o}C$ 1 hour, air cool.

Fatiguing : $K_{max} = 28\ \text{Mpa}\sqrt{m}$
$K_{min} = 2.8\ \text{Mpa}\sqrt{m}$
24 000 cycles
3 mm crack extension

Hardness : 49 HRC

Chapter 4

MEASUREMENT OF THE J INTEGRAL WITH CAUSTICS: SMALL SCALE YIELDING

In recent years the optical method of caustics has been developed into a very successful experimental tool for studying linear elastic fracture mechanics problems. The past success of caustics has led to efforts to extend the method to applications in elastic plastic fracture to measure the J integral, which characterizes the amplitude of the crack tip stress and strain fields and thus can be used as a fracture criterion.

Some preliminary work [21,22], based on the assumption of the validity of the plane stress, HRR, asymptotic crack tip field [6,7], demonstrated that the value of the J integral can be directly measured with caustics. Unfortunately the region of dominance of the plane stress HRR field has not been accurately established. Thus the conditions under which the analytical results reported in [21,22] and presented here in Chapter 2 are valid are uncertain. Experimental results given in [9,22,23,58] indicate that the method is promising and is worthy of further investigation.

Consider idealized small scale yielding conditions as depicted in Figure 4.1. Well outside the plastic zone, the elastic, singular stress field dominates. Inside the plastic zone, very near the crack tip, the HRR field dominates. In the transition region between these two fields no analytical solution is known. Thus no analysis of the method of caustics exists for initial curves originating from this region. This places certain limitations on the applicability of caustics. To quantify the limitations, the extent of dominance of the plane stress HRR field is studied numerically. In addition caustics based on the numerical results are introduced. These caustics are not limited by the assumption of a particular asymptotic field.

For caustics obtained from the elastic region surrounding the crack tip plastic zone, an analysis based on the linear elastic K_I field may be used. However crack

tip plasticity often affects caustics, causing errors in the measurement of K_I. The resulting errors are investigated here experimentally.

The analysis of the method of caustics applies to cracked, planar bodies that are thin enough so that the state of deformation is one of plane stress. However, there is a region near the crack tip where the deformation fields are three dimensional. Experiments were performed to investigate the extent of the region of three dimensional fields for plastically deforming materials, and to determine the effect of three dimensionality on the accuracy of the method of caustics as based on plane stress fields.

4.1. Numerical Calculations.

In numerical calculations performed by Narasimhan [4], [10] a semi-infinite crack under Mode-I, plane stress, small scale yielding conditions was modelled. The in plane displacements from the singular, elastic crack tip field

$$u_\alpha(r,\theta) = K_I \sqrt{\frac{r}{2\pi}}\ \hat{u}_\alpha(\theta)\ , \quad \textit{where} \quad \alpha = 1,2$$

were specified on a circle of radius of approximately 3400 times the the smallest element length. The maximum extent of the plastic zone was contained within 1/30 of this radius. An incremental J_2 plasticity theory was used. The material obeyed the Von Mises yield criterion and followed a piecewise power hardening law in uniaxial tension of the form

$$\frac{\epsilon}{\epsilon_o} = \begin{cases} \dfrac{\sigma}{\sigma_o} & \sigma \le \sigma_o \\ \left(\dfrac{\sigma}{\sigma_o}\right)^n & \sigma > \sigma_o \end{cases} \tag{4.1}$$

with hardening exponent n=9 and σ_0=830 MPa. These values were chosen to match

the 4340 steel used in the experiments.

4.1.1. *Results.* The calculated and experimentally observed plane stress, crack tip plastic zones are shown in Figure 4.2. A point was plotted for every element that had yielded, thus defining the calculated plastic zone in Figure 4.2a. Note that the density of points reflects only the density of the mesh near the crack tip. Figure 4.2b shows visual evidence of plastic deformation observed on the surface of a thin, compact tension specimen of 4340 steel with a hardening exponent of n=8.7. It is seen that the calculated and observed plastic zones agree in shape. Both calculations and experiment show that the extent of the plastic zone ahead of the crack tip is $r_p=0.25(K_I/\sigma_o)^2$.

The stress distribution σ_{22}/τ_o ahead of the crack is shown in Figure 4.3. The non-dimensionalization of x_1 by $(K_I/\sigma_o)^2$ is used because the plastic zone scales with this parameter. The computed stress agrees with the stresses of the plane stress HRR field to within 1% when $x_1 \leq 0.08(K_I/\sigma_o)^2$, i.e. $x_1 < 0.3 r_p$. In Figure 4.4 the plastic strain distributions $\epsilon^p_{22}/\epsilon_o$ and $\epsilon^p_{33}/\epsilon_o$ are compared to the strains predicted by the HRR solution. Again it is seen that the numerical results agree with the HRR field up to $x_1 \sim 0.3 r_p$. Of particular interest is the result for $\epsilon^p_{33}/\epsilon_o$ since this is related to the out of plane displacement, which is important to the method of caustics.

The stresses ahead of the crack are compared to the linear elastic K_I field in Figure 4.5. At the boundary of the plastic zone ($x_1=0.25(K_I/\sigma_o)^2$) σ_{22} begins to decrease rapidly, making a transition to the linear elastic solution as x_1 increases. It is seen that the linear elastic field agrees with the actual stress field when $x_1 \geq 1.5\ r_p$.

4.1.2. *Caustics Generated with Numerical Solution.* To provide a means to analyze caustics that is not dependent on the assumption of dominance of the HRR or K_I fields, caustics were generated using the results of the FEM analysis. The out of plane surface displacements were smoothed using a least squares scheme and

caustics were generated by mapping light rays point by point using equation (2.2) for different values of z_o. The caustics are shown in Figure 4.6 for values of r_o/r_p from 0.19 to 1.3. It is seen that for r_o/r_p=0.19 the numerically simulated caustic agrees in shape with the caustic predicted using the the HRR field, Figure 2.7. When r_o/r_p=1.3 the numerically simulated caustic, Figure 4.6f, agrees with the caustic predicted using the elastic, K_I field. In the region between r_o/r_p=.19 and 1.3 there is a transition from the "HRR like" caustic to the "elastic caustic". It is seen that for r_o/r_p as small as 0.30 (Figure 4.6b) the caustic shape deviates from the HRR shape.

4.2. Description of Experiments.

To experimentally determine the range of validity of the caustics measurements, the J integral (J_{caus}) or the stress intensity factor (K_{caus}) was measured with caustics using different initial curves. These quantities were simultaneously measured from the boundary conditions and are denoted by J_{BC} and K_{BC}. The values were then compared for different conditions.

The caustics were photographed using the apparatus illustrated in Figure 4.7. The system consisting of the lens and screen forms a telephoto camera that is focused on a virtual image plane at a distance z_o behind the specimen. Light reflected from the specimen forms a caustic on the screen which is then photographed with a 35 mm camera. Graph paper on the screen allows the magnification from the screen to the film to be determined and the thin lens equation is used to calculate the magnification from the virtual image plane to the screen. By varying the distance from the lens to the screen and by using different focal length lenses, the system can be focused at different distances z_o behind the specimen. Varying z_o varies the initial curve, allowing data to be obtained from different distances from the crack tip.

Note that to have large z_o one must make the distance from the lens to the screen small. In order to maintain a good magnification, a long focal length lens should be used when z_o is large.

The initial curve was calculated from the caustic diameter using equation (2.7) for $r_o > r_p$ and equation (2.11) for $r_o < r_p$. In transition regions where neither the HRR or the elastic field dominates, or in three-dimensional regions, these equations are approximate. However, r_o should always be bounded by the two values, 0.316D and 0.40D, (equations (2.7) and (2.11)) and thus any calculated value of r_o using these equations is approximately correct even in the transition regions.

For these tests, loading beyond relatively small scale yielding conditions was not applied. Thus only the applied load needed to be measured to determine J. Values of K_{BC} (and hence J_{BC}) were calculated using formulas given in [59] of the form

$$K_I = f\,(P, a_e, geometry) \tag{4.2a}$$

where P is the load applied to the specimen. A correction to the crack length to account for the plastic zone in calculating K_I was used. The correction, discussed in [60] is given by

$$a_e = a + \beta r_y \tag{4.2b}$$

where a is the crack length,

$$r_y = \frac{1}{2\pi}\,\frac{n-1}{n+1}\,\left(\frac{K_I}{\sigma_o}\right)^2 \tag{4.2c}$$

and

$$\beta = \frac{1}{[1-(P/P_0)^2]}. \tag{4.2d}$$

Equations for the limit load, P_0, are given in [60].

The specimen dimensions and geometries are given in Figure 4.8. Both three point bend and compact tension specimens were tested. The specimens were lapped optically flat and polished to a mirror finish. The pre-crack was cut with a wire electric discharge machine, producing a crack tip diameter of 0.3 mm. Annealed 4340 steel and cold-rolled 1018 steel were used. The heat treatment of the 4340 steel was: 843^oC for 1.5 hours, oil quench, then anneal at 649^oC for 1 hour and air cool. The material properties were: yield stress $\sigma_o = 830\ MPa$, hardening exponent n=8.7, and $\alpha = 3.3$ for a best fit of the uniaxial tension properties to the Ramberg-Osgood material model. The uniaxial tension stress-strain curve is shown in Figure 3.9. Also shown in the figure are stress-strain curves for other heat treatment of 4340 steel. The 1018 steel was used as received. Its uniaxial tension curve is shown in Figure 4.9. The 1018 steel had $\sigma_o = 560\ MPa$ with no hardening.

The tests proceeded by loading the specimen to some level and then maintaining that level while caustics were photographed for different values of z_o. The load was then increased a step and the process repeated.

4.3. Experimental Results and Discussion.

4.3.1. *Sequence of Caustics.* A sequence of photographs of caustics is shown in Figure 4.10. These photographs are from specimen 28, (compact tension) loaded such that $r_p \approx 3.4mm$. Only the distance z_0 was varied, thus varying the initial curve size r_0. The parameter r_0/r_p in the figure is the ratio of the initial curve size to plastic zone size. The plastic zone size r_p was estimated by measuring the extent of the visual evidence of plastic deformation seen in the photographs. The initial curve size r_0 was estimated using equation (2.11) when $r_0/r_p<1$ and equation (2.7) when $r_0/r_p>1$. It is seen from Figure 4.10 that for $r_0/r_p \leq 0.35$ the caustics agree in shape with the caustic predicted from the plane stress HRR field (Figure 2.7a). For r_0/r_p=1.4 (Figure 4.10f) the caustic has the shape predicted using the singular elastic field.

Comparing the experimentally observed caustics with the numerically generated ones of Figure 4.6 it is seen that in both cases there is a transition from an "HRR caustic" to an "elastic caustic" as r_0/r_p goes from 0.19 to 1.4. The transition away from the HRR caustic occurs at $r_0/r_p \approx 0.35$ for the experimental results and at $r_0/r_p \approx 0.30$ for the numerical results. Thus it appears that the transition from the HRR caustic to the elastic caustic occurs sooner in the numerical model than in the experiments. However, the general trend is similar in each case.

By comparing the shapes of the experimentally observed caustics to the predicted caustic shape (Figure 2.7a) further information on the region of dominance of the HRR field can be obtained. If the caustic is not shaped similar to the predicted caustic then the displacement fields near the initial curve cannot correspond to that of the HRR field. The caustics of Figure 4.10 deviate from the predicted shape for $r_0/r_p \geq 0.35$ indicating that under small scale yielding an upper bound for the dominance of the HRR field is $r \approx 0.35 r_p$.

4.3.2. *Effect of Plasticity on Elastic Caustics.* Under conditions of plane stress, small scale yielding the elastic singular field dominates at some distance outside the plastic zone. Thus when the initial curve radius r_0 satisfies $r_0 \gg r_p$ and $r_0 \ll a$ where a is the crack length or some other relevant in plane specimen dimension, K_I may be measured with caustics by applying equation (2.6).

The numerical results shown in Figure 4.5 show that the elastic singular field does not agree with the actual stress field when $r < 1.5 r_p$. Thus values of K_I measured with caustics are expected to be affected by the plastic zone when $r_0 < 1.5 r_p$.

To quantify the effect of plasticity on caustics from outside the plastic zone, experiments were performed measuring K_I from caustics, K_{caus}, at different distances from the crack tip and comparing K_{caus} to K_I measured from the boundary conditions, K_{BC}.

The results are presented in Figure 4.11 where K_{caus}/K_{BC} is plotted vs. r_0/r_p. The initial curve radius r_0 is calculated using equation (2.7). For all of the tests r_p was calculated using the numerical results

$$r_p = 0.25\left(\frac{K_I}{\sigma_0}\right)^2 \tag{4.3a}$$

for the 4340 steel (n=8.7) and using the estimation

$$r_p = \frac{1}{\pi}\left(\frac{K_I}{\sigma_0}\right)^2 \tag{4.3b}$$

for the 1018 steel ($n\rightarrow\infty$).

According to [20], for elastic solids plane stress conditions prevail for $r>0.5h$, where h is the specimen thickness. Therefore only caustics satisfying $r_0>0.5h$ were plotted, ensuring plane stress conditions. The parameter r_p/b in the figure is the ratio of plastic zone size to uncracked ligament size, b. This parameter indicates the extent of yielding that has occured. No data were obtained for $r_p/b>.046$ because beyond that level of yielding it was not possible to observe a caustic that was shaped like the predicted caustic since small scale yielding conditions were no longer satisfied. Some data points are given for $0.7<r_0/r_p<1.0$. It was observed that for r_0/r_p as small as 0.7 the caustic curve remained close to the elastic shape. Thus it is appropriate to present data for $r_0/r_p\approx0.7$ along with data for $r_0>r_p$.

The results of Figure 4.11 show that away from the plastic zone equation (2.6) is valid. However, for $r_0\leq1.5r_p$, K_{caus}/K_{BC} deviates from 1.0 indicating that serious errors will occur if equation (2.6) is applied for the evaluation of caustics in this range. This limit does not appear to depend on hardening for $n\geq9$ since the 4340 steel and the 1018 steel data are consistent with each other.

As stated above the caustics retain the shape predicted by the elastic analysis even for r_0/r_p as small as 1.0. Thus the effect of the plastic zone on the caustic cannot be judged by observation of the caustic shape. The invariance of the shape of the caustic is explained by the numerical results. It was found that the sum $\sigma_{11}+\sigma_{22}$ generally follows the singular elastic field even for r_0/r_p as small as 1.2. This result is important because it is the out of plane displacement $u_3 = -\frac{h\nu}{2E}\left(\sigma_{11}+\sigma_{22}\right)$ that is relevant to caustics, and because the shape of the caustics is mainly determined by the angular distribution of u_3. Since the angular distribution of u_3 is in good agreement with the singular elastic field, the caustic shapes do not deviate much from the predicted shape as $r_0 \rightarrow r_p$.

4.3.3. *Three Dimensional Effects.* It has been demonstrated above that the plane stress, HRR field dominates for $r \leq 0.30 r_p$. Thus the application of equation (2.9) for analyzing caustics is restricted to $r_0/r_p < 0.30$ if plane stress conditions are satisfied. However, due to the finite thickness of an actual test specimen there is a region near the crack tip in which the deformation field is three dimensional. It was shown in [20] that for elastic materials this region extends for distances from the crack less than one half of the specimen thickness. Here the three dimensional effects in elastic-plastic materials are investigated.

Experiments were performed measuring J_{caus} using caustics at different distances from the crack tip and then comparing J_{caus} to J_{BC}, measured from the boundary conditions. The specimens used for these tests are the same specimens that were used for investigating the caustics from outside the plastic zone. The only difference is that here the initial curve was placed well inside the plastic zone, and the plastic zone size was generally larger.

The collective results are presented in Figure 4.12 where J_{caus}/J_{BC} is plotted vs. r_0/h. The initial curve size, r_0, was calculated using equation (2.11). Only data points corresponding to caustics for which the aspect ratio D_y/D_x was in good agreement with the value predicted by the HRR field were plotted. Here D_y and D_x

are the sizes of the caustic in the x_2 and x_1 directions. This was done to insure that only the three dimensional effects were being investigated. Other effects, such as the variation of caustic shape as r_0/r_p increases, are thus minimized. The maximum ratio of initial curve to plastic zone size was $r_0/r_p \leq 0.45$.

No results are given in Figure 4.12 for $r_0/h > 0.6$. The reason for this is that in a given test (h, r_p constant), as r_0/h is increased, r_0/r_p is also increased. When r_0/r_p becomes large the caustic shape is no longer similar to the HRR shape and thus a calculation of J using the analysis of caustics based on the HRR field is meaningless in such cases. It was found that r_p could not be increased indefinitely for two reasons. First, the thin specimens used here are prone to out of plane bending and buckling at the high loads needed to make r_p large. Second, extensive plastic deformation reduces the reflectivity of the specimens reducing the definition of the resulting caustic.

The results show that for $r_0/h \leq 0.6$, J_{caus}/J_{BC} is less than one, indicating that three dimensional effects are important in that region. The extent of the region of three dimensionality seems to be larger than the extent for elastic materials. The plane stress crack tip solution, equation (2.9) predicts that $u_3 \rightarrow \infty$ as $r \rightarrow 0$. However, since this is impossible, the actual u_3 is less than predicted. Thus so are the values of J_{caus}/J_{BC} since the size of the caustic increases with increasing u_3 and $\partial u_3/\partial x_\alpha$.

The results do not seem to depend on specimen configuration or on the particular steel. The reason for this consistency is that the tests were all carried out under nominally small scale yielding conditions, thus the only in plane distance that is important is the plastic zone size. Also note that the 4340 steel has a relatively low hardening making it nearly elastic-perfectly plastic like the 1018 steel.

4.4. Conclusions.

Application of the method of caustics for the measurement of the J integral in plastically deforming materials was investigated. It was found that under small scale yielding conditions the plane stress, HRR field dominates for $r<0.3r_p$. Thus the application of caustics as based on the HRR field is restricted to initial curves satisfying $r_0<0.3r_p$. For caustics obtained from the elastic region the presence of a plastic zone introduces errors in the measurement of the elastic stress intensity factor when $r_0<1.5r_p$. In an actual test specimen there is a region near the crack tip where the deformation field is not one of plane stress but is three dimensional. It was found that the extent of this region for plastically deforming materials extends to at least $r<0.6h$, where h is the specimen thickness.

In summary, to use caustics to measure fracture toughness the following restrictions must be observed. (1) For initial curves outside the plastic zone: $r_0/r_p > 1.5$, $r_0/h > 0.5$, $r_0/a << 1$. This implies $r_p/a << 1$ (small plastic zones). (2) For initial curves within the plastic zone: $r_0/r_p < 0.3$, $r_0/h > 0.6$, $r_0/b < .06$, where b is the uncracked ligament and a is the crack length.

For less ductile materials the conditions (1) can be satisfied at fracture initiation. For more ductile materials (1) cannot be satisfied and one must try to put the initial curve within the plastic zone. However, the conditions (2) are so restrictive and conflicting that they can rarely be met. Thus to make caustics useful for studying the toughness of ductile materials a different approach must be taken. This approach is discussed in the next chapter.

Chapter 5

MEASUREMENT OF THE J INTEGRAL WITH CAUSTICS: LARGE SCALE YIELDING

As discussed in Chapter 4 the interpretation of caustics based on two dimensional, analytical solutions that do not take into account the finite specimen geometry results in a procedure that is too restrictive for practical applications to elastic-plastic fracture mechanics. In this chapter an approach is taken that will allow the initation value of the J integral (assumed here to be a fracture criterion) to be measured under both static and dynamic loading conditions (Chapter 6).

Since methods for determining J are well established for static loading there is no point on applying caustics to static problems. However, under dynamic loading this application of caustics can replace expensive finite element calculations that would be necessary to interpret a dynamic test and to determine the time history of J. Furthermore, as discussed in Chapter 3 standard instrumented impact tests do not generally provide enough information to determine the fracture initation time, a quantity that is needed for calculations of the critical initation value of J, or J_C.

In brief, the approach taken here is to make a static calibration of J versus the caustic diameter for a particular material and specimen geometry. Such an approach is similar in principle to that taken by Loss [61], where strain gages were applied to the specimen, near the crack tip. In Loss's technique a low load calibration of strain vs. K_I was made and then extrapolated linearly for measuring K_{IC} in a drop weight test. As one might think, this approach will be good only for the particular specimen tested; a new calibration is required for each new specimen geometry or material.

In addition to caustics strain gages were also used in the current experiments. Strains measured near the crack tip were related to the J integral through a static, nonlinear calibration. This relation will serve as a secondary measurement of J

during the drop weight experiments.

Although the principal goal of Chapters 4 and 5 is to examine the application of caustics to ductile materials two issues keep appearing. These are the extent to which the near crack tip fields are three dimensional and the extent of dominance of the asymptotic solutions. These issues are being examined in further detail in a companion study by Narasimhan and Rosakis [62]. In this study, the specimen upon which the experiments in this chapter were performed is being analyzed in a three dimensional, elastic-plastic, finite element calculation. In order to provide a direct comparison between the calculations and the actual specimen a second experiment was performed simultaneously with the caustics experiment. Using Twyman-Green interferometry, the out of plane displacement was measured for load levels up to fracture initiation. These displacements are compared directly to the numerical results. In addition the load, load point displacement and strains measured near the crack tip are compared to the numerical results. This cross checking of results from two techniques is very helpful in establishing confidence in and accuracy of both the numerical calculations and the experiments.

5.1. Description of Experiments.

These experiments used three point bend specimens (numbers 67 and 69) with a 4:1 length to width ratio. The specimen dimensions are given in Figure 5.1. As before 4340 steel was used but with a higher yield stress heat treatment. The heat treatment was: 843°C for 1.5 hours, oil quench, then anneal for 1 hour at 538°C. The material properties were yield stress σ_0 = 1030 MPa, and hardening exponent n = 22.5 for a fit to the piecewise power hardening law, equation (4.1). An alternative description of the stress strain behavior is obtained by a fit to the Ramberg-Osgood model, equation (2.8). In this case α=2 and n=15.7. The uniaxial stress-strain curve is given in Figure 3.9. As with the previous experiments the specimens were lapped optically flat and polished to a mirror finish. For these experiments both sides of the specimen were polished to allow for simultaneous caustics and interferometry measurements.

Four measurements were performed on each specimen: Caustics, interferometry, load, load point displacement, and strain gages. The strain gage locations are shown in Figure 5.1. A photograph of the specimen, the loading fixtures, strain gages and extensometer (for measuring load point displacement) is shown in Figure 5.2.

The experiments proceeded by loading the specimen in small steps. During the loading the strain gages, load cell and extensometer signals were recorded. When loading was stopped at a particular step caustics photographs and interferometric photographs (interferograms) were recorded. This process was repeated until the point of fracture initiation. A summary of the experiments giving the values of J and the plastic zone sizes is given in Table 5.1.

5.1.1. *Load and Load Point Displacement.* The load and load point displacement were recorded with a 100 000 lb. capacity load cell and a strain gage extensometer. The signals were recorded during loading by a digital oscilloscope. There exists some extraneous displacement due to compliance of the loading fixtures, and denting of the specimen at the contacts with the rollers. This extraneous displacement was subtracted using the procedure of Robinson [63]. In this procedure the support rollers are placed together, and an uncracked specimen is inserted between the support rollers and the loading roller. The entire system is then compressed and the load-load point displacement was measured. It was found that the extraneous displacement was approximately linear with load.

5.1.2. *Strain Gages.* The strain gages measured the ϵ_{22} strain component along a line roughly perpendicular to the crack line. The choice of gage location was designed to place the gage in a region where the strains would be high but not out of the elastic range. The gages were connected to a single arm bridge and recorded unamplified on the digital oscilloscope.

5.1.3. *Caustics.* The caustics were photographed with a setup exactly the same as discussed previously (see Figure 4.7). In drop weight testing only one value of z_0 can be used during a test thus in these tests z_0 was held constant. A preliminary experiment was performed to choose a suitable z_0. In this experiment caustics were obtained for various z_0 values and load levels. At low loads the caustics were all very clear for all z_0's. But as the load increased the caustics for small z_0's become blurred and ill defined. This is caused partially by a loss of reflectivity due to plastic deformation. On this basis it was decided to use z_0 = 100 cm. This choice allows caustics to be recorded without loss of definition up to the fracture initiation load.

5.1.4. *Interferometry.* A version of the Twyman-Green interferometer [64] was used to measure the out of plane displacement, u_3. A sketch of the optical arrangement is shown in Figure 5.3. Due to the high sensitivity of interferometry minimization of vibration of the specimen and optics is important. Thus the entire apparatus including the loading frame is mounted on an isolated optical table. A photograph of the specimen and interferometer optics is shown in Figure 5.4. The loading frame pivots in a yoke that is rigidly mounted to the optical table, allowing for a tilting adjustment of the specimen.

For interferometry a 50 mm diameter collimated laser beam is split into two with a beamsplitter. The reference beam reflects from the flat mirror back through the beamsplitter and into the camera, see Figure 5.3. The object beam reflects from the specimen, through the beamsplitter and into the camera. When the two beams are adjusted to fall on top of each other any nonuniform differences in optical path length between the two beams results in light and dark fringes. The laser used produces coherent, monochromatic light with a wavelength of 632.8×10^{-3} mm. The fringe patterns were photographed with a 35 mm camera using a 200 mm f4 (50 mm diameter) telephoto lens. The camera was located such that 50 mm of the specimen just filled up the 35 mm film frame. Kodak Technical Pan 2415 film shot at ASA 100 and developed in Kodak D-19 was used in order to achieve high contrast and high

resolution.

For complete interference between the reference and object beams the intensity of light from each beam must be matched. Polished steel has a reflectivity of 50%, thus to match the reference beam to the object beam a 50% reflectance mirror was used.

Destructive interference between two waves occurs when the waves are out of phase by $\lambda/2, 3\lambda/2, \cdots$ where λ is the wavelength. The phase shift between the reference and object beams is equal to the difference in optical path length, thus the change in optical path length δS represented by adjacent dark fringes is $\delta S = \lambda$. For small deformations $S = 2u_3$, thus adjacent dark fringes represent a change in u_3 of $\delta u_3 = \lambda/2$.

It is important to focus the camera on the surface of the specimen so that a large caustic will not be formed, obscuring the crack tip. By minimizing the caustic, fringes can be resolved to within approximately one crack tip diameter.

Due to the angular deflection of the reflected light rays, as seen in Figure 2.4, the relation $S = 2u_3$ is not completely accurate; the actual optical path is slightly larger. In addition the angular deflection will change the location of the fringes. It is demonstrated in Appendix B that for these experiments the maximum error in fringe location is less than 1λ and in the u_3 values the error is less that $.01\lambda$.

The interferograms were analyzed by making 50X enlargements and digitizing the fringes by hand on a computer digitizing pad. The center of each dark fringe was estimated by eye and its position was digitized.

5.2. Numerical Calculations.

The numerical calculations modelled in three dimensions one quarter of the three point specimen shown in Figure 5.1, using six layers of elements for half the thickness. An incremental J_2 plasticity theory was used. The material obeyed the von Mises yield criterion and followed the piecewise power hardening law of

equation (4.1), with n=22.5. Loads were applied to the specimen incrementally in 140 steps, going from 0 to 80000 N. The J integral was calculated using a numerical domain integral representation as given in [65]. This value of J coincides with the value of J calculated as an integral over a cylindrical surface surrounding the crack front divided by the specimen thickness.

5.3. Results: Comparison between Experiments and Calculations.

5.3.1. *Load, Displacement, and J Integral.* The specimen geometry was chosen to take advantage of the load-displacement methods for estimating the J integral. For the 3-point bend specimen J may be estimated by [66,67]

$$J = \frac{2}{hb}\int_0^{\delta} P\, d\delta \quad , \tag{5.1}$$

where P is the load applied to the specimen, δ is the load point displacement, h is the specimen thickness and b is the uncracked ligament length. The accuracy of the equation has been confirmed experimentally by several authors [68,69] and the consensus is that equation (5.1) is accurate for $s/w > 4.0$ and $0.4 < a/w < 0.7$. In the present experiments $s/w = 4.0$ and $a/w = 0.4$. However, as will be discussed it was found that the above is not accurate for our specimen.

The load-displacement (P-δ) curves for specimens 67 and 69 are shown in Figure 5.5. For each specimen the curve is shown only up to the point of fracture initiation. Also shown is the P-δ curve calculated from the numerical model. Good agreement is obtained between the experiments and the calculations. It is seen that the P-δ curves flatten out at around 75000 N but the numerical curve increases to nearly 80000 N for the same δ. The difference is due to crack initiation occurring in this range.

The resulting J integral given as a function of load, P, is shown in Figure 5.6. Shown in the figure are J calculated from equation (5.1) using the experimental

results and the numerical results. Also shown are J calculated as a domain integral from the numerical results and J calculated using the EPRI approach [60], introduced by Shih and Hutchinson. In the EPRI approach J is calculated by using the elastic-plastic estimation formula:

$$J = J^e(a_e) + J^p(a,n) \quad , \tag{5.2a}$$

where

$$J^e(a_e) = \frac{K_I^2(a_e)}{E} \quad , \tag{5.2b}$$

and

$$J^p(a,n) = \alpha \frac{\sigma^2}{E} b h_1(a/w,n) \left(\frac{P}{P_0} \right)^{n+1} \quad . \tag{5.2c}$$

The values of h_1(a/w, n) were calculated by using the finite element method and are given in tabular form in [60]. K_I is calculated as if the specimen were elastic as in equation (4.2a). An expression for a_e is given in equation (4.2b). The parameters α and n corresponding to a fit of the stress-strain data to the Ramberg-Osgood model were used for this calculation. For plane stress $h_1(0.4,16) \approx 0.16$, and the limit load P_0 is .

$$P_0 = 0.536 \frac{\sigma_0 b^2}{s/2} = 75900N \quad .$$

The numerical domain integral result is considered here to be the most accurate evaluation of J since this method of calculation is a direct consequence of the surface integral integral definition of J. This will be called the "true J value". It is seen that the experimental and numerical values of J calculated from the P-δ method,

equation (5.1), are the same but both are too large by approximately 20%. Although equation (5.1) is an approximation, in light of previous results [68,69] better agreement was expected between the approximate and the true J. Note that $\int_0^{\delta} P\, d\delta$ represents the energy input to the specimen. An alternate expression of the energy is $\int_0^{\theta} M\, d\theta$ where M is the moment across the uncracked ligament and θ is the work conjugate rotation. Thus J may be estimated by substituting $\int_0^{\theta} Md\theta$ for $\int_0^{\delta} Pd\delta$ in equation (5.1) [66,67]. It was found in the numerical calculations that by taking θ as the crack mouth opening displacement divided by the distance from the crack mouth to a fixed "hinge point", J could be accurately evaluated for the higher loads. Thus in future experiments it is recommended that the $Md\theta$ version of equation (5.1) be used. The EPRI approach agrees with the true J up to 60000 N, that is it agrees under small scale yielding where J^e dominates equation (5.2). The EPRI approach is not expected to be very accurate for low hardening since for large n h_1 is a very sensitive function of a/w, thus making interpolation of h_1 values somewhat inaccurate. Also for large n, the term $\left(\frac{P}{P_0}\right)^{n+1}$ is very small until $P>P_0$.

5.3.2. *Strains.* The strain gages placed on the specimen measure ϵ_{22} on the specimen surface averaged over the area of the gage. The strains for the two gages are plotted versus the applied load in Figure 5.7. Also shown are the strains calculated numerically at the same locations. The agreement between the experimental and numerical results is best for strain gage #1, the gage nearest the crack tip, where the finite element mesh is finest. At the location of strain gage #2 strains from several elements were averaged to obtain the numerical results shown.

Note that the measured strain for gage #1 begins to decrease even before fracture intiation, but the numerical strain does not. This unloading and difference with the numerical results indicates that tunneling, or crack extension in the interior of the plate, is occurring prior to visible crack intiation on the surface of the plate.

Thus it seems that crack initiation occurs over a range of loads, starting at 67600 N and finishing at 74700 N, corresponding to J values from 270 kN/m to 420 kN/m. A more detailed version of this experiment could use compliance techniques to determine a J resisitance curve rather than only an initiation value as is done here.

In Figure 5.8 the strains for gage #1 and the corresponding values of J are plotted. The solid line is a fit to the experimental data. The values of J that were used are the values calcuated from the numerical results with the domain integral. The fit to the experimental data was used to determine J from strains measured in drop weight experiments. Clearly there are a few problems with the measurement of J from this technique. It is seen that $J(\epsilon)$ is not a unique function due to the decrease in strain caused by crack tunneling. Thus a choice must be made concerning which part of the $J(\epsilon)$ curve is relevant. Near the peak strain $J(\epsilon)$ is very sensitive thus a small change in ϵ, caused perhaps by electrical noise, produces a large change in J.

5.4. Results: Caustics.

Caustics were recorded for specimens 67 and 69 using the fixed value z_0 = 100 cm. The sequence of caustics for increasing loads for specimen 69 is shown in Figure 5.9. Although the caustics are nearly circular the equation for elastic caustics, equation (2.6) cannot be used to evaluate them. The experimental results are presented in Figure 5.10 as non-dimensionalized caustic diameter versus non-dimensionalized J integral. Examination of equations (2.6) and (2.10) shows that the relation between J and D may be non-dimensionalized as in the figure. Also shown in Figure 5.10 are the relations for the elastic case, equation (2.6), and for the HRR field case, equation (2.10). The calibration of D versus J is valid only for the specimen tested here and only for z_0 = 100 cm. This curve is used as a master curve for interpreting drop weight experiments of the same material and specimen, and with the same z_0.

The main reason for normalizing the experimental data is to compare it to the analytical results and to be sure that the results are at least similar in form and in

magnitude. From Figure 5.9 it is seen that for the entire loading range the caustic is nearly circular, thus the issues discussed in sec. 4.3.2 are relevent here. At low loads D is small, thus the initial curve size, r_0, is small; it is within the region near the crack tip of three dimensional deformations where the caustic diameter is smaller than predicted analytically. As the specimen is loaded, r_0 increases and the plastic zone size r_p also increases. The initial curve is now outside of the region of three-dimensionality but $\frac{r_0}{r_p}<1.5$ thus causing D to be larger than that predicted by the elastic analysis.

5.5. Interferometry and u_3 Comparison.

Interferograms were recorded for load levels from 6000 N up to fracture initiation, 74700 N. At the highest load levels the quality of the interferograms deteriorates. This is due to the combination of roughening of the surface due to plastic deformation near the crack and the high fringe density near the crack tip due to steep deformation gradients there. The highest load for which fringes near the crack tip could be resolved was 57300 N.

The level of initial flatness of the specimens is demonstrated by Figure 5.11 where it is seen that over 5 cm the surface elevation of the unloaded specimen does not vary by more than 1λ. (Recall that each dark fringe represents a change in u_3 of $\lambda/2$ from the adjacent dark fringe.)

Typical interferograms are presented in Figures 5.12 and 5.13. Both photographs are for a load of 35000 N, but the photograph in Figure 5.13 is greatly enlarged (and the contrast is reversed.) Although the fringes at the crack tip are not resolvable in Figure 5.12 they are resolvable when magnified enough as in Figure 5.13. Here it is seen that fringes can be resolved almost all the way to the crack tip, except for that part obscured by a very small caustic.

The interferograms actually represent the u_3 displacement of the specimen with respect to some inclined plane, the plane of the reference mirror. During the

experiment the mirror is aligned to be as close to perpendicular to the specimen as possible. However it will usually be off a little thus some additional information is needed to analyze the interferograms. What is needed is to know a priori the displacements at three noncolinear points on the specimen, then any inclination of the mirror can be corrected for. The u_3 results from the interferograms are matched up with the known displacements at those points to get the true displacement field. In these tests the displacements at known points were provided by the finite element calculation. It was found that u_3 was zero (or very nearly zero) at x_1 = -1.5 cm, x_2 = 0 and zero at x_1 = 2.1 cm, x_2 = 0 and u_3= -5.72x10^{-3} mm at r=1.0 cm on the line θ= 40^{0}C. Actually the location of the zero displacement point ahead of the crack tip changes slightly as the specimen is loaded, and although this was accounted for, using a fixed zero point would have caused little error. Even a simple two dimensional, elastic model could have been used almost as well. Using a coarse mesh with a two dimensional, elastic finite element model the zero point was calculated to be at 2.0 cm. Thus even simple finite element calculations are very valuable in interpreting interferograms.

The u_3 displacement along the line θ=0 is shown in Figure 5.14 for three load levels. Data are shown only as close to the crack tip as fringes could be resolved. Generally fringes could be measured to approximately 0.3 mm ahead of the crack tip and to approximately 0.5 mm behind the crack tip. Away from the crack tip u_3 is linear with x_1 as it should be for a beam. The displacement crosses zero at $x_1 \approx$ 2.1 cm and is positive for greater x_1 values since this part of the specimen is in compression. The displacement gradients are much larger behind the crack tip than ahead of the crack tip. The plastic zone does not spread much behind the crack tip, and since most of the displacement occurs within the plastic zone, this displacement must occur over a small distance, causing the steep displacement gradients.

In Figures 5.15-5.17 u_3 is presented on θ=0 for three loads, nondimensionalized by J/σ_0. Also shown in these figures are the numerical results for the same load levels. For reference the extent of the plastic zone on θ=0 and x_1 corresponding to

one half the specimen thickness are also shown in the Figures. In Figure 5.15, where the plastic zone is very small, u_3 from the linear elastic K field, equation (2.5), is given. In Figure 5.17, where the plastic zone is larger, u_3 from the HRR field, equation (2.9) is given.

The first observation is the excellent agreement between the experimental and numerical results at all load levels. The agreement of the calculated u_3 displacements as well as the agreement of the other measured quantities with the experiment leaves no question that the numerical calculations are accurate and sufficiently detailed to model well this specimen. To show that the angular variation in displacement of the numerical results is also accurate, the numerical and experimental u_3 along the line θ=40^o is given in Figure 5.18 for a load of 52300 N. Again the agreement of numerical and experimental results is excellent.

For all load levels it was found that there is no region where the plane stress HRR field adequately described u_3 on the specimen surface. This is consistent with results of Chapter 4 where it was found that caustics based on the HRR fields could not be used to accurately measure J. The asymptotic HRR field does not agree with the actual field because of three dimensionality of the near crack tip fields and due to the finite specimen dimensions that cause higher order terms to become important away from the crack tip. At low loads Figure 5.15 shows that the K_I field does not predict u_3 well even for r/h > 0.5, due again to the finite specimen dimensions and the importance of higher order terms. However the method of caustics as based on the K_I field could probably be used for these specimens at low loads since from the figure it appears that the experimentally obtained slope is about the same as that predicted by the K_I field. Recall that caustics depend on $\frac{\partial u_3}{\partial x_i}$ not on the absolute value of u_3.

To help visualize what the u_3 field looks like near the crack tip, the experimentally obtained u_3 is plotted three dimensionally in Figures 5.19a and 5.19b for two different views.

Recent experiments [70] on very thin, ductile specimens showed that the HRR field does predict u_3 and u_2 for r/h > 1. In those experiments the ratio of specimen width to thickness was 30:1. In the present experiments the ratio is 7:1. The results indicate that if one can make measurements in a region far enough away from the crack tip so that three dimensional effects are negligible, but close to the crack compared to in plane specimen dimensions, then the asymptotic fields will accurately describe the true fields in some region. How close to the crack compared to in plane specimen dimensions will depend on specimen geometry, and if the material is non-linear on the applied load level. One puzzling result of [70] is that $-u_3$ is maximum not at the crack tip but at r/h$\approx$0.5. This result is contradicted by both the present results and those in [71] that show that $-u_3$ is maximum at the crack tip. Perhaps the difference has to do with the differences in specimen geometries between the different experiments.

Table 5.1 Summary of Results, Specimens 67 and 69

Load, kN	J, kN/m	r_p, mm	r_p/h	r_p/b
21	19.8	1.2	.12	.03
35	54.7	3.3	.33	.07
52	130.	7.8	.78	.17
75	420.	25	2.5	.54

Chapter 6

DYNAMIC MEASUREMENT OF THE J INTEGRAL

Many issues relating to the fracture mechanics of ductile materials were discussed in Chapters 4 and 5. Although all of the experiments and calculations were performed statically they were done keeping in mind the goal of measuring J under dynamic loading. In this chapter experiments are described where the J integral was measured dynamically in a ductile steel using the method of caustics. This is the first time that such a measurement has been successfully performed. In addition, J is measured using strain gages as described in Chapter 5. Some limitations to the use of caustics for this measurement will be explored by looking at the results of some "unsuccessful" experiments.

Certain questions can be raised concerning the meaning of the J integral under dynamic loading, its applicability as a fracture initiation criterion, and our ability to measure it. Let us first discuss these issues, and then the experiments and results will be discussed.

6.1. Theoretical Concerns.

For elastic materials or for materials modeled by the deformation theory of plasticity, the line integral J is path independent for static loading. For two dimensional problems J is defined as [5]

$$J = \int_{\Gamma} (W n_1 - \sigma_{\alpha\beta} n_\beta u_{\alpha,1}) d\Gamma \quad , \tag{6.1}$$

where the strain energy density W is given by

$$W = \int_0^{\underline{\epsilon}} \sigma_{\alpha\beta}(\underline{\epsilon}) d\epsilon_{\alpha\beta} \quad , \tag{6.2}$$

Γ is a path enclosing the crack tip, and $\underline{n}$ is the outward unit normal to Γ. For elastic materials J equals the energy release rate, G. Although J is not equal to G for plastically deforming materials, J is the amplitude factor of the crack tip stress and strain fields, and under monotonic loading, where the deformation is nearly proportional, J is very nearly path independent. Thus J may be used as a fracture toughness parameter.

Under static loading there is a one to one relation between J and the crack tip displacement field. By making a calibration of caustic diameter or strain versus J, use is made of this one to one relation.

The J integral is not path independent for a stationary crack subject to dynamic loading. However, for a *linear or nonlinear elastic material* if J is defined only in the limit as $\Gamma \rightarrow 0$, then calling this J_d to distinguish it from the definition of equation (6.1),

$$G = J_d = \lim_{\Gamma \rightarrow 0} \int_{\Gamma} (W n_1 - \sigma_{\alpha\beta} n_\beta u_{\alpha,1}) d\Gamma \quad . \tag{6.3}$$

Alternately J_d for this situation may be calculated by path-area type integrals [72,73] or by domain integral type expressions [65].

As in the static case, for *plastically deforming materials,* $J_d \neq G$. Thus we should ask what is the usefullness of J in dynamic loading situations? *If* it can be argued that J_d still has the meaning of the amplitude of the crack tip stress and strain fields, then J_d has meaning for dynamic loading and may be useful as a fracture initiation criterion.

The questions to be resolved are (i) does J_d characterize the crack tip stress and strain fields? (ii) Is the relation between J and u_{static} the same as the relation between J_d and $u_{dynamic}$? (iii) What does one really measure with caustics under dynamic loading?

Some analytical estimates are available that indicate that the crack tip fields are the same statically and dynamically. The plane strain deformation of a rigid plastic half space subjected to dynamic indentation by a flat rigid punch was solved by Spencer [74]. It was found that near the punch the slip line field was the same statically and dynamically. Away from the punch the slip line field deviates from the static solution by an amount that depends on the loading rate and on the distance away from the punch. The punch indentation problem produces the same slip line field as the tensile crack problem, thus these results are evidence that the near crack tip fields are the same statically and dynamically.

An estimate of the deviation of the fields from the static solution can be obtained for a dynamically loaded antiplane shear crack in an elastic-perfectly plastic material, see Appendix C [75]. From this analysis it is seen that the dynamic effects vanish at the crack tip and that for loading rates in the range of drop weight testing the dynamic effects are negligible for distances from the crack tip of less than 5-10 cm.

A consequence of the results that show that the near crack tip fields are the same statically and dynamically is that there must be a region near the crack tip where J as defined by equation (6.1) is path independent even for dynamic loading. Thus it can be argued that the near crack tip fields are characterized by J and furthermore that J as defined by equations (6.1) and (6.3) are the same within the crack tip region.

Although there certainly is no proof, there are some results that support the assumption that J_d characterizes $u_{dynamic}$ in the same manner as J characterizes u_{static}. In dynamic, notched bar, tensile fracture experiments [76] J was measured dynamically by measuring the local crack opening displacement and the stress transmitted across the uncracked ligament. The value of J was then determined from a statically derived equation similar in form to equation (5.1). Subsequent numerical analysis [73] showed that this approach is accurate when the measured J

values are interpreted as J_d values. This result implies that in a region sufficiently close to the crack tip the deformation and stress fields are of the same nature statically and dynamically. Caustics are generated by the crack tip u_3 displacement fields. Thus although the correspondence between J and the tup load will not be the same statically and dynamically, if the correspondence between J and u_3 is the same statically and dynamically then so will be the caustic diameter versus J relationship since the caustics depend on u_3. Similarly, strains measured near the crack tip should have the same relation to J statically as dynamically.

Strain rate effects should also be considered. If it is assumed that the crack tip fields are those of the HRR fields, then [77]

$$\dot{\epsilon}_{ij} = \left(\frac{n}{n+1}\right)\cdot\left(\frac{\dot{J}}{J}\right)\epsilon_{ij} \quad . \tag{6.5}$$

In the experiments to be described the average $\dot{J}$ was $\dot{J}\approx 5x10^8$ N/(ms), or $\dot{J}/J\approx 1250/s$ at fracture initiation. Thus for a large strain level, let us say $\epsilon\approx 0.10$, $\dot{\epsilon}\approx 125/s$, or at the elastic-plastic boundary, where $\epsilon=\epsilon_0$, $\dot{\epsilon}\approx 6/s$. In the heat treatment used here 4340 steel is relatively rate insensitive. Data in the literature [78] indicate that the yield stress increases by less than 30% over its static value for a strain rate of 2000/s. Thus for the moderate strain rates of this experiment the effect of strain rate sensitivty will be small. In addition, recent calculations [77] modelling a stationary crack in a highly strain rate sensitive, ductile material under dynamic loading, showed that for the same values of J the strain distribution was nearly the same statically and dynamically. However this was not true for the stress distribution. Since what is measured in the current experiments are strains and displacements, the above result implies that strain rate effects on caustics will be negligible even in highly strain rate sensitive materials.

6.2. Description of Experiments.

The experiments were essentially the same as those described in Chapter 3. Three point bend specimens (numbers 70 and 71) of the same dimensions and heat treatment as those in Chapter 5 (see Figure 5.1) were tested in the drop weight tower. The drop weight was 1910 N and the impact speed was 5 m/s. Caustics were photographed with the high speed camera at a rate of 100 000 frames per second. The tup load, support load and the two strain gage signals were recorded on a high speed, digitial oscilloscope. In these experiments interest was confined to recording the J integral up to the time of fracture initiation.

6.3. Results and Discussion.

The tup load record for specimen 71 is given in Figure 6.1. The load record is highly dynamic and it is clear that determination of J from the static, load versus J results of Figure 5.6 is hopeless for short times. At later times (>400 μs) the load varies more slowly and it may be possible to approximate J from the tup load. The peak load achieved was approximately 80000 N, corresponding statically to J $\approx$ 600 kN/m. From caustics the fracture initiation time was 700 μs; it is seen that the tup load gives no indication of the time of fracture.

The strains recorded during the experiment are presented for specimen 71 in Figure 6.2. The strains at each location vary in phase and as in the static experiments the strain at gage #1 begins to decrease while the strain at gage #2 continues to increase, indicating that crack tunneling is occurring prior to fracture initiation. As with the tup load the strain gages give no indication of the time of fracture initiation.

Selected caustics photographs from specimen 71 are shown in Figure 6.3. These caustics correspond in size and shape to those recorded statically, Figure 5.9. The size and shape of the static and dynamic caustics agree except for the last recorded dynamic caustic, which is elongated, indicating crack tunneling.

Fracture in these thin, ductile specimens occurs in a shearing manner (there is no flat fracture region) thus when the crack initiates the caustic becomes asymmetric due to the shearing type of fracture. This asymmetry results in the caustic not closing back on itself behind the crack tip. When this first occurs fracture initiation has occurred. The time to fracture was 700 μs for specimen 70 and 780 μs for specimen 71.

Using the static caustics calibration of Figure 5.10, and the caustics photographed with the high speed camera, J(t) was determined for each specimen and is presented in Figure 6.4. Also shown in the Figure is the J(t) record determined from strain gage #1. Overall there is a very close correspondence between J(t) as determined from caustics and J(t) from the strain gage. There is however a substantial disagreement during the time from 300 μs to 400 μs. This corresponds to the portion of the J(ϵ) curve, Figure 5.8, where the strain decreases while J is increasing causing the J(ϵ) relation to be non-unique. At some time a jump is made from one branch of the curve to another, thus the large jump in J(t) at 300 μs.

The reason for performing a fracture initiation experiment under dynamic loading is that the toughness may increase or decrease compared to the static values. Thus accurate predictions of dynamic fracture initiation require dynamic fracture toughness experiments. Although the current experiments were not true fracture toughness measurements since they were performed not with a fatigued crack tip but with a crack of diameter 0.3 mm, it is useful to compare the fracture initiation values, J_c, from the static and dynamic experiments. Statically $J_c \approx$ 420 kN/m. Dynamically $J_c \approx$ 350 kN/m using the caustics results or $J_c \approx$400 kN/m using the strain gage results. The value of J_c as determined solely from the tup load is $J_c \approx$600 kN/m, somewhat higher than than the other values. Since caustics are the most local of all three measurements it is felt that the caustics are the most reliable of the three.

6.4. Limitations of Caustics.

Some early experiments performed on thinner and more ductile specimens pointed out some limitations to the applicability of caustics for measuring J. Three point bend specimens of 4340 steel with dimensions of 30.5 cm x 10.2 cm x 0.6 cm thick were tested in the drop weight tower. The tempering temperature for these specimens was 649^0C, (σ_0=830 MPa, the same as the experiments in Chapter 4) producing a very ductile steel.

Extensive plastic deformation occurred in these specimens prior to fracture initiation. The caustics photographed from one of these experiments are shown in Figure 6.5. At later times, where the plastic zone is large, the caustic is very distorted and poorly defined. It is impossible to interpret such caustics even if a calibration was available.

6.5. Conclusions.

For the first time the J integral has been measured dynamically for a ductile material using an optical technique. Although there exist other procedures for measuring J in drop weight testing [79,80] these techniques are most useful for experiments where the time to fracture is somewhat long. The specimen tested here has a fracture initiation time of 700 μs, which is just borderline on being long enough to apply the other techniques. The method of caustics is not restricted to long fracture initiation times, and thus it complements existing techniques by providing a measurement that can be used for very high loading rates.

The drawback of caustics is that it cannot be applied to ductile materials when the plasticity is not too great. A rule of thumb for when caustics can be used would be that the plasticity is "contained" before fracture initiation. That is the plastic zone does not spread to the specimen boundaries. Specimens that fracture in such a state (fully yielded state) will have significantly longer facture initiation times than those that fracture with less plasticity. Thus for fully yielded specimens techniques other than caustics will be the most useful.

Chapter 7

SUMMARY AND CONCLUSIONS

The mechanics of dynamic fracture initiation and propagation in structural materials were investigated experimentally. In the first part of this thesis dynamic fracture propagation criteria are investigated by using an established application of the optical method of caustics. In the second part new experimental techniques to measure fracture initiation criteria for dynamically loaded cracks in ductile materials are investigated.

Throughout this research the optical method of caustics was used as the principal experimental tool. The method of caustics provides a nonintrusive, instantaneous measurement of the crack tip strain intensities. Application of caustics frees the experimenter from having to measure the complicated, time dependent boundary conditions (loads or displacements) applied to the test specimen, and from then inferring crack tip parameters from these measurements. Both static and dynamic experiments were performed. The static experiments were done to gain experience and to calibrate the method of caustics for application to dynamic, elastic-plastic fracture mechanics. The dynamic experiments used Caltech's rotating mirror high speed camera to record caustics at rates of up to 200,000 frames per second.

In the first set of experiments dynamic fracture propagation in a high strength 4340 steel was investigated. This steel serves here as a model material for dynamic crack growth under conditions of small scale yielding. The drop weight impact test, previously used only for fracture initiation studies, was adapted to study dynamic crack growth and initiation. This experiment produces reliable results and has many advantages over other commonly used test configurations. The results of these experiments support the existence of a monotonically increasing dynamic

fracture toughness crack propagation speed relationship, in qualitative agreement with analytical results. Unstable crack growth starting from a fatigue crack was investigated. The crack initially propagates slowly (< 100 m/s) and then accelerates to high speeds, approximately 700 m/s. This is in contrast to cracks initiated from supercritically loaded blunted notches that propagate very fast (> 1000 m/s) from the start. To complete this study the emission of stress waves during dynamic crack growth and the micromechanisms of fracture were investigated.

Application of the method of caustics for the measurement of the J integral in plastically deforming materials was subsequently investigated. The J integral characterizes the amplitude of the asymptotic crack tip stress and strain fields and thus it serves as a fracture initiation criterion for ductile materials where concepts of linear elastic fracture mechanics are not applicable. The results of these static experiments are compared directly to results from a finite element calculation modelling a crack under plane stress, small scale yielding conditions in an elastic-plastic material. It was found that under small scale yielding conditions the asymptotic fields, the HRR fields [6,7], dominate for distances from the crack tip of less than one third of the crack tip plastic zone size ($r < 0.3r_p$). Thus the application of caustics when based on the assumption of the validity of the two-dimensional, plane stress HRR fields is restricted to points of observation (initial curve) within one third of the plastic zone ($r_0 < 0.3r_p$). For caustics obtained from the elastic region the presence of a plastic zone introduces errors in the measurement of the elastic stress intensity factor when $r_0 < 1.5r_p$. There is a region near the crack tip where the deformation field is not one of plane stress but is three dimensional. It was found that the extent of this region for plastically deforming materials extends to at least $r < 0.6h$, where h is the specimen thickness. Thus to use caustics as based on the asymptotic fields to measure fracture toughness certain restrictions must be observed. These conditions are so restrictive and conflicting that they can rarely be met. Thus to make caustics useful for studying the toughness of ductile materials a different approach was taken.

In this approach problems of the region of dominance of the HRR fields, the extent of the crack tip region of three dimensionality and the effects of specimen geometry are all automatically accounted for. A static calibration of caustic diameter versus the J integral was made for a three point bend specimen. The relation was then used to measure the time history of J, J(t), dynamically in a drop weight experiment. This is the first time that an optical measurement of J has been made for dynamic loadings. A method based on strain gages for measuring J was also explored. The dynamic J record from strain gages agreed with the J record from caustics throughout most of the experiment. However there is a significant disagreement for one portion of the experiment indicating that the strain gage technique has some problems. This application of caustics will allow the fracture toughness of ductile materials to be measured under arbitrarily high loading rates.

At the same time (and on the same test specimens) that the caustic diameter versus J integral calibration was being measured, other measurements were performed. The load, load point displacement and strains near the crack tip were measured as the specimen was loaded. The out of plane displacements near the crack tip was also measured, using optical interferometry. These results were compared to finite element results that modelled in three dimensions the specimen being tested. Excellent agreement of all the measured quantities was obtained between the experimental and numerical results. For the numerical analyst the agreement with the experimental results leaves no doubt that the numerical calculations are accurate and sufficiently detailed to model this specimen well. It was found that for all load levels there is no region on the specimen where the plane stress HRR field accurately described the out of plane displacement field. This is consistent with the caustics results that show that caustics based on the HRR fields cannot be used to accurately measure J.

REFERENCES

1. *Proceedings: Workshop on Dynamic Fracture,* Knauss, W.G. et al., eds. California Institute of Technology, 1983.

2. *Dynamic Fracture,* Special issue of *International Journal of Fracture,* Vol. 27, Nos. 3-4, 1985.

3. *Dynamic Fracture Mechanics, The Albert Kobayashi Anniversary Volume,* Special issue of *Engineering Fracture Mechanics,* Vol. 23, No. 1, 1986

4. Narasimhan, R., "Mode-I, Plane Stress Crack Initiation and Growth in Elastic-Plastic Solids: A Finite Element Analysis," Ph.D. Thesis, 1986, California Institute of Technology. Also Narasimhan, R., and Rosakis, A.J., "Finite Element Analysis of Small Scale Yielding Near a Stationary Crack Under Plane Stress," GALCIT Report SM 86-21, California Institute of Technology, 1986.

5. Rice, J.R., "A Path Independent Integral and the Approximate Analysis of Strain Concentration by Notches and Cracks," *Journal of Applied Mechanics,* Vol. 35, 1968, pp. 379-386.

6. Hutchinson, J.W. "Singular Behaviour at the End of a Tensile Crack in a Hardening Material," *Journal of the Mechanics and Physics of Solids,* Vol. 16, 1968, pp. 13-31.

7. Rice, J.R., and Rosengren, G.F., "Plane Strain Deformation Near a Crack Tip in a Power-Law Hardening Material," *Journal of the Mechanics and Physics of solids,* Vol. 16, 1968, pp. 1-12.

8. Zehnder, A.T., and Rosakis, A.J., "Dynamic Fracture Initiation and Propagation in 4340 Steel Under Impact Loading," GALCIT Report SM86-6, California Institute of Technology, 1986, to appear in an *ASTM Special Technical Publication on Nonlinear Fracture Mechanics,* Proceedings of the Third International Symposium on Nonlinear Fracture Mechanics, Knoxville, TN, Oct. 6-8, 1986.

9. Zehnder, A.T., and Rosakis, A.J., "A Note on the Measurement of K and J Under Small Scale Yielding Conditions Using the Method of Caustics," *International Journal of Fracture* Vol. 30, 1986, pp. R43-R48.

10. Zehnder, A.T., Rosakis, A.J., and Narasimhan, R., "Measurement of the J Integral With Caustics: An Experimental and Numerical Investigation," GALCIT Report SM86-8, California Institute of Technology, 1986, to appear in an *ASTM Special Technical Publication on Nonlinear Fracture Mechanics,* Proceedings of the Third International Symposium on Nonlinear Fracture Mechanics, Knoxville, TN, Oct. 6-8, 1986

11. Schardin, H., "Velocity Effects in Fracture," in *Fracture,* Averbach et al. (eds.), John Wiley and Sons, 1959.

12. Manogg, P., "Anwendungen der Schattenoptik zur Untersuchung des Zerreissvorgags von Platten," Ph.D. Thesis, Freiburg, West Germany, 1964.

13. Beinert, J., and Kalthoff, J.F., "Experimental Determination of Dynamic Stress Intensity Factors by the Method of Shadow Patterns," in *Mechanics of Fracture,* Vol. VII, G. Sih (ed.), Sijthoff and Noordhoff, 1981, pp. 281-320.

14. Theocaris, P.S., "Elastic Stress Intensity Factors Evaluated by Caustics," in *Mechanics of Fracture,* Vol VII, G. Sih (ed.), Sijthoff and Noordhoff, 1981.

15. Goldsmith, W., and Katsamanis, F., "Fracture of Notched Polymeric Beams Due to Central Impact," *Experimental Mechanics,* Vol. 19, 1979, pp. 235-244.

16. Ravi-Chandar, K., and Knauss, W.G., "Dynamic Crack-Tip Stresses Under Stress Wave Loading - A Comparison of Theory and Experiment," *International Journal of Fracture,* Vol. 20, 1982, pp. 209-222.

17. Rosakis, A.J., Duffy, J., and Freund, L.B., "The Determination of Dynamic Fracture Toughness of AISI 4340 Steel by the Shadow Spot Method" *Journal of the Mechanics and Physics of Solids,* Vol 32, 1984, pp. 443-460.

18. Rosakis, A.J., and Zehnder, A.T., "On the Method Of Caustics: An Exact Analysis Based on Geometrical Optics," *Journal of Elasticity,* Vol. 15, 1985, pp.347-367.

19. Williams, M.L., "On the Stress Distribution at the Base of a Stationary Crack," *Journal of Applied Mechanics,* Vol 24, 1957, pp. 109-114.

20. Rosakis, A.J., and Ravi-Chandar, K., "On Crack Tip Stress State: An Experimental Evaluation of Three Dimensional Effects," *International Journal of Solids and Structures,* Vol. 22, 1986, pp. 121-138.

21. Rosakis, A.J., Ma, C.C., and Freund, L.B., "Analysis of the Optical Shadow Spot Method for a Tensile Crack in a Power-Law Hardening Material," *Journal of Applied Mechanics,* Vol. 105, 1983, pp. 777-782.

22. Rosakis, A.J., and Freund, L.B., "Optical Measurement of the Plastic Strain Concentration at a Crack Tip in a Ductile Steel Plate," *Journal of Engineering Materials and Technology,* Vol. 104, 1982, pp. 115-120.

23. Marchand, A., Freund, L.B., Ma, C.C., and Duffy, J., "Use of the Shadow Spot Method in Evaluating J for Ductile Steels," Brown University Technical Report, ONR 0597/1, MRL E-160, February 1986.

24. Freund, L.B., and Clifton, R.J., "On the Uniqueness of Plane Elastodynamic Solutions for Running Cracks," *Journal of Elasticity,* Vol 4, 1974, pp. 293-299.

25. Freund, L.B., "The Mechanics of Dynamic Fracture," in Proceedings of the Tenth U.S. National Congress of Applied Mechanics, Austin, TX, 1986.

26. Lam, P.S. and Freund, L.B., "Analysis of Dynamic Crack Growth of a Tensile Crack in an Elastic- Plastic Material," *Journal of the Mechanics and Physics of Solids,* Vol. 33, 1985, pp. 153-167.

27. Brickstad, B. "A FEM Analysis of Crack Arrest Experiments," *International Journal of Fracture,* Vol. 21, 1983, pp. 177-194.

28. Kanazawa, T., Machida, S., Teramoto, T., and Yoshinari, H., "Study on Fast Fracture and Crack Arrest," *Experimental Mechanics,* Vol. 38 1981, pp. 78-88.

29. Bilek, Z., "Some Comments on Dynamic Crack Propagation in a High Strength Steel," in *Crack Arrest Methodology and Applications, ASTM STP 711,* American Society for Testing and Materials, 1980, pp. 240-247.

30. Dally, J.W., in *Optical Methods in Mechanics of Solids,* A. Lagarde ed., Sijthoff and Noordhoff, 1980, p. 692.

31. Ravi-Chandar, K. and Knauss, W.G., *International Journal of Fracture,* Vol. 25, 1984, pp. 247-262; Vol. 26, 1984, pp. 65-80, pp. 141-154, pp. 193-204.

32. Kobayashi, T., and Dally, J.W., "Dynamic Photoelastic Determination of the $\dot{a}$-K Relation for High Strength Steel," in *Crack Arrest Methodology and Applications, ASTM STP 711,* American Society for Testing and Materials, 1980, pp. 189-210.

33. Rosakis, A.J., Duffy, J., and Freund, L.B., in *Proceedings, "Workshop on Dynamic Fracture,"* W.G. Knauss et al., eds. California Institute of Technology, 1983, pp. 100-118.

34. Freund, L.B., and Douglas, A., "The Influence of Inertia on Elastic Plastic Antiplane Shear Crack Growth," *Journal of the Mechanics and Physics of Solids,* Vol. 30, 1982, pp. 59-74

35. Freund, L.B., and Hutchinson, J.W., "High Strain-Rate Crack Growth in Rate-Dependent Plastic Solids," *Journal of the Mechanics and Physics of Solids,* Vol. 33, 1985, pp. 169-191.

36. Freund, L.B., and Douglas, A.S., "Dynamic Growth of an Antiplane Shear Crack in a Rate-Sensitive Elastic-Plastic Material," in *Elastic-Plastic Fracture: Second Symposium, Volume I - Inelastic Crack Analysis,* ASTM STP 803, Shih and Gudas, eds., American Society for Testing and Materials, 1983, pp. 5-20.

37. Rice, J.R., and Levy, N., "Local Heating by Plastic Deformation at a Crack Tip," in *Physics of Strength and Plasticity,* Ali Argon, ed., MIT Press, 1969.

38. Kuang, Z-B., and Atluri, S.N., "Temperature Field Due to a Moving Heat Source: A Moving Mesh Finite Element Analysis," *Journal of Applied Mechanics,* Vol. 52, 1985, pp. 274-280.

39. Hahn, G.T., et al., Reports to the U.S. Nuclear Regulatory Comission, Batelle Columbus Laboratories, 1974-1976.

40. Angelino, G.C., "Influence of the Geometry on Unstable Crack Extension and Determination of Dynamic Fracture Mechanics Parameters," in *Fast Fracture and Crack Arrest, ASTM STP 627,* American Society for Testing and Materials, 1978, pp. 392-407.

41. Kobayashi, A.S., et al., "Dynamic Fracture Toughness," *International Journal of Fracture,* Vol. 30, 1986, pp. 275-286.

42. Hudak, S.J., et al., "The Influence of Specimen Boundary Conditions on the Fracture Toughness of Running Cracks," *Engineering Fracture Mechanics,* Vol. 23, 1986, pp. 201-213.

43. Dexter, R.J., "Sources of Error in Finite Element Computations of the Stress Intensity Factor for Running Cracks," *Numerical Methods in Fracture Mechanics,* Proceedings of the Fourth International Conference, San Antonio, Texas, March 1987, pp. 153-172.

44. Kanninen, M.F., "Application of Dynamic Fracture Mechanics for the Prediction of Crack Arrest in Engineering Structures," *International Journal of Fracture,* Vol. 27, 1985, pp. 299-312.

45. Emery, A.F., Walker, G.E., Williams, J.A., "A Green's Function for the Stress-Intensity Factor of Edge Cracks and its Application to Thermal Stresses," *Journal of Basic Engineering,* Vol. 91, 1969, pp. 618-624.

46. ASTM E 24.03.03, "Proposed Standard Method of Test for Instrumented Impact Testing of Precracked Charpy Specimens of Metallic Materials," Draft 2d, 1981.

47. Ireland, D.R., "Critical Review of Instrumented Impact Testing," Proc. International Conference on Dynamic Fracture Toughness, London, 1976.

48. Kalthoff, J.F., Bohme, W., Winkler, S., and Klemm, W., "Measurements of Dynamic Stress Intensity Factors in Impacted Bend Specimens," CSNI Specialist Meeting on Instrumented Precracked Charpy Testing, Electric Power Research Institute, Palo Alto, CA, 1980.

49. Kalthoff, J.F., Winkler, S., Klemm, W., and Beinert, J., "On the Validity of K_{Id}-Measurements in Instrumented Impact Tests," Proceedings, 5th International Conference on Structural Mechanics in Reactor Technology, Berlin, 1979, G 4/5.

50. Rosakis, A.J., and Zehnder, A.T., "On the Dynamic Fracture of Structural Metals," *International Journal of Fracture,* Vol. 27, 1985, pp. 169-186.

51. Kalthoff, J.F., Beinert, J., Winkler, S., and Klemm, W., "Experimental Analysis of Dynamic Effects in Different Crack Arrest Test Specimens," in *Crack Arrest Methodolgy and Applications, ASTM STP 711,* American Society for Testing and

Materials, 1980, pp. 109-127.

52. Kanninen, M.F., Popelar, C., and Gehlen, P.C., "Dynamic Analysis of Crack Propagation and Arrest in the Double Cantilever Beam Specimen," in *Fast Fracture and Crack Arrest,* ASTM STP 627, American Society for Testing and Materials, 1977, pp. 19-38.

53. Theocaris, P.S., and Georgiadis, H.G., "Rayleigh Waves Emitted by a Propagating Crack in a Strain-Rate Dependent Elastic Medium," *Journal of the Mechanics and Physics of Solids,* Vol 32, 1984, pp. 491-510.

54. Parsons, I.D., Hall, J.F., and Rosakis, A.J., "A Finite Element Investigation of the Elastostatic State Near a Three Dimensional Edge Crack", GALCIT Report SM86-29, California Institute of Technology, 1986.

55. Tetelman, A.S., and McEvily, A.J., *Fracture of Structural Materials,* John Wiley and Sons, N.Y., 1967, pp.529-539.

56. Bucher, J., et al., AFML Dept. TR-65-60, 1965

57. Chi, Y.C., Lee, H.S., and Duffy, J., "The Effects of Tempering Temperature and Test Temperature on the Dynamic Fracture Initiation of AISI 4340 VAR Steel", Brown University Report, DAAG29-85-K-0003, March 1987.

58. Judy, R.W., and Sanford, R.J., "Correlation of Optical Caustic Behavior With Fracture Properties of High Strength Steels," to appear in *ASTM Special Technical Publication on Nonlinear Fracture Mechanics,* proceedings of the Third International Symposium on Nonlinear Frature Mechanics, Knoxville, TN, Oct. 6-8, 1986.

59. Tada, H., Paris, P., and Irwin, G., *The Handbook of Stress Intensity Factors* Del Research Corporation, 1973.

60. Kumar, V., German, M.D., and Shih, C.F., "Engineering Approach for Elastic-Plastic Fracture Analysis," EPRI Report NP-1931, July 1981.

61. Loss, F.J., et al., "Fracture Toughness of Light-Water Reactor Pressure Vessel Materials," Naval Research Laboratory Report, April 1975.

62. Narasimhan, R., and Rosakis, A.J., Work in progress, Caltech, 1987.

63. Robinson, J.N., and Tetelman, A.S., "Comparison of Various Methods of Measuring K_{IC} on Small Precracked Bend Specimens That Fracture After General Yield," *Engineering Fracture Mechanics,* Vol. 8, 1967, pp. 301-313.

64. Hecht, E., and Zajac, A., *Optics,* Addison-Wesley Publishing Company, 1979, pp. 322-324.

65. Shih, C.F., Moran, B., and Nakamura, T., "Energy Release Rate Along a Three-Dimensional Crack Front in a Thremally Stressed Body," *International Journal of Fracture,* Vol. 30, 1986, pp. 79-102.

66. Bucci, R.J., et al., "J Integral Estimation Procedures," in *Fracture Toughness, Proceedings of the 1971 National Symposium on Fracture Mechanics, Part II, ASTM STP 514,* American Society for Testing and Materials, 1972, pp. 40-69.

67. Rice, J.R., Paris, P.C., and Merkle, J.G., "Some Further Results of J Integral Analysis and Estimates," in *Progress in Flaw Growth and Fracture Toughness Testing, ASTM STP 536,* American Society for Testing and Materials, 1973, pp. 231-245.

68. Landes, J.D., Walker, H., and Clarke, G.A., "Evaluation of Estimation Procedures Used in J-Integral Testing," in *Elastic-Plastic Fracture Mechanics, ASTM STP 668,* American Society for Testing and Materials, 1979, pp. 266-287.

69. DeCastro, P.M.S.T., Spurrier, J., and Hancock P., "Comparison of J Testing Techniques and Correlation J-COD Using Structural Steel Specimens," *International Journal of Fracture,* Vol. 17, 1981, pp. 83-95.

70. Wu, X.P., and Chiang, F.P., "Three Dimensional Crack Tip Deformation in a Plastically Deformed Three Point Bend Specimen," College of Engineering and Applied Sciences Technical Report No. 475, State University of New York at Stoney Brook, March 1986.

71. Chiang, F.P., and Hareesh, T.V., "Three Dimensional Crack Tip Deformation: An Experimental Study and Comparison to HRR Field," College of Engineering and Applied Sciences Technical Report No. 481, State University of New York at Stoney Brook, Spetember 1986.

72. Kishimoto, Aoki, and Sakata, "On the Path Independent Integral-$\hat{J}$," *Engineering Fracture Mechanics,* Vol 13, 1980, pp. 841-850.

73. Nakamura, T., Shih, C.F., and Freund, L.B., "Elastic-Plastic Analysis of a Dynamically Loaded Circumferentially Notched Round Bar," *Engineering Fracture Mechanics,* Vol. 22, 1985, pp. 437-452.

74. Spencer, A.J.M., "The Dynamic Plane Deformation of an Ideal Plastic- Rigid Solid," *Journal of the Mechanics and Physics of Solids,* Vol. 8, 1960, pp. 262-279.

75. Freund, L.B., private communication provided to the author by A.J. Rosakis.

76. Costin, L.S., Duffy, J., and Freund, L.B., "Fracture Initiation in Metals Under Stress Wave Loading Conditions," in *Fast Fracture and Crack Arrest, ASTM STP 627,* American Society for Testing and Materials, 1977, pp. 301-318.

77. Hoff, R., Rubin, C., and Hahn, G.T., "Strain-Rate Dependence of the Deformation at the Tip of a Stationary Crack," in *Fracture Mechanics: Sixteenth Symposium, ASTM STP 868,* American Society for Testing and Materials, 1985, pp. 409-430.

78. Zuiki, Y., "The Effect of Temperature on Fracture Initiation in 4340 Steel," Sc.M. Thesis, Brown University, 1982.

79. Nakamura, T., Shih, C.F., and Freund, L.B., "Analysis of a Dynamically Loaded Three Point Bend Ductile Fracture Specimen," *Engineering Fracture Mechanics,* Vol. 25, 1986, pp. 323-339.

80. Joyce, J.A., and Hackett, E.M., "An Advanced Procedure for J-R Curve Testing in the Drop Weight Tower," to appear in an *ASTM Special Technical Publication on Nonlinear Fracture Mechanics,* Proceedings of the Third International Symposium on Nonlinear Fracture Mechanics, Knoxville, TN, Oct. 6-8, 1986.

81. Achenbach, J.D., *Wave Propagation in Elastic Solids,* North Holland Publishing Company, 1973, p. 379.

82. Hutchinson, J.W., *A Course on Nonlinear Fracture Mechanics,* The Technical University of Denmark, 1979, pp. 48-51.

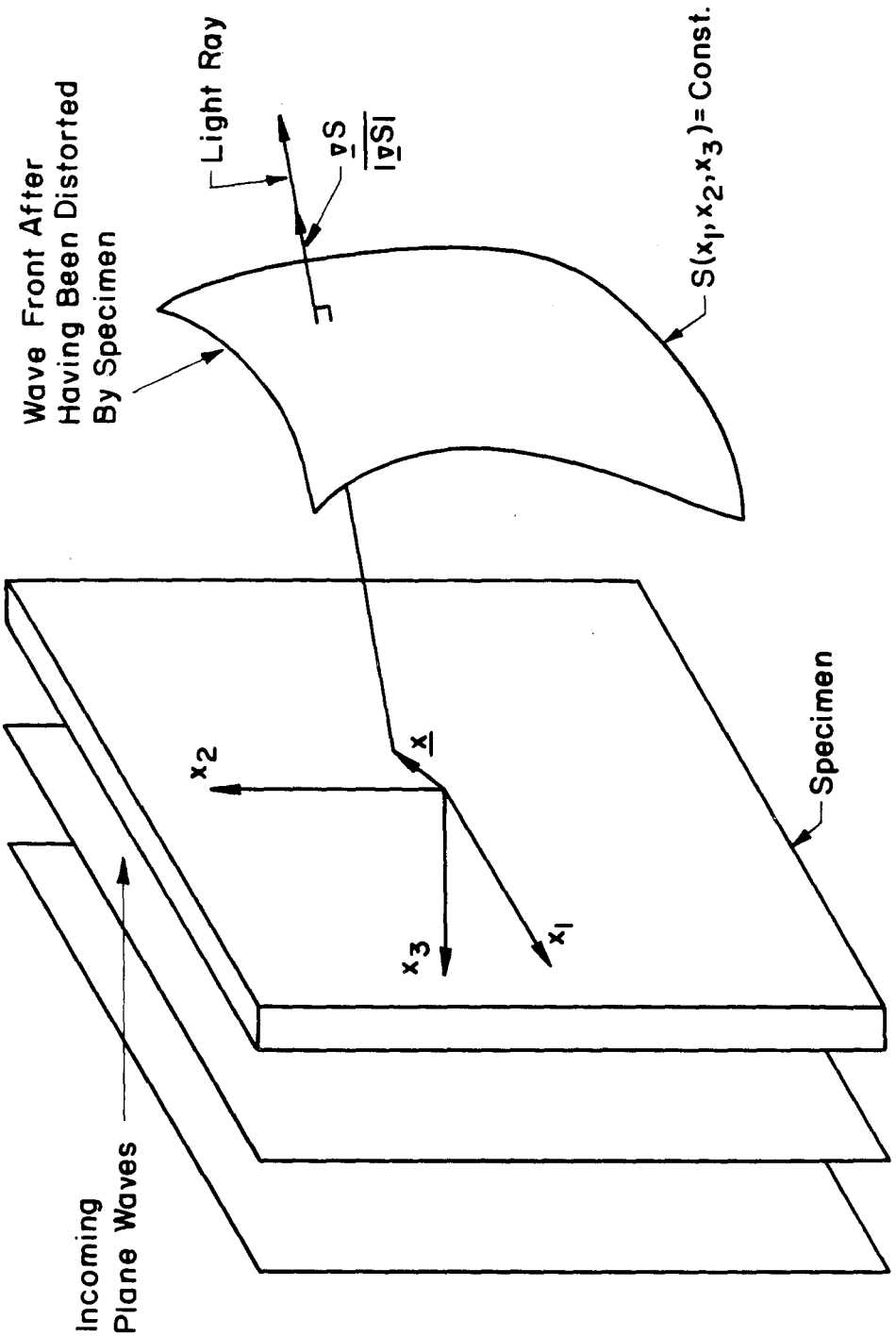

Figure 2.1 Deflection of light rays by specimen.

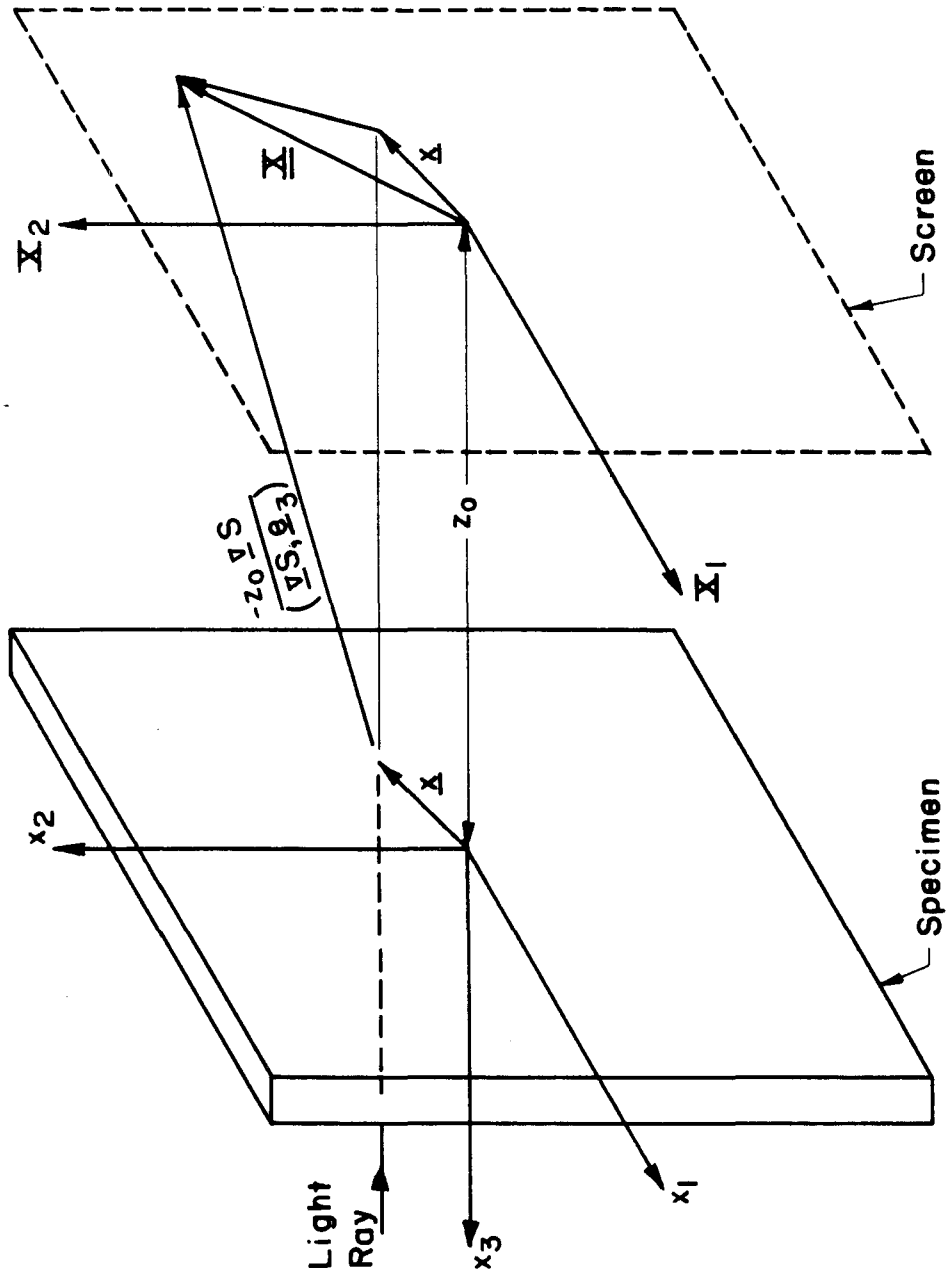

Figure 2.2 General Optical Mapping

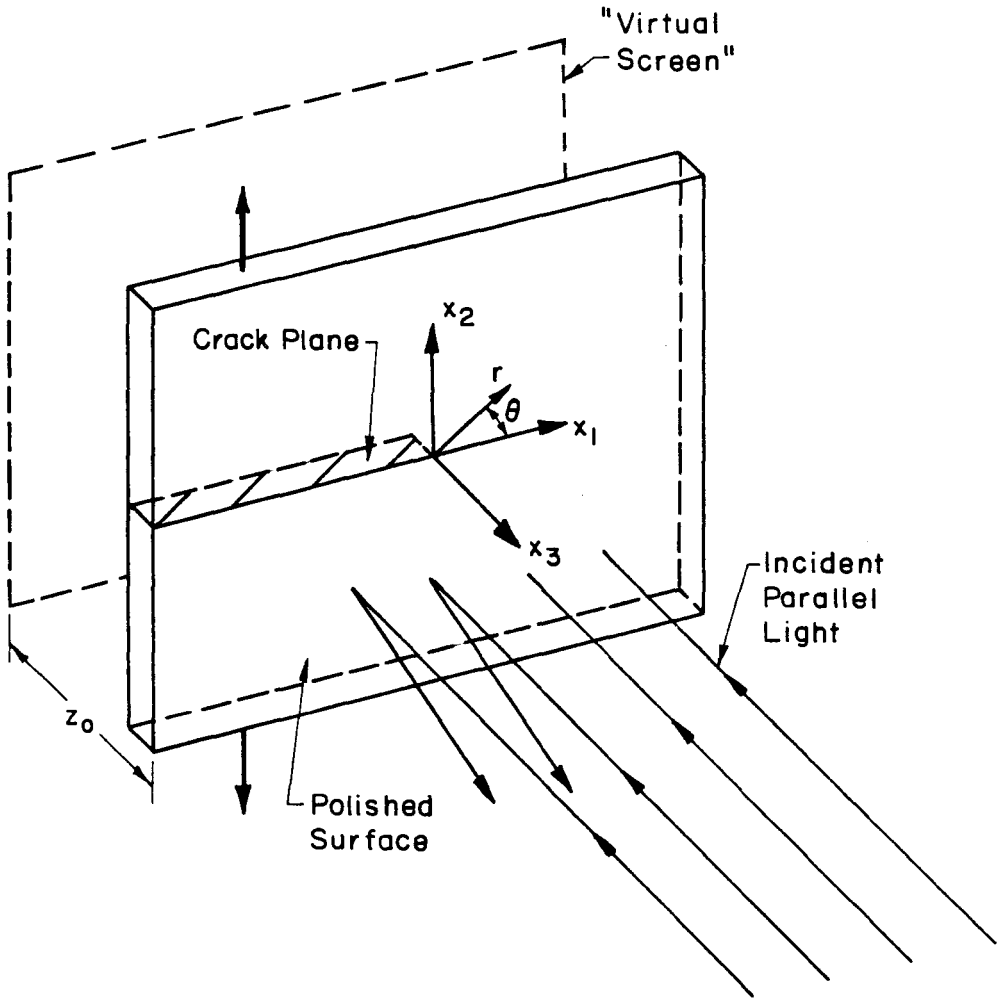

Figure 2.3 Specimen and optical arrangement for reflected caustics. Surface is polished to a mirror finish.

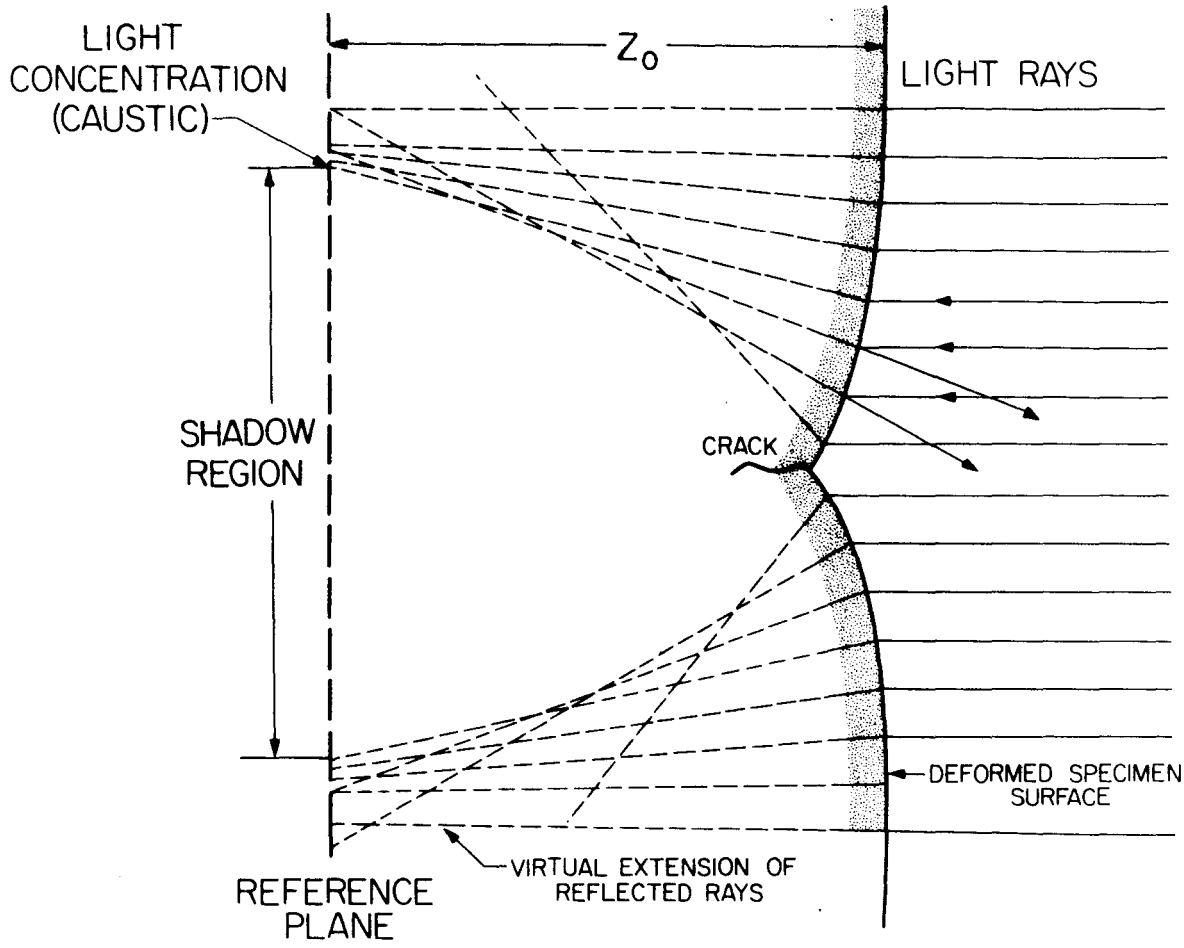

Figure 2.4 Formation of caustic due to reflection of light from the polished, deformed specimen surface near the crack tip.

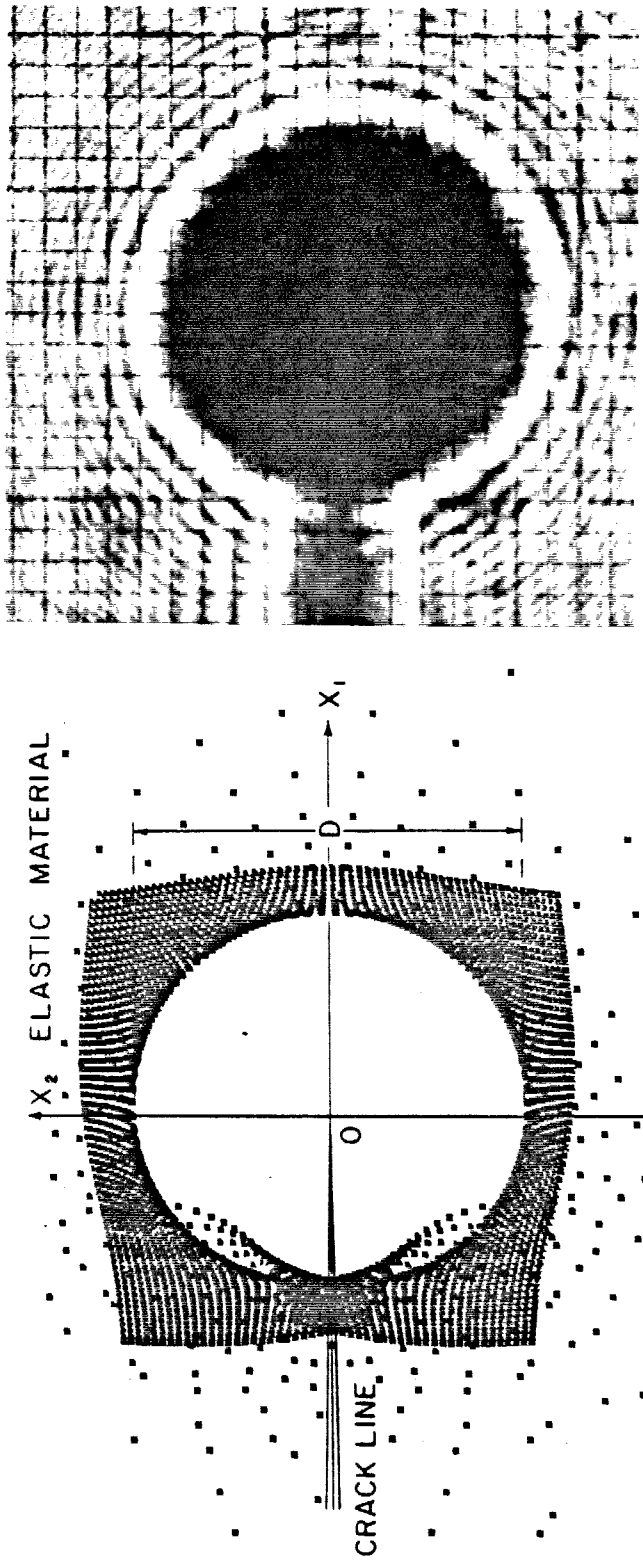

Figure 2.5 Caustics formed due to reflection of light from outside crack tip plastic zone. (a) Numerically simulated (b) Experimental.

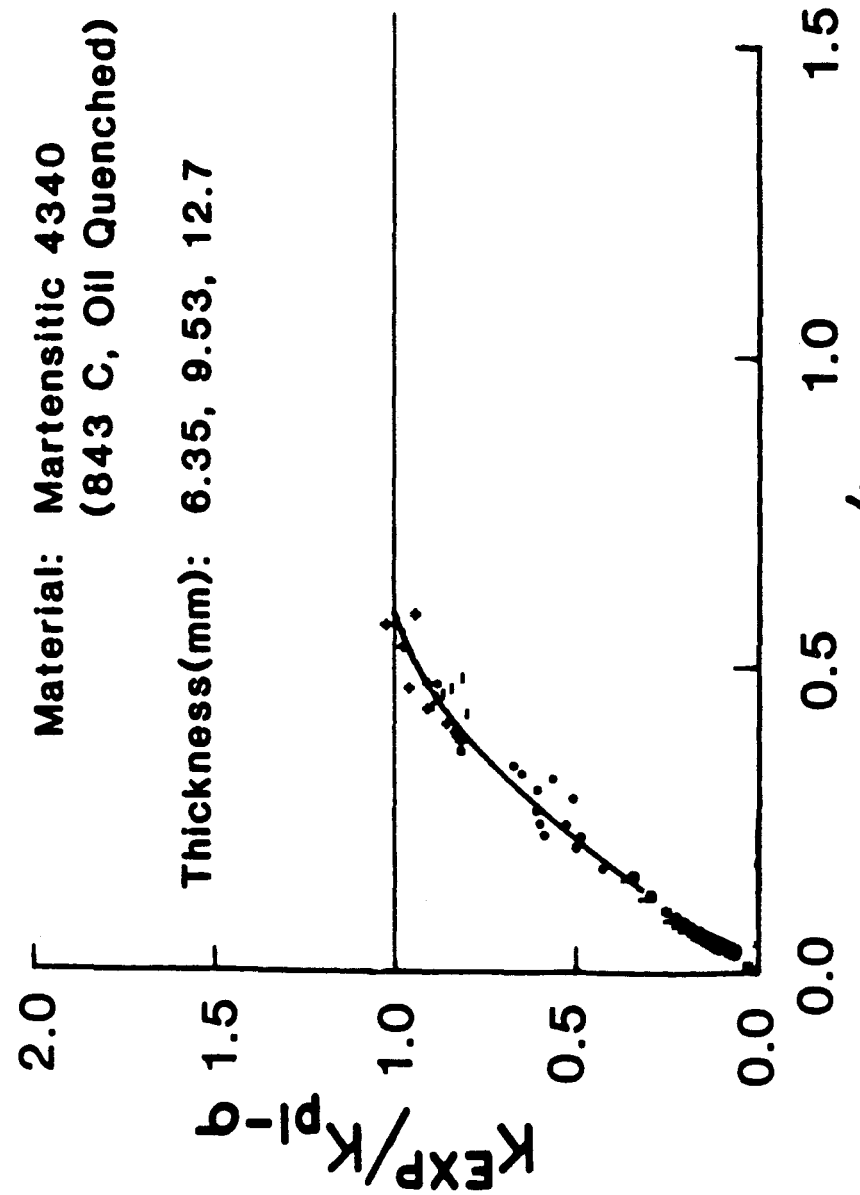

Figure 2.6 Static stress intensity factor as measured by caustics, divided by plane stress value versus distance r from the crack tip, (from Rosakis and Ravi-Chandar [20].)

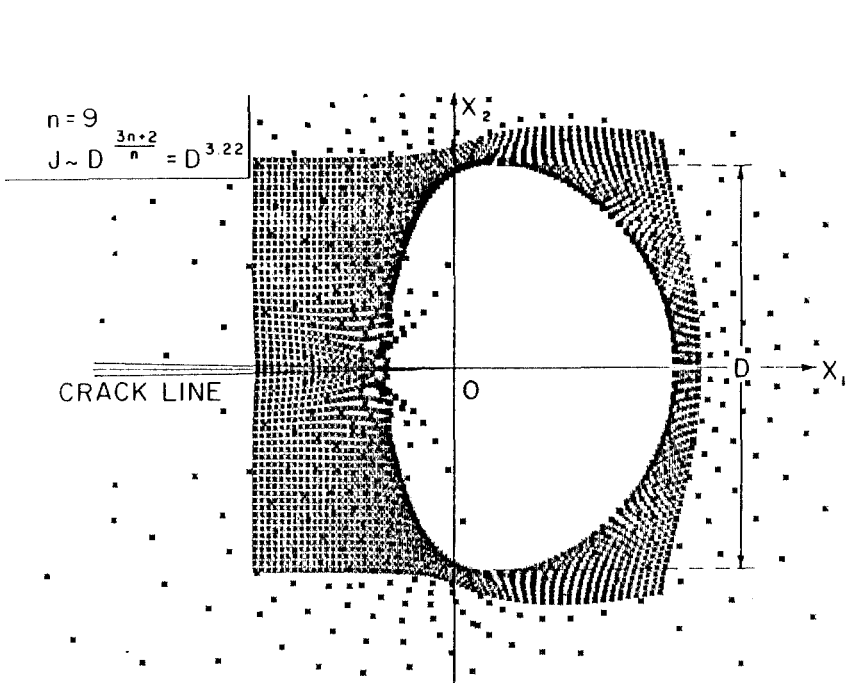

(a)

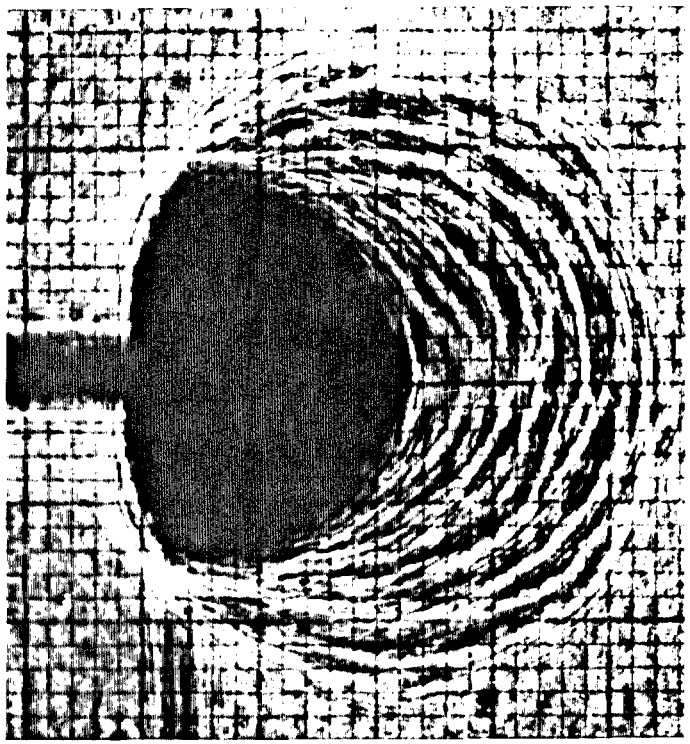

(b)

Figure 2.7 Caustics formed due to reflection of light from within crack tip plastic zone. (a) Numerically simulated (from Rosakis et al. [21]) (b) Experimental.

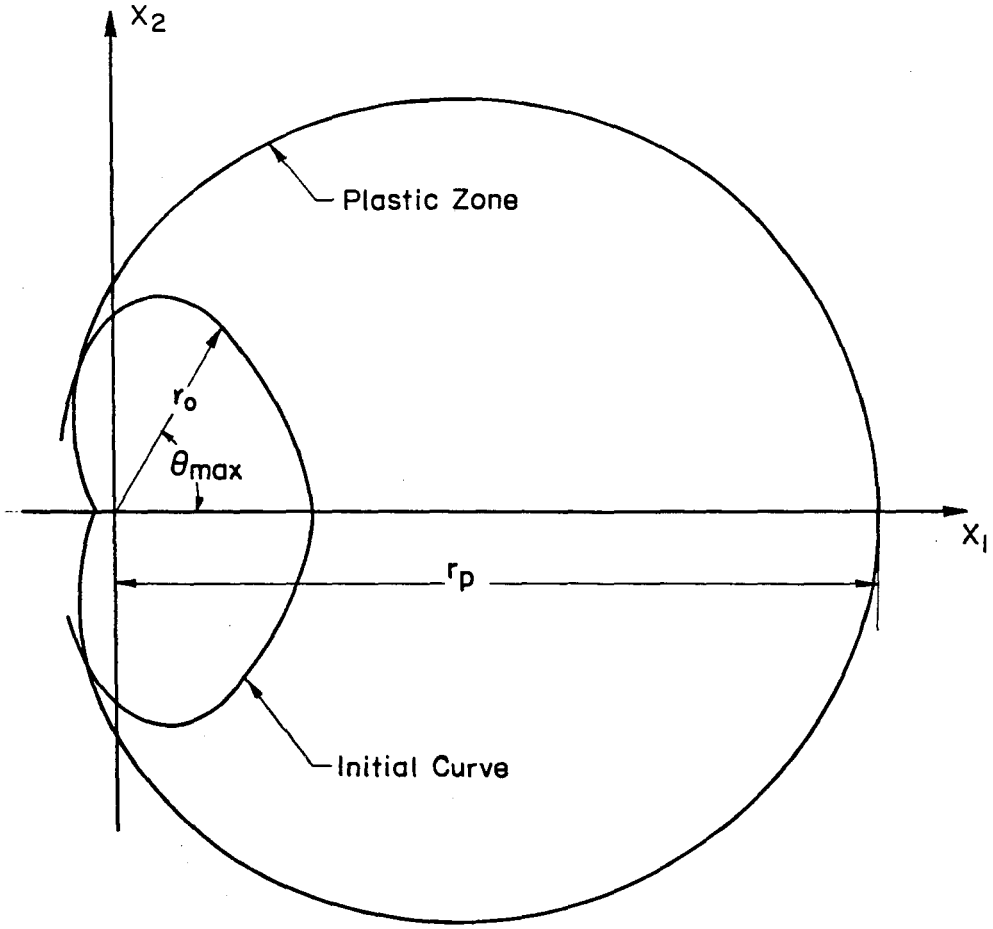

Figure 2.8 Initial curve and plastic zone geometries for an initial curve within the HRR dominant region.

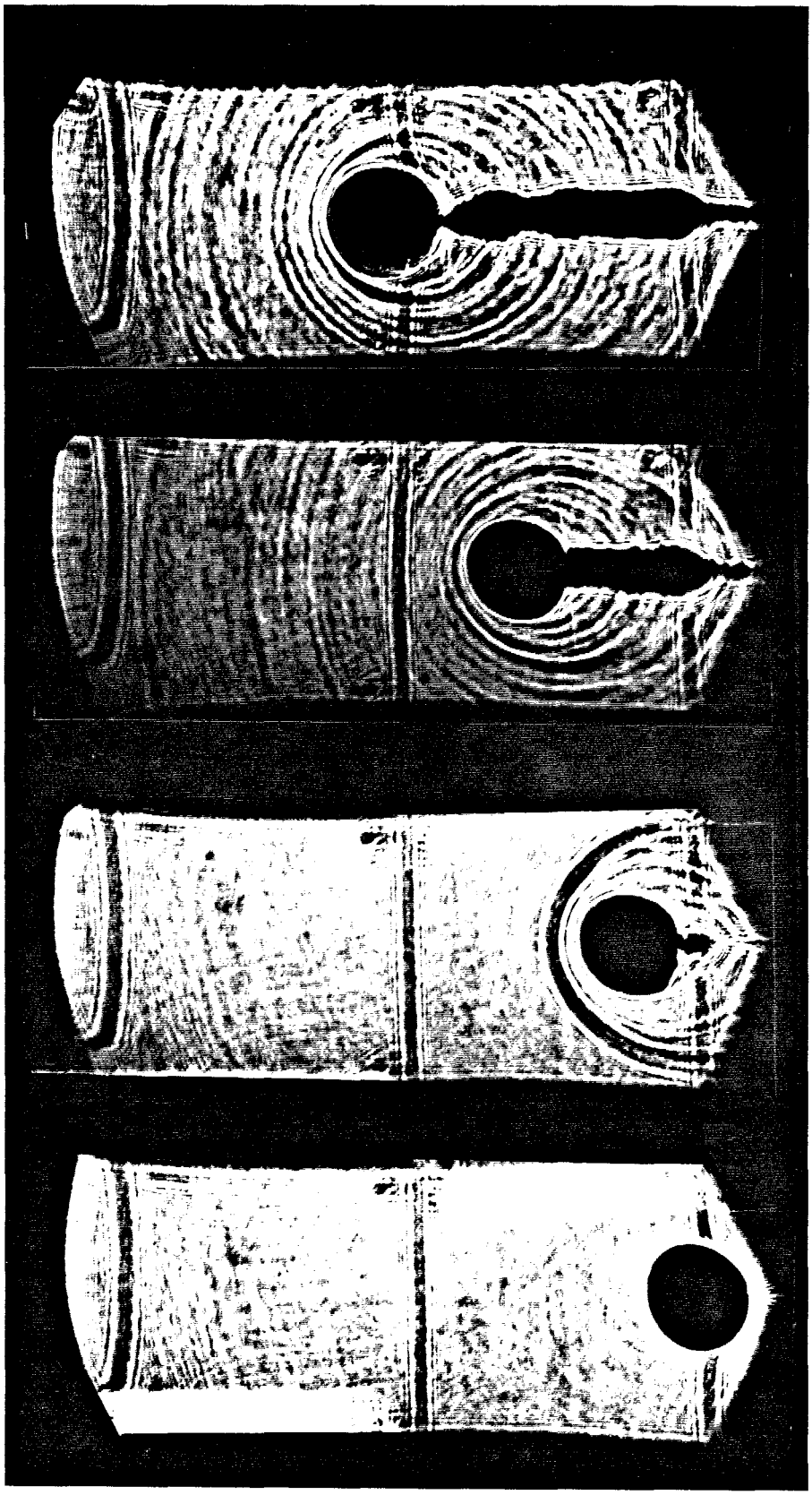

Figure 2.9 Caustics formed by a dynamically propagating crack.

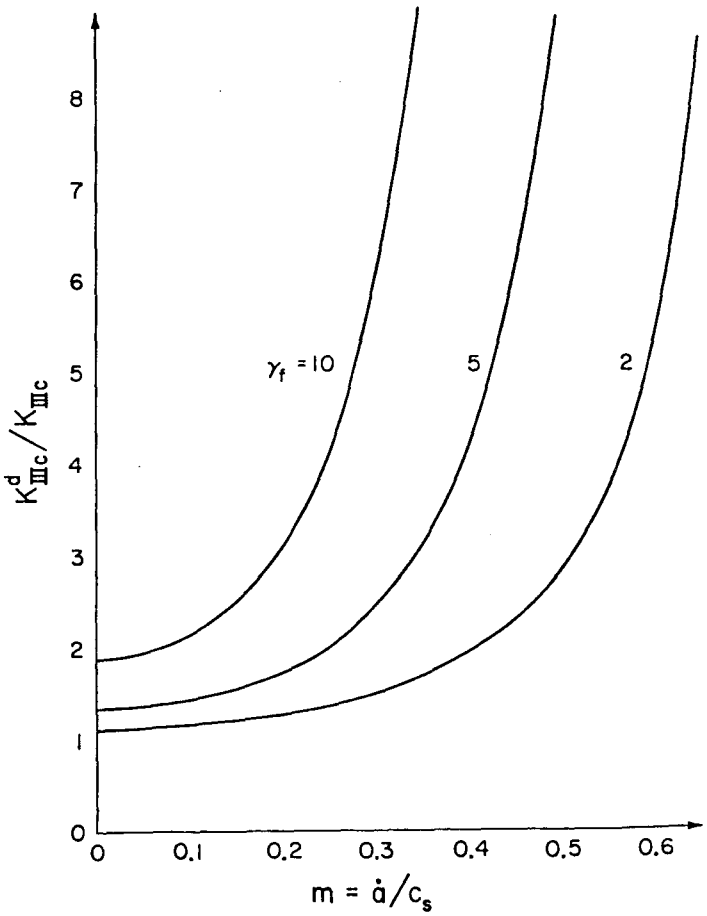

Figure 3.1

Mode III dynamic fracture toughness as a function of crack speed in an elastic-ideally plastic, rate insensitive material according to the critical plastic strain criterion. (From Freund and Douglas [34].)

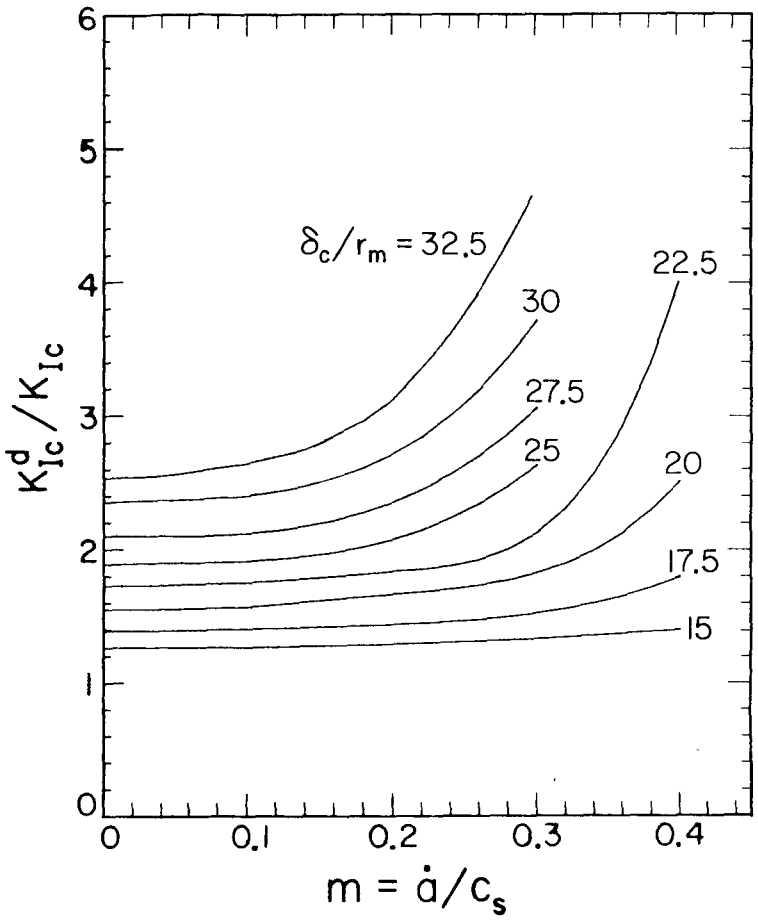

Figure 3.2

Mode I dynamic fracture toughness as a function of crack speed according to the critical crack tip opening angle fracture criterion. (From Lam and Freund [26].)

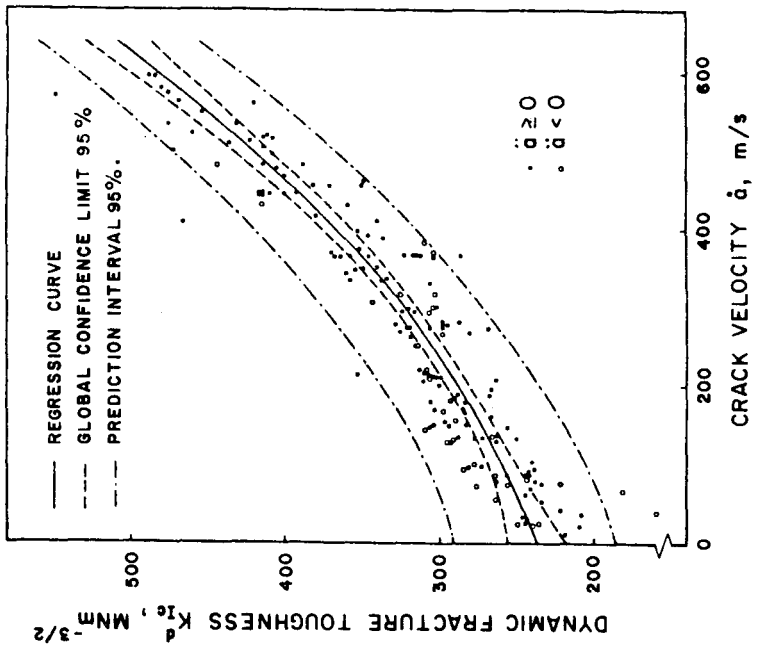

Figure 3.4

Dynamic fracture toughness as a function of crack velocity for a high strength steel. (From Brickstad [27].)

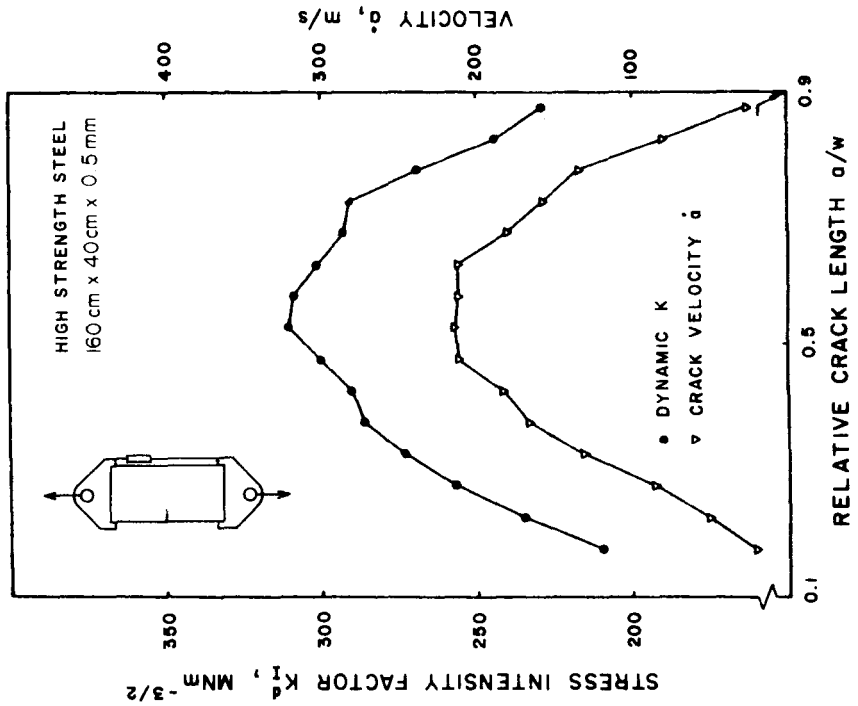

Figure 3.3

Stress intensity factor and crack velocity as functions of crack length. (From Brickstad [27].)

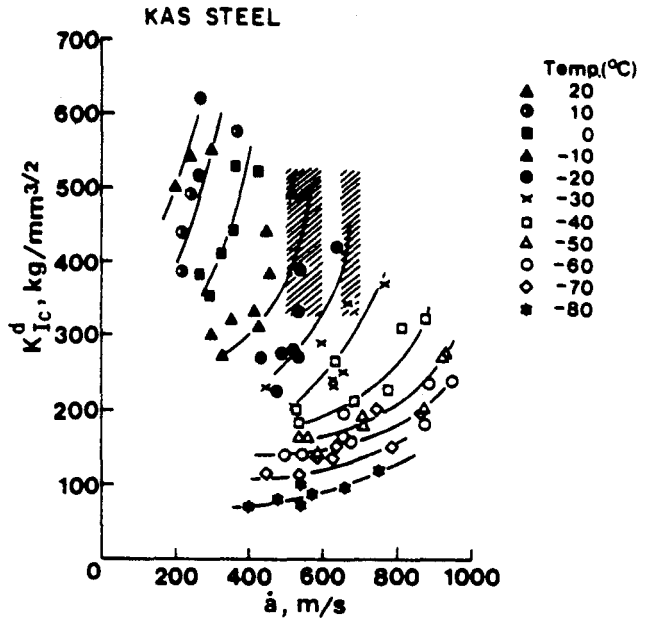

(a)

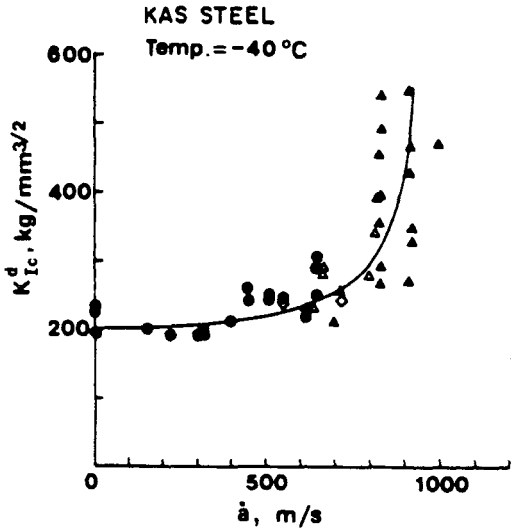

(b)

Figure 3.5 Dynamic fracture toughness as a function of crack tip speed. 100 $kg\ mm^{-3/2} = 31\ MNm^{-3/2}$. (a) For different temperatures. (b) for -40^o C. (from Kanazawa et al. [28].)

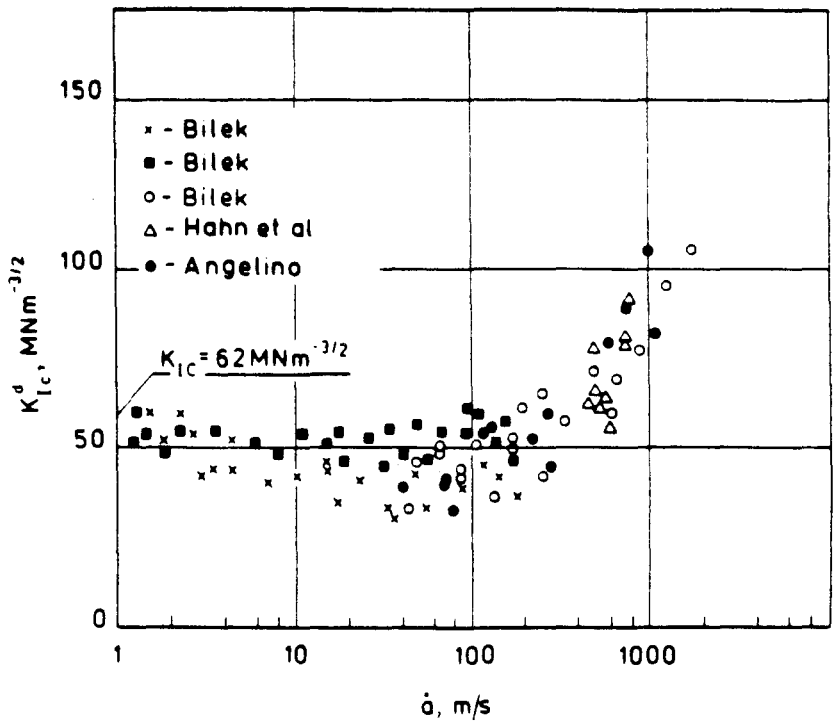

Figure 3.6 Dynamic fracture toughness as a function of crack velocity for 4340 steel. (From Bilek [29].)

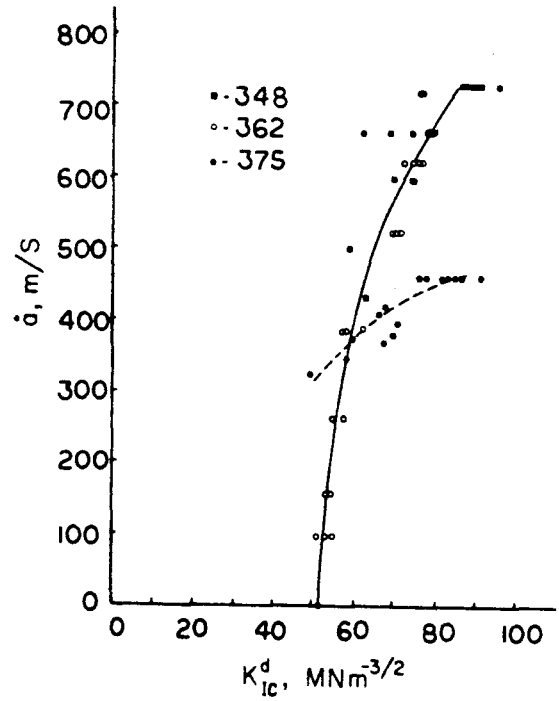

Figure 3.7 Dynamic fracture toughness as a function of crack velocity for a 4340 steel. (From Kobayashi and Dally [32].)

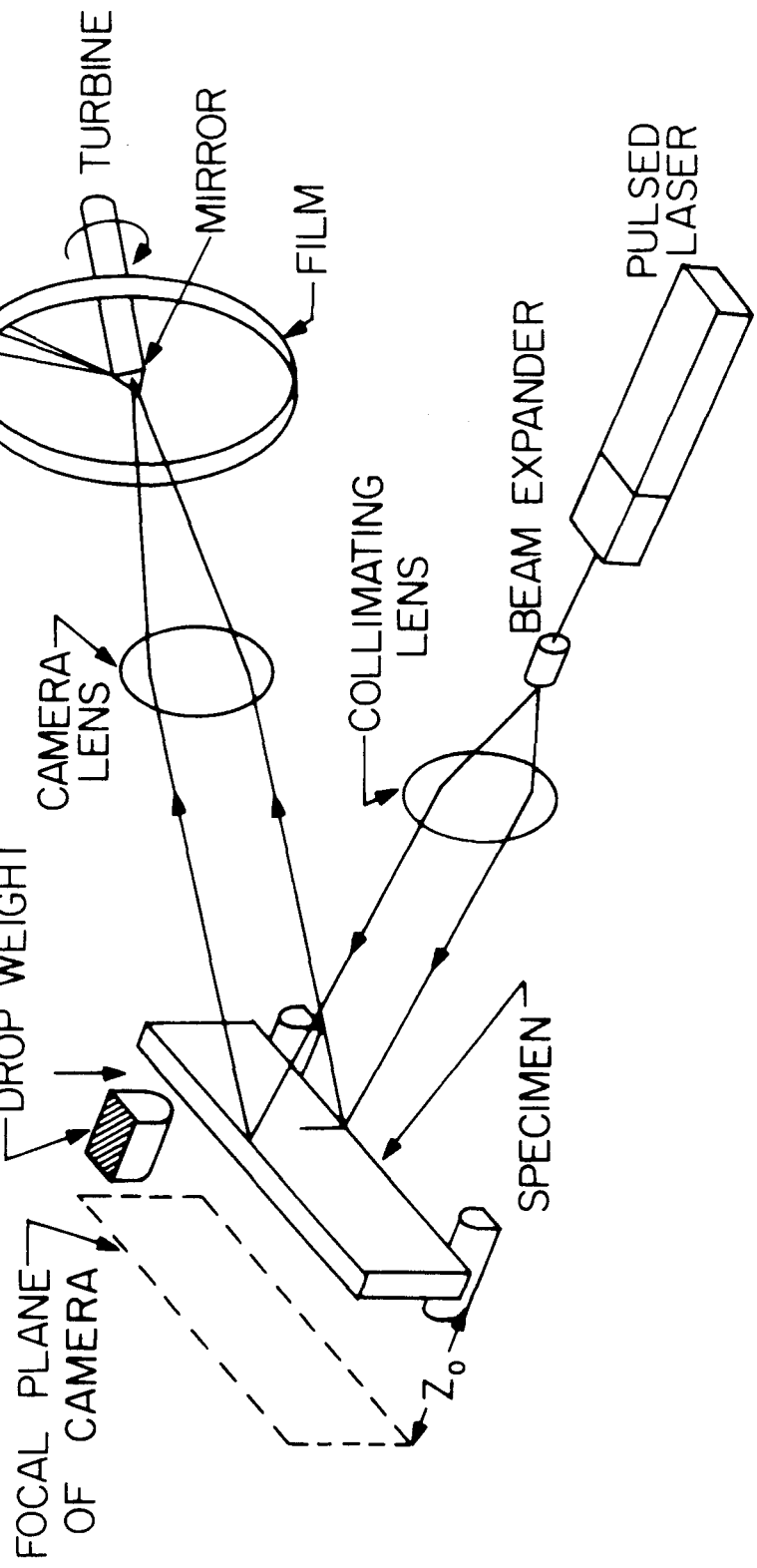

Figure 3.8 Specimen and experimental setup for high speed photography of caustics.

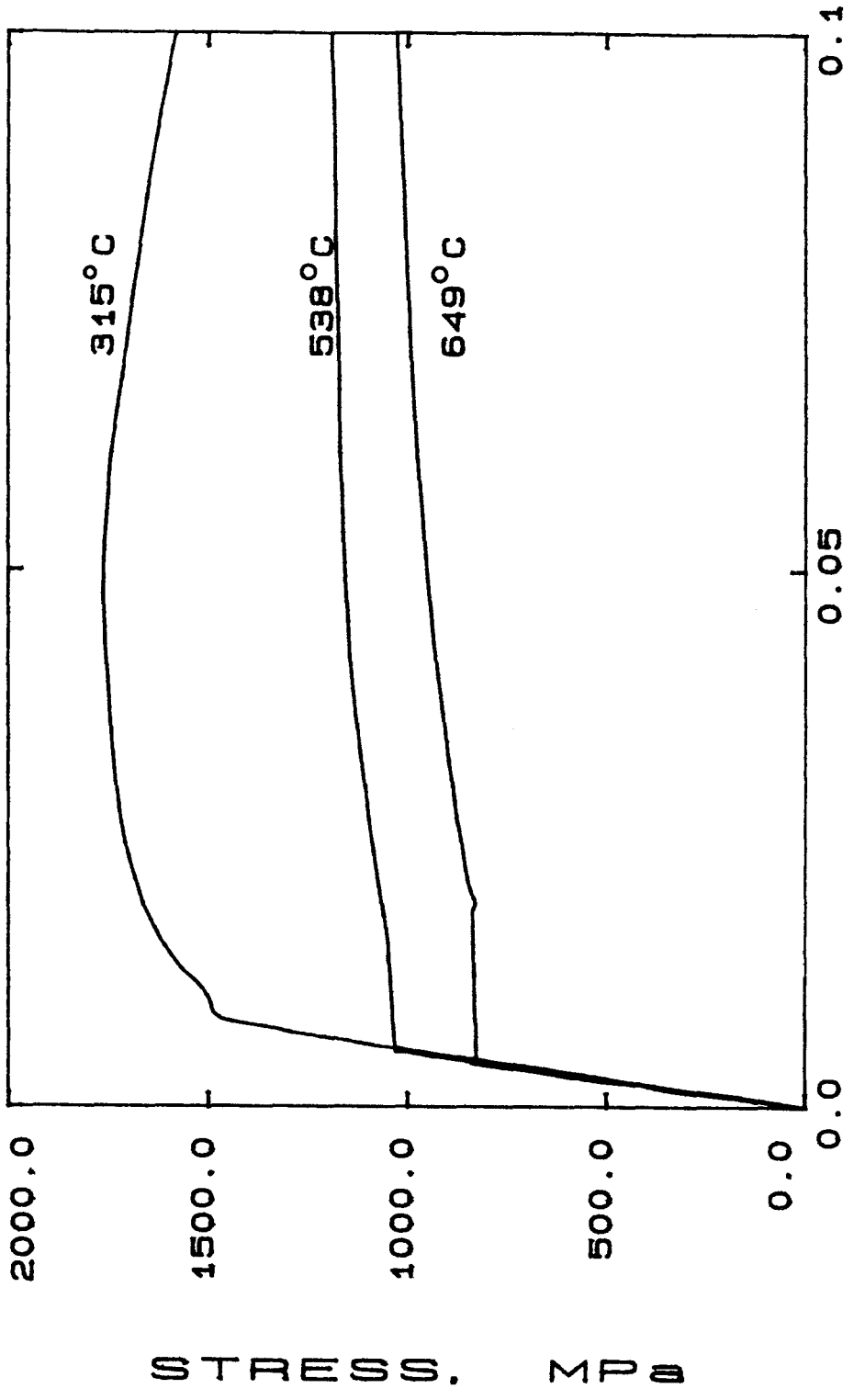

Figure 3.9 Uniaxial stress-strain curves for three heat treatments of 4340 steel. Shown in the figure are the tempering temperatures.

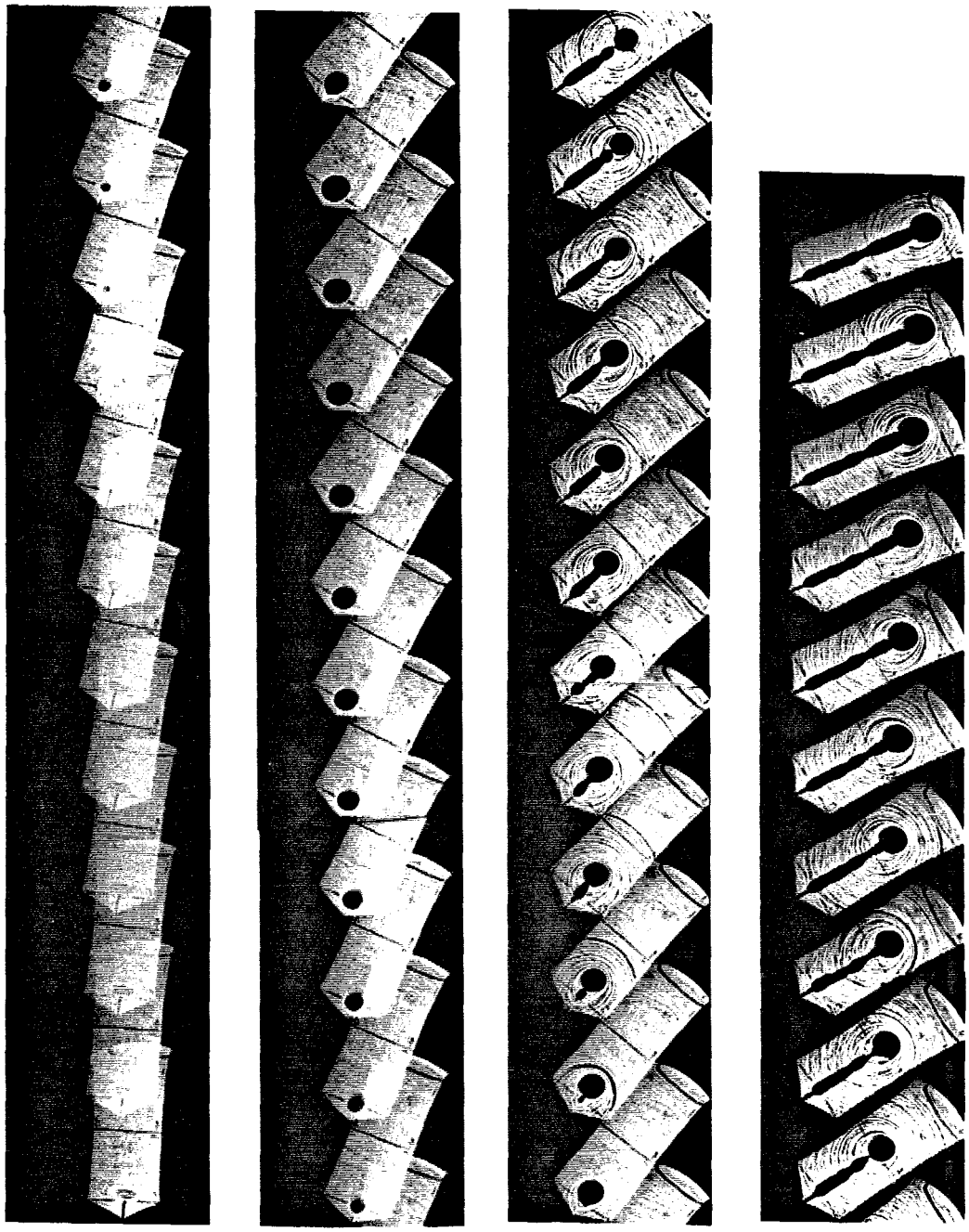

Figure 3.10 Photographs of caustics as they appear on film. Time between frames is 7 μs.

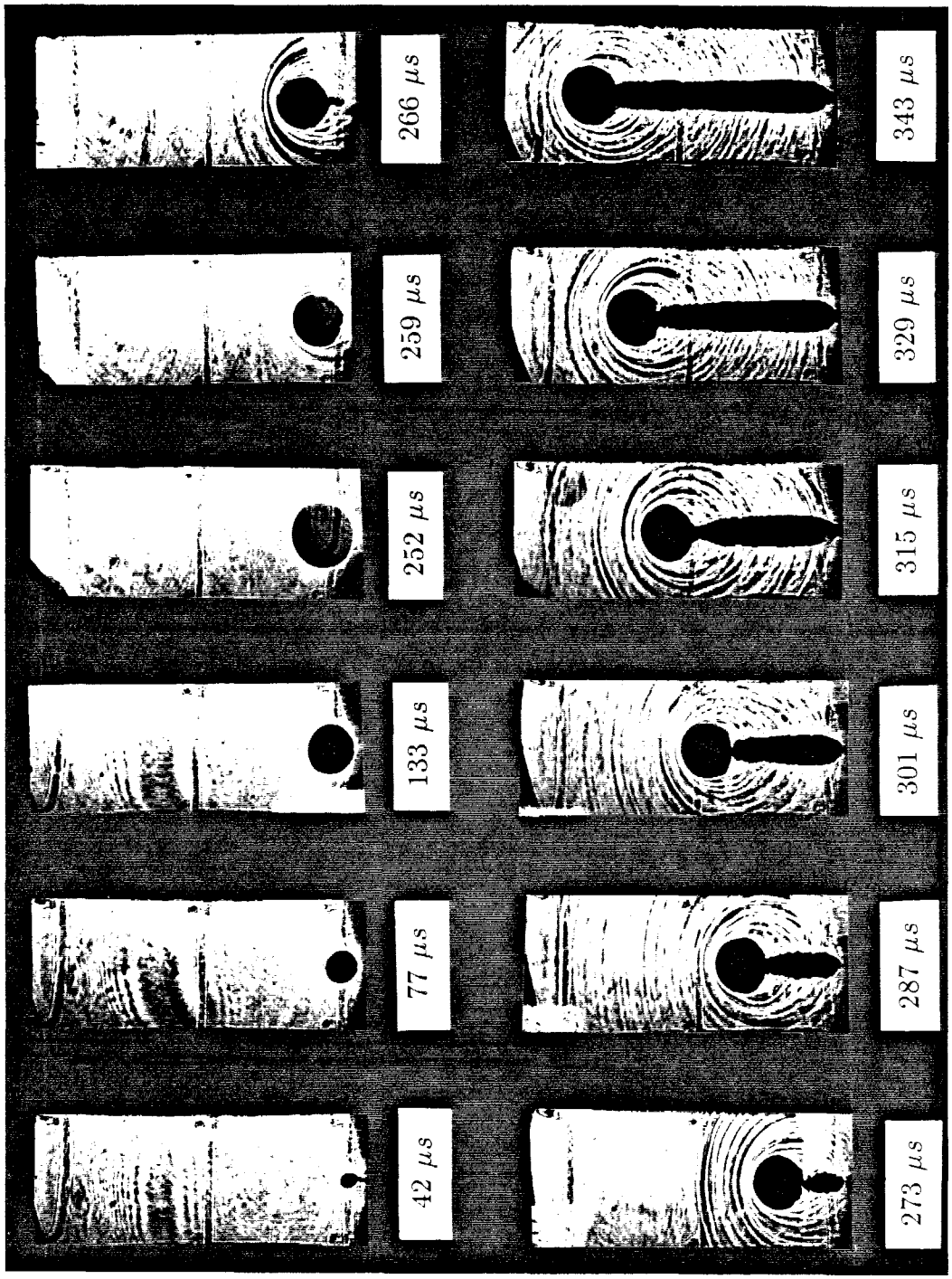

Figure 3.11 Selected photographs showing loading, initiation, and propagation stages of crack growth in a 3-point bend specimen.

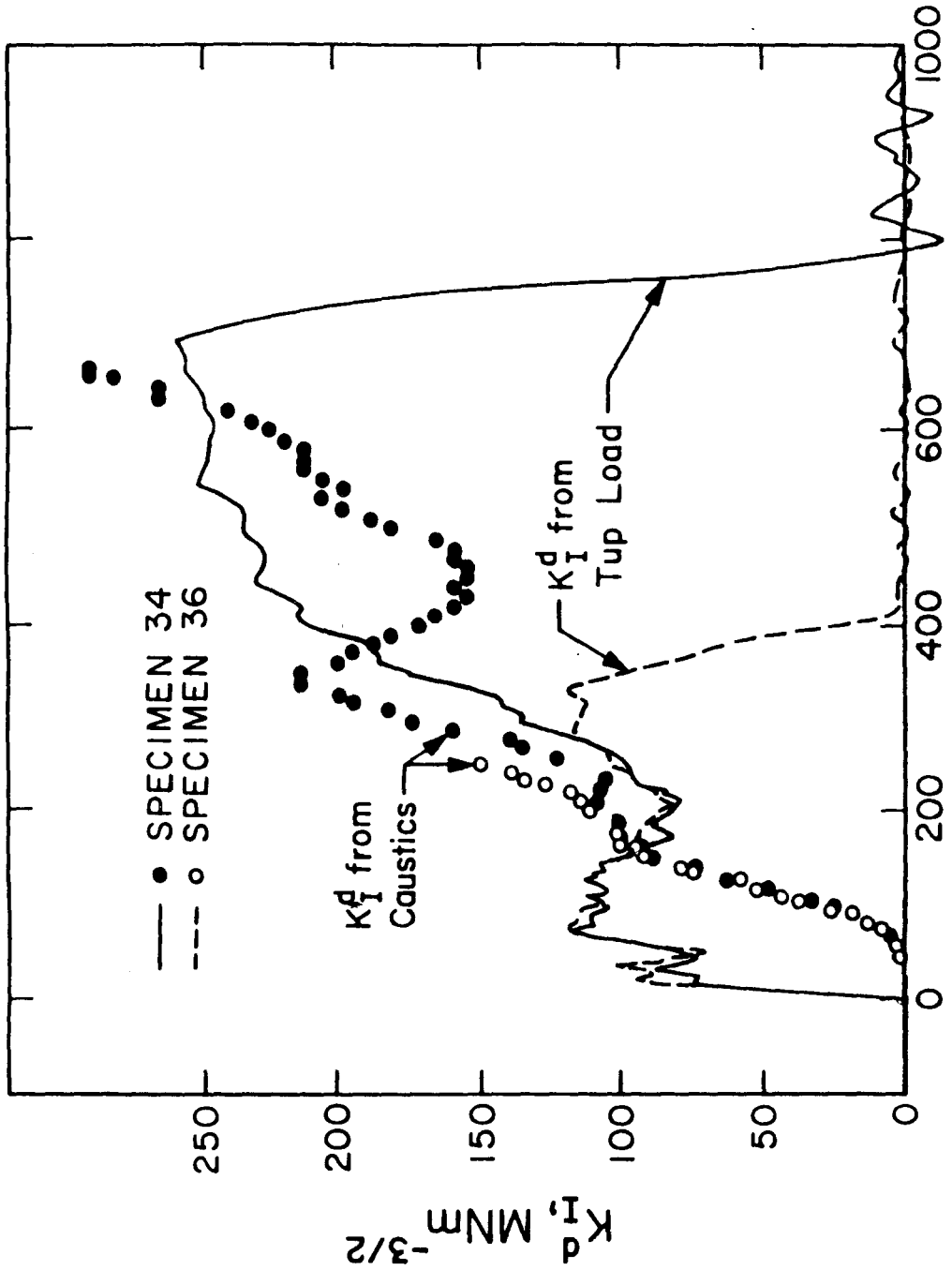

Figure 3.12 Stress intensity factor prior to crack initiation. Both K_I^d calculated from caustics and from the tup load are given. Specimen 34, crack tip diameter $\phi = 1.4$ mm; specimen 36, $\phi = 0.3$ mm.

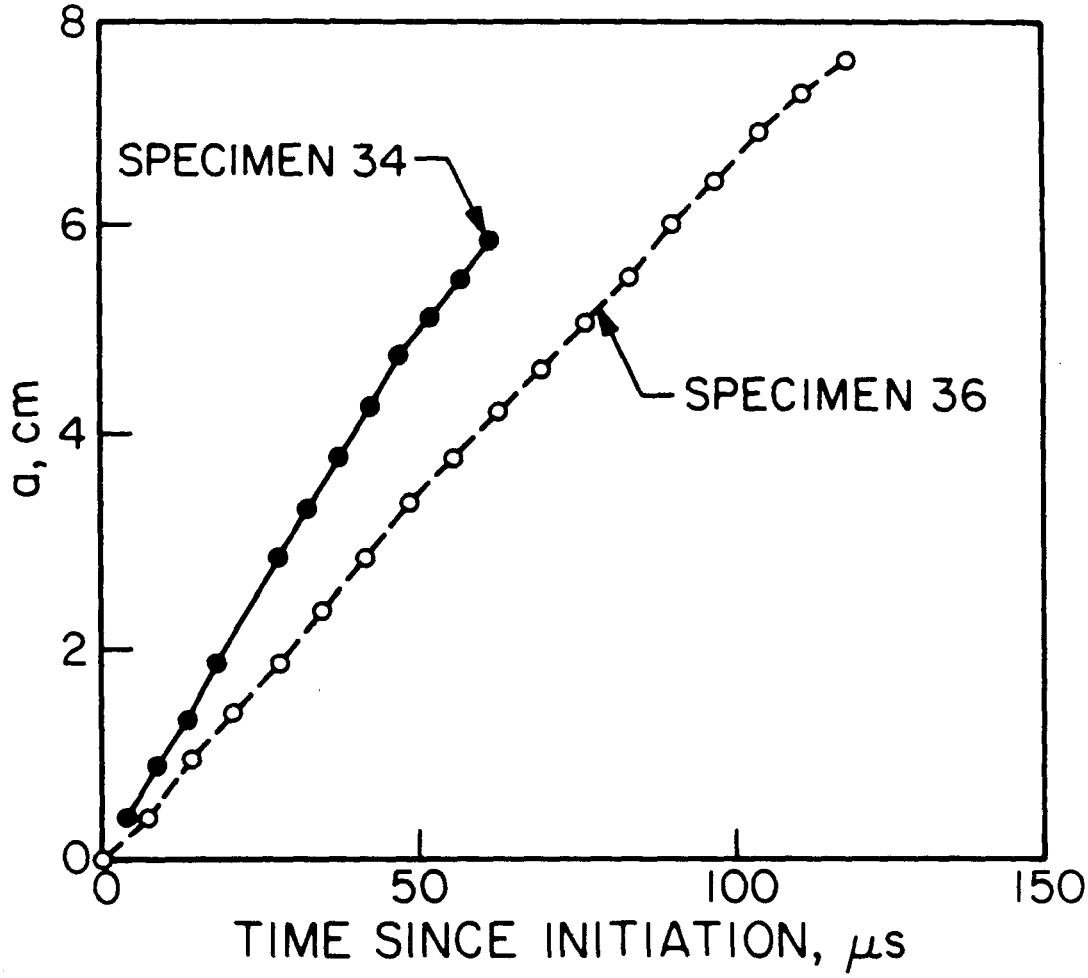

Figure 3.13 Crack length versus time. Specimen 34, crack tip diameter $\phi = 1.4$ mm; specimen 36, $\phi = 0.3$ mm.

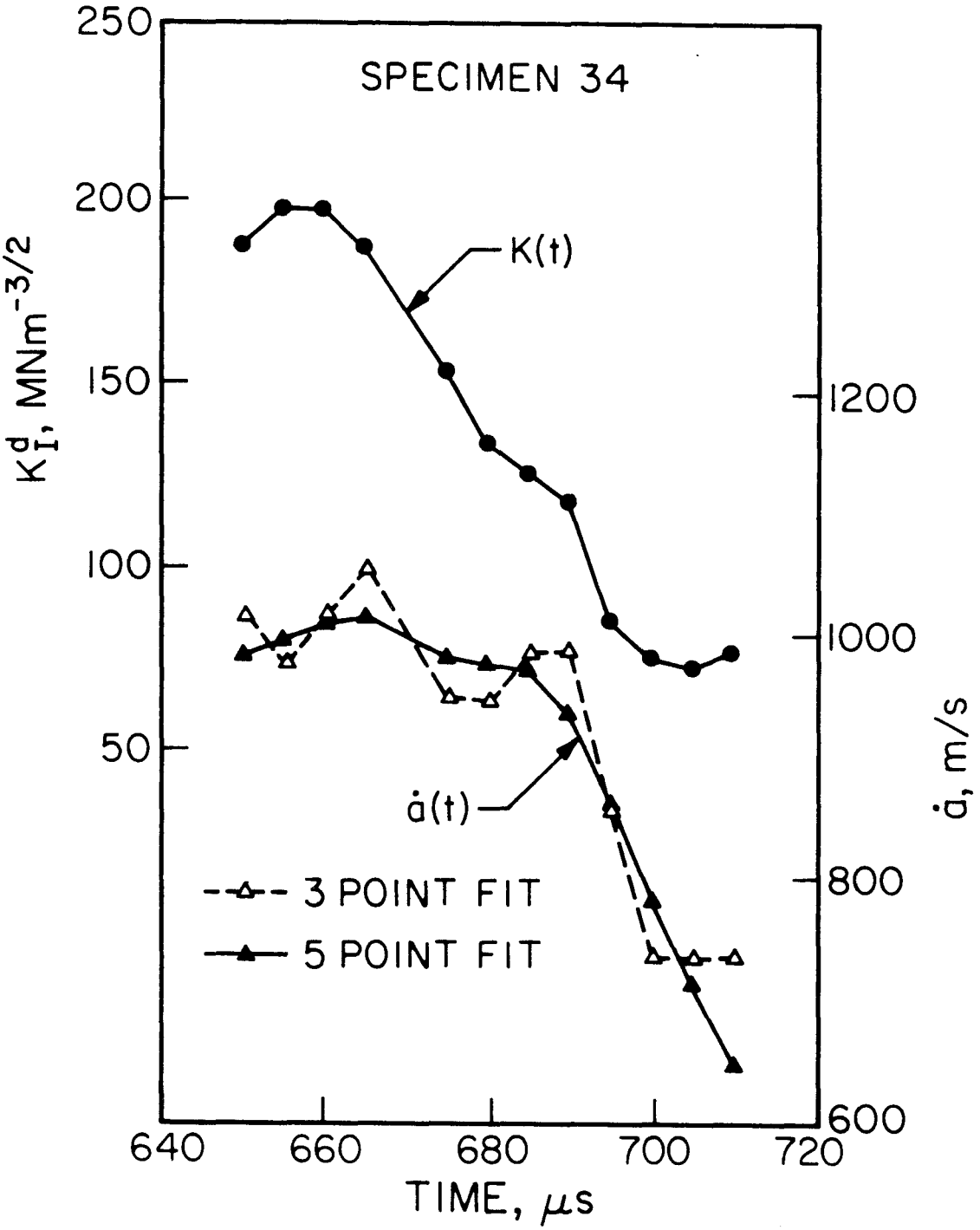

Figure 3.14 Specimen 34, stress intensity factor and crack speed records. K_I^d and $\dot{a}$ vary in phase.

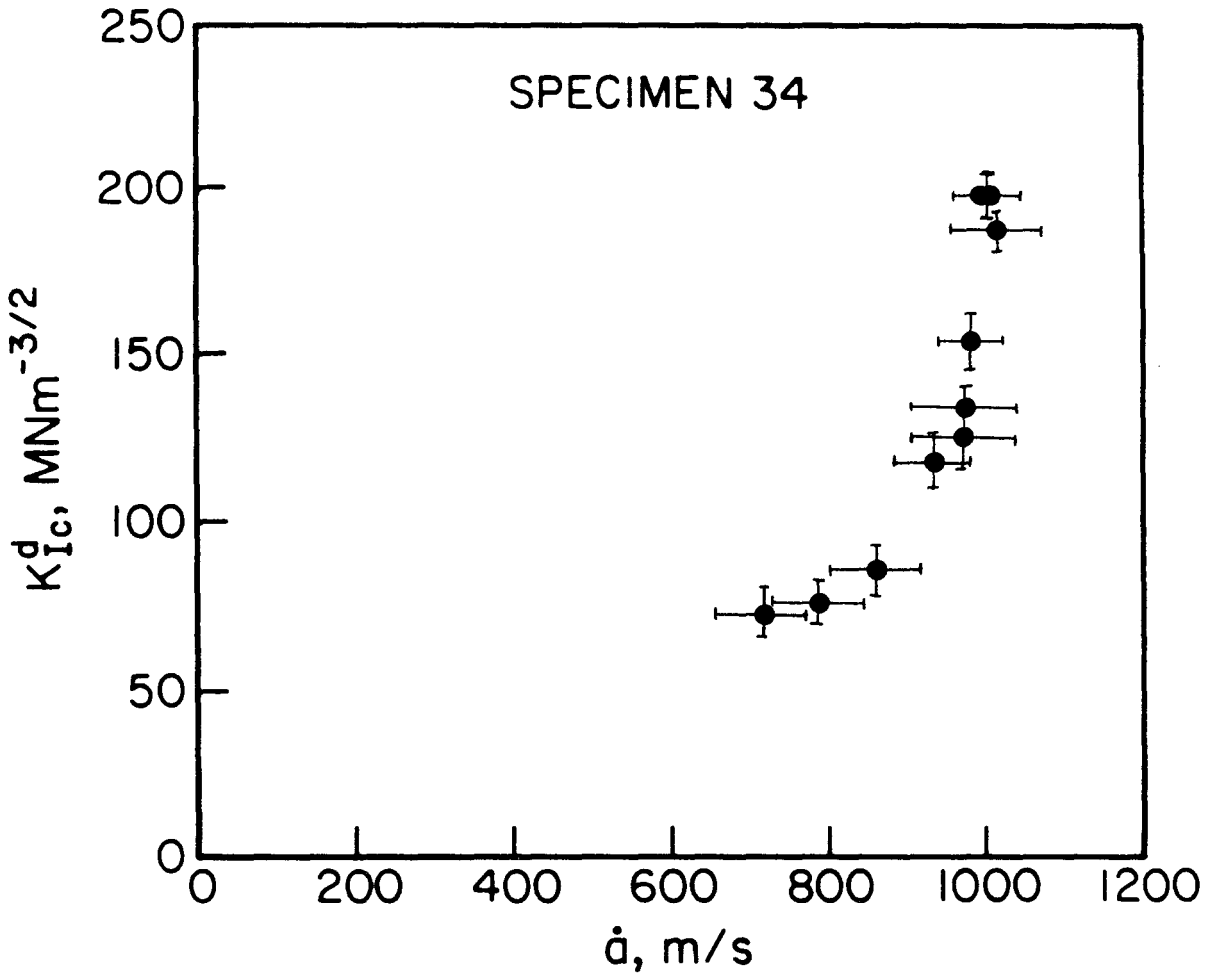

Figure 3.15 Resulting $K^d_{Ic}(\dot{a})$ relation for specimen 34.

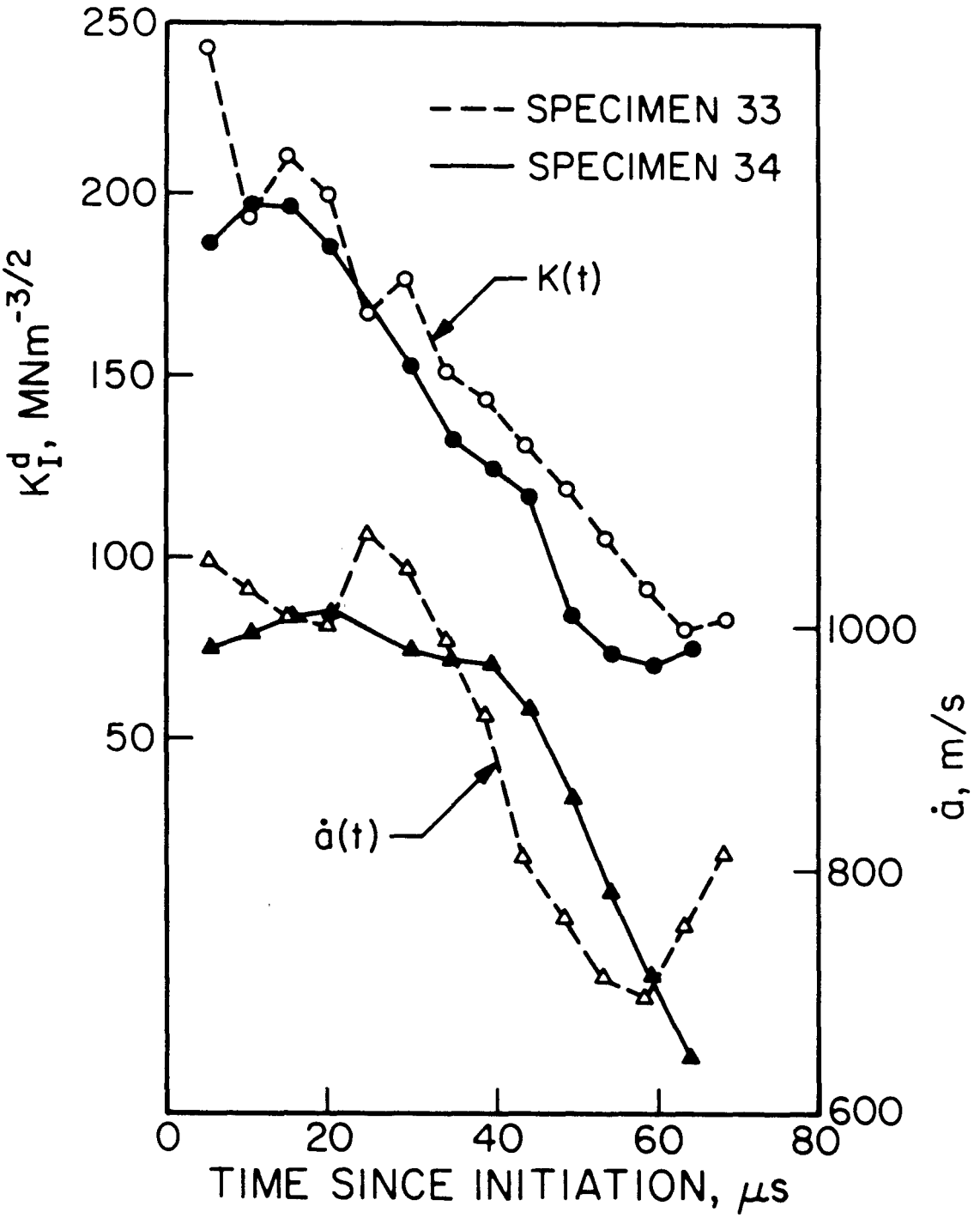

Figure 3.16 Stress intensity factor and crack speed for identical specimens. Note consistency of results.

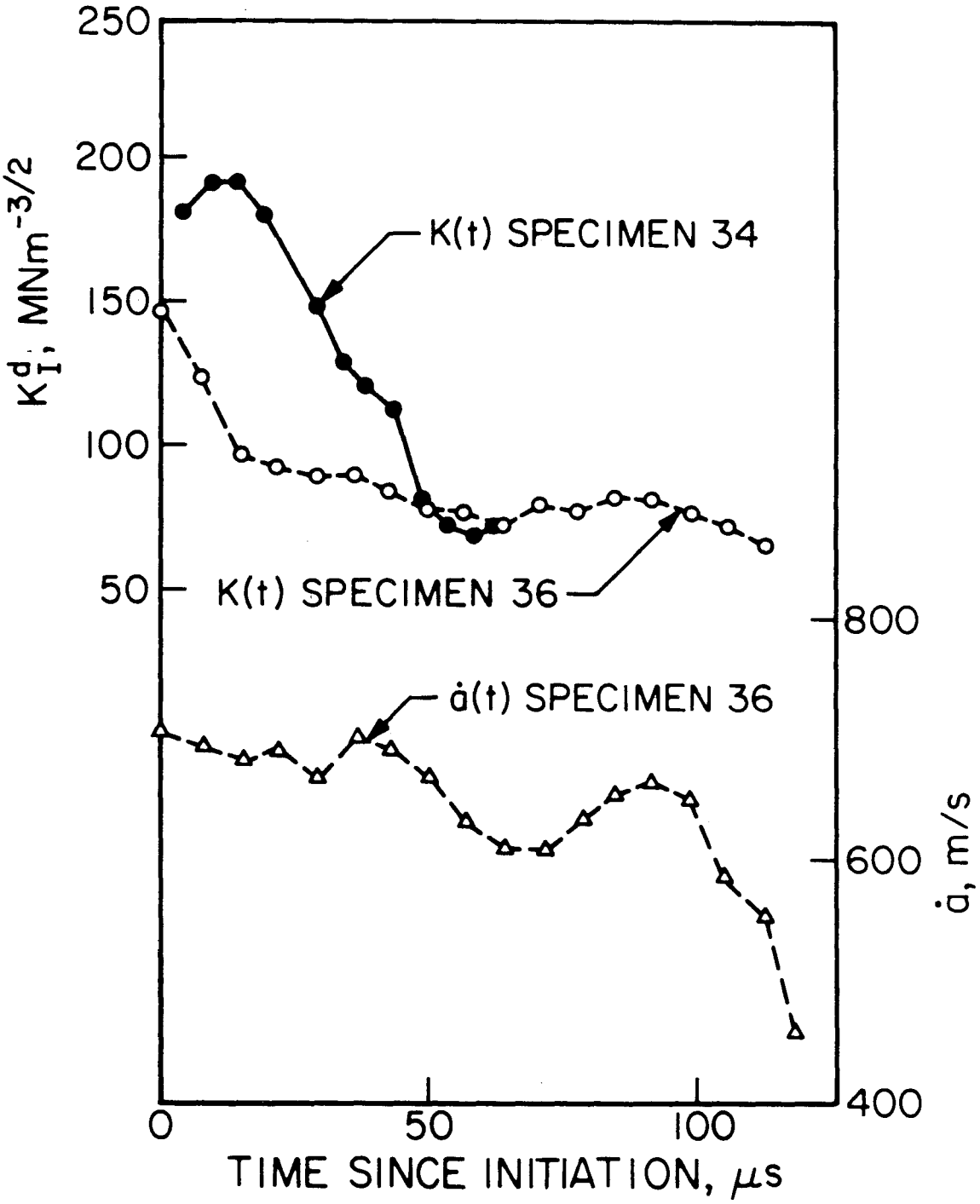

Figure 3.17 Effect of crack tip bluntness on K_I^d. Blunted specimen 34 has higher K_I^d than sharper specimen 36.

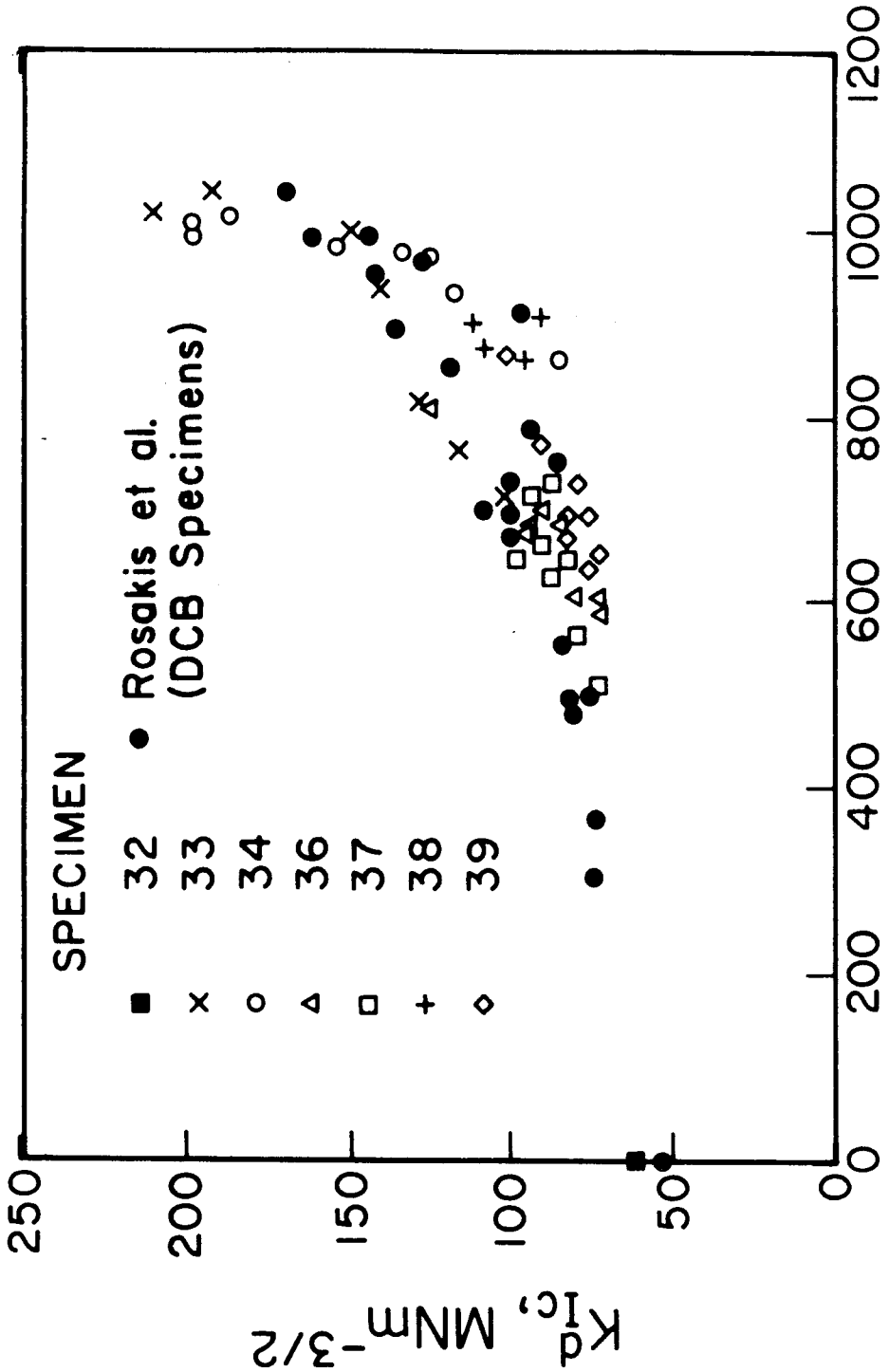

Figure 3.18 Dynamic fracture toughness K^d_{Ic} versus crack speed $\dot{a}$. Collected data from impact testing are presented with equivalent results from DCB specimens of the same material.

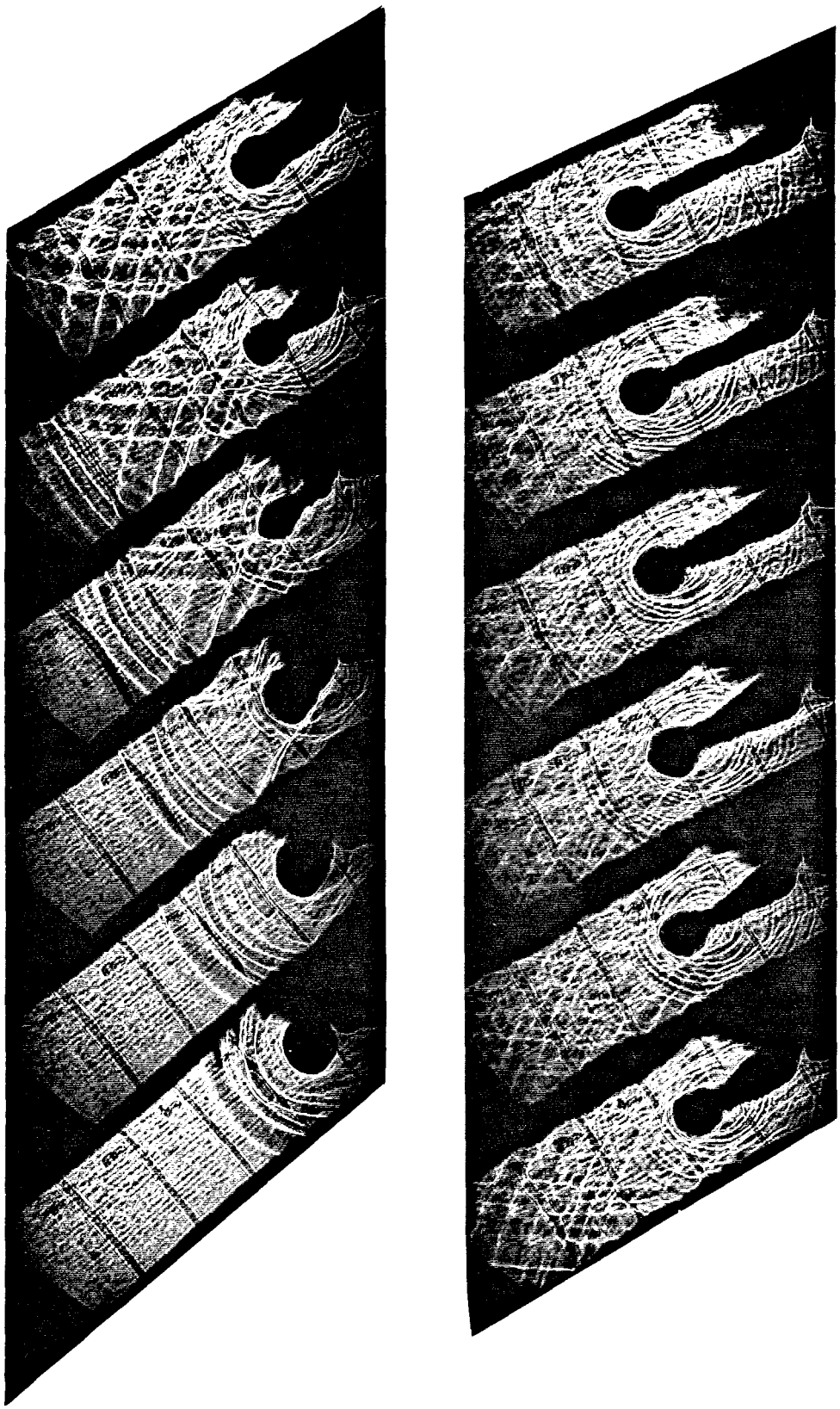

Figure 3.19 Dynamic crack growth in a DCB specimen. Strong dynamic effects are demonstrated by unloading waves emitted from crack tip and reflected from specimen boundaries.

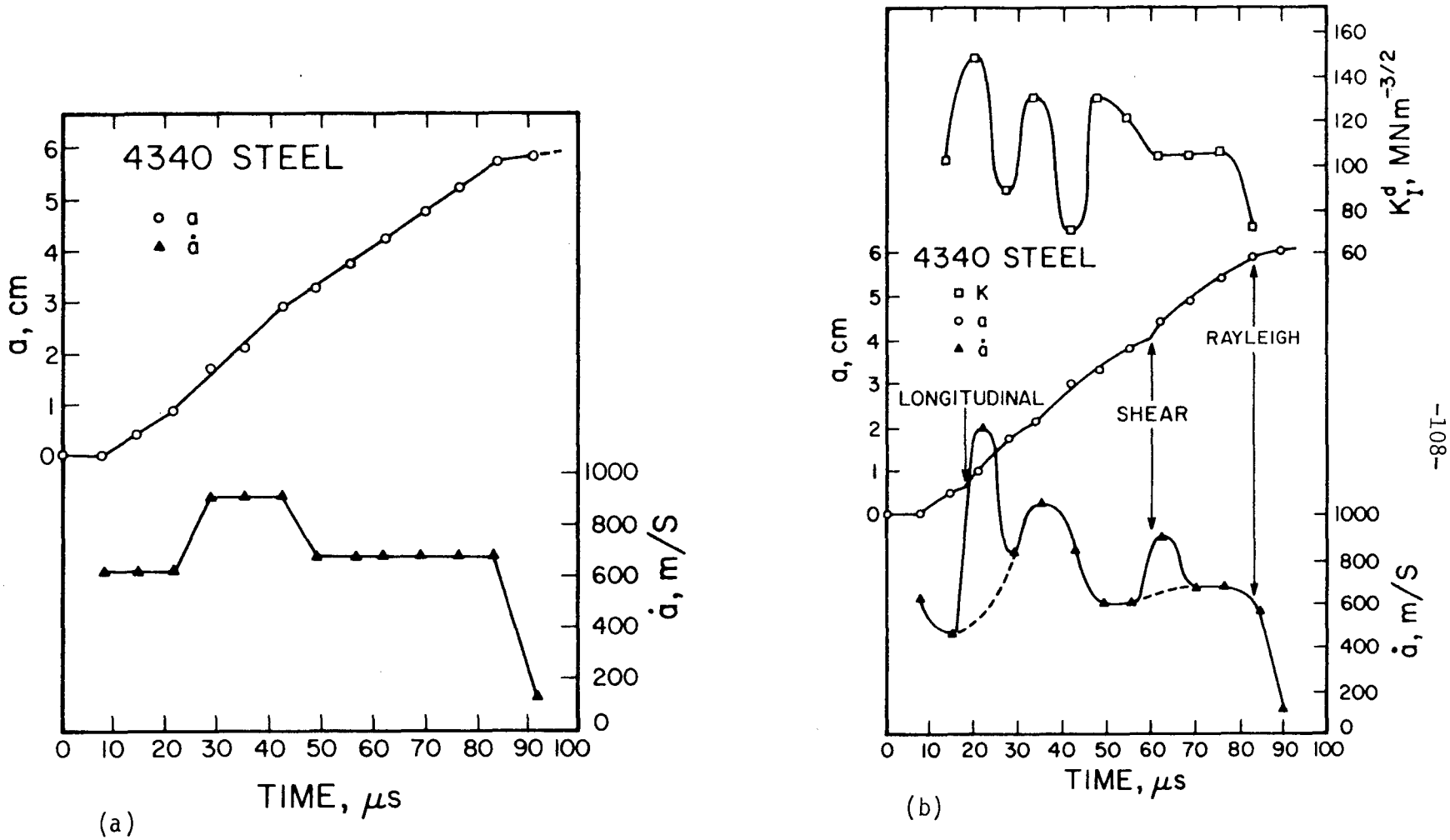

Figure 3.20 Stress intensity factor, crack length and crack speed as functions of time. (a) One interpretation of a(t) record. (b) Alternative interpretation of a(t) record. Arrows indicate reflected stress wave arrivals.

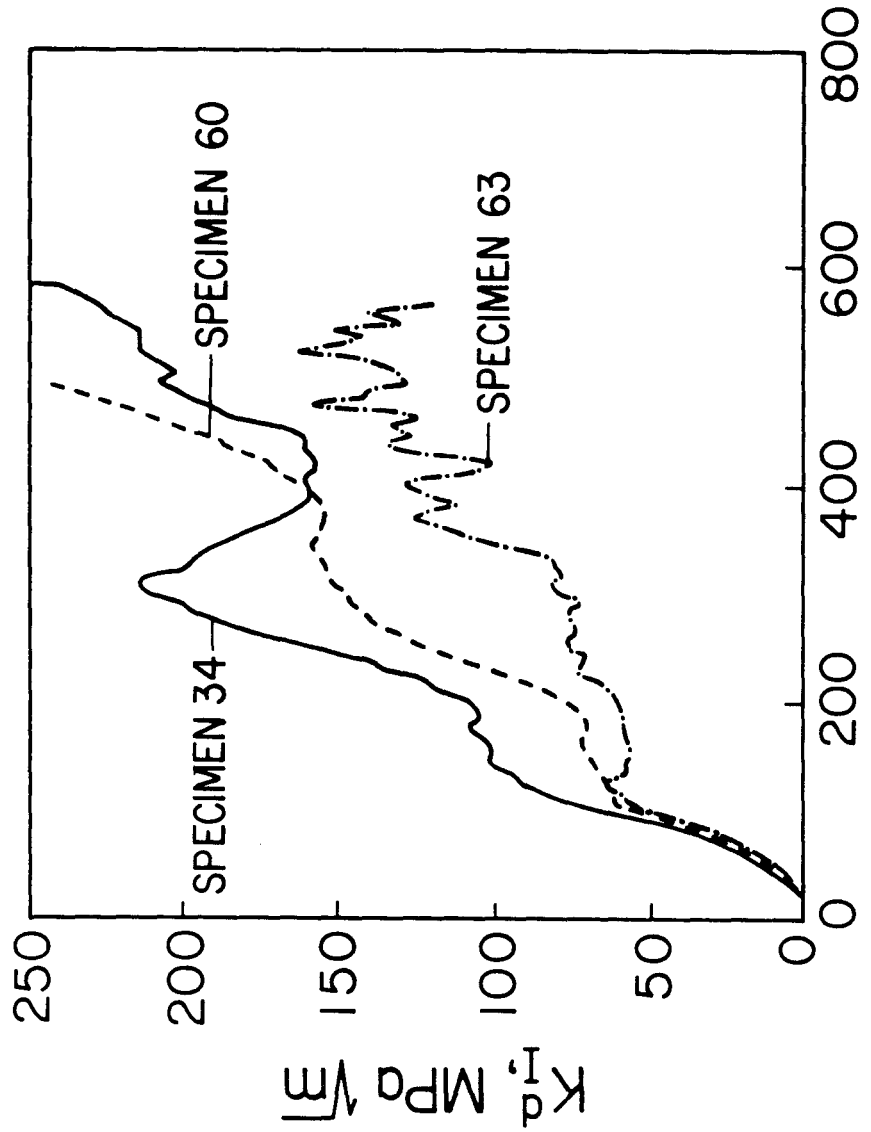

Figure 3.21 Stress intensity factor time history for three different drop weight tests.

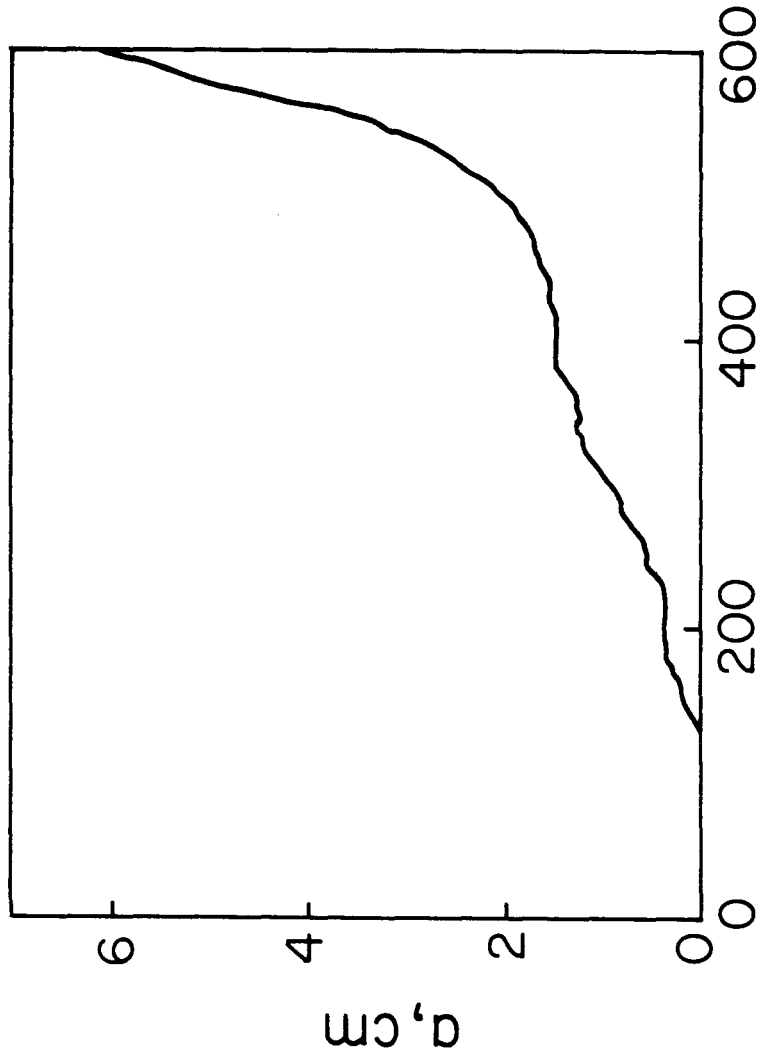

Figure 3.22 Crack length record for specimen 63.

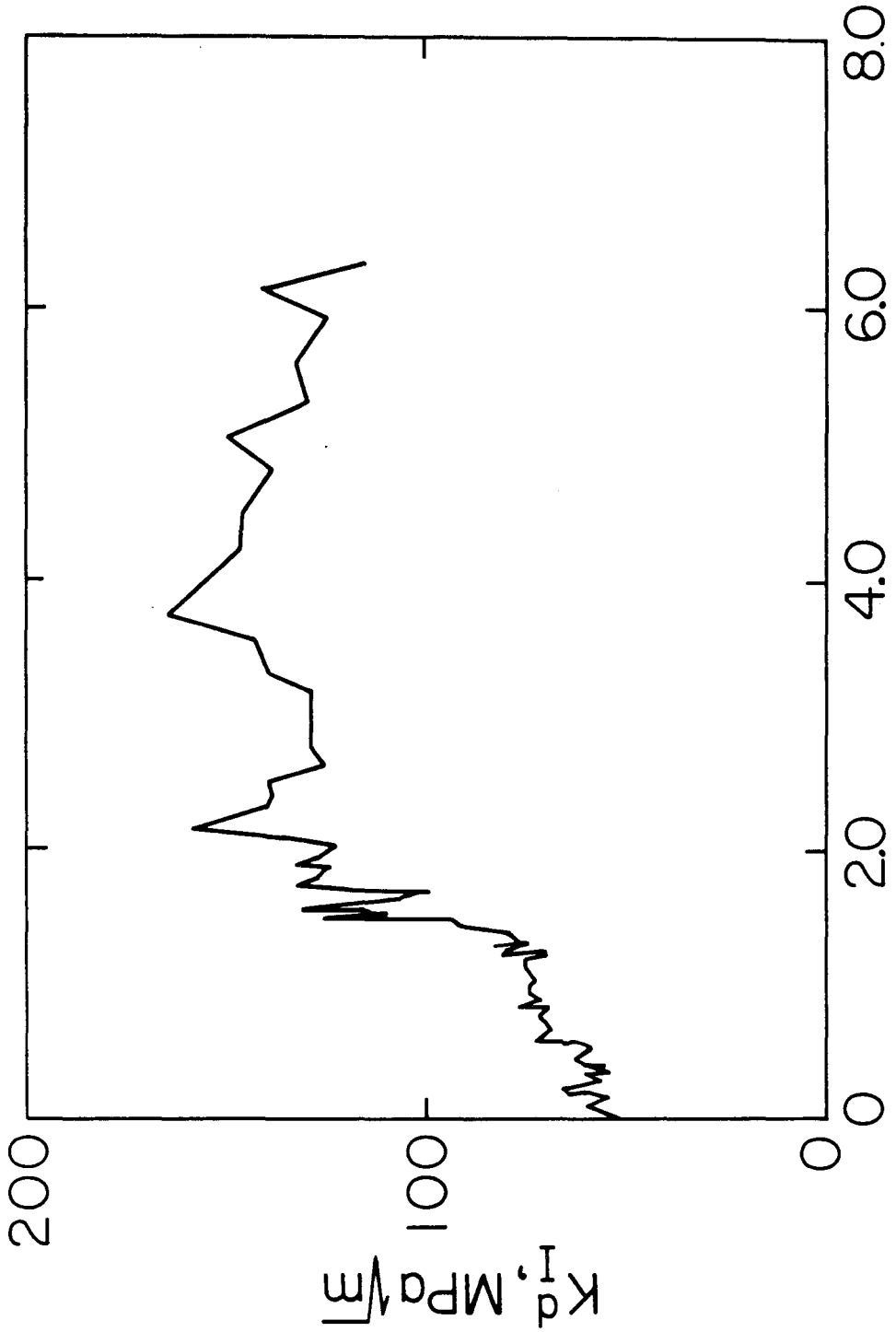

Figure 3.23 Stress intensity factor vs. crack length for specimen 63.

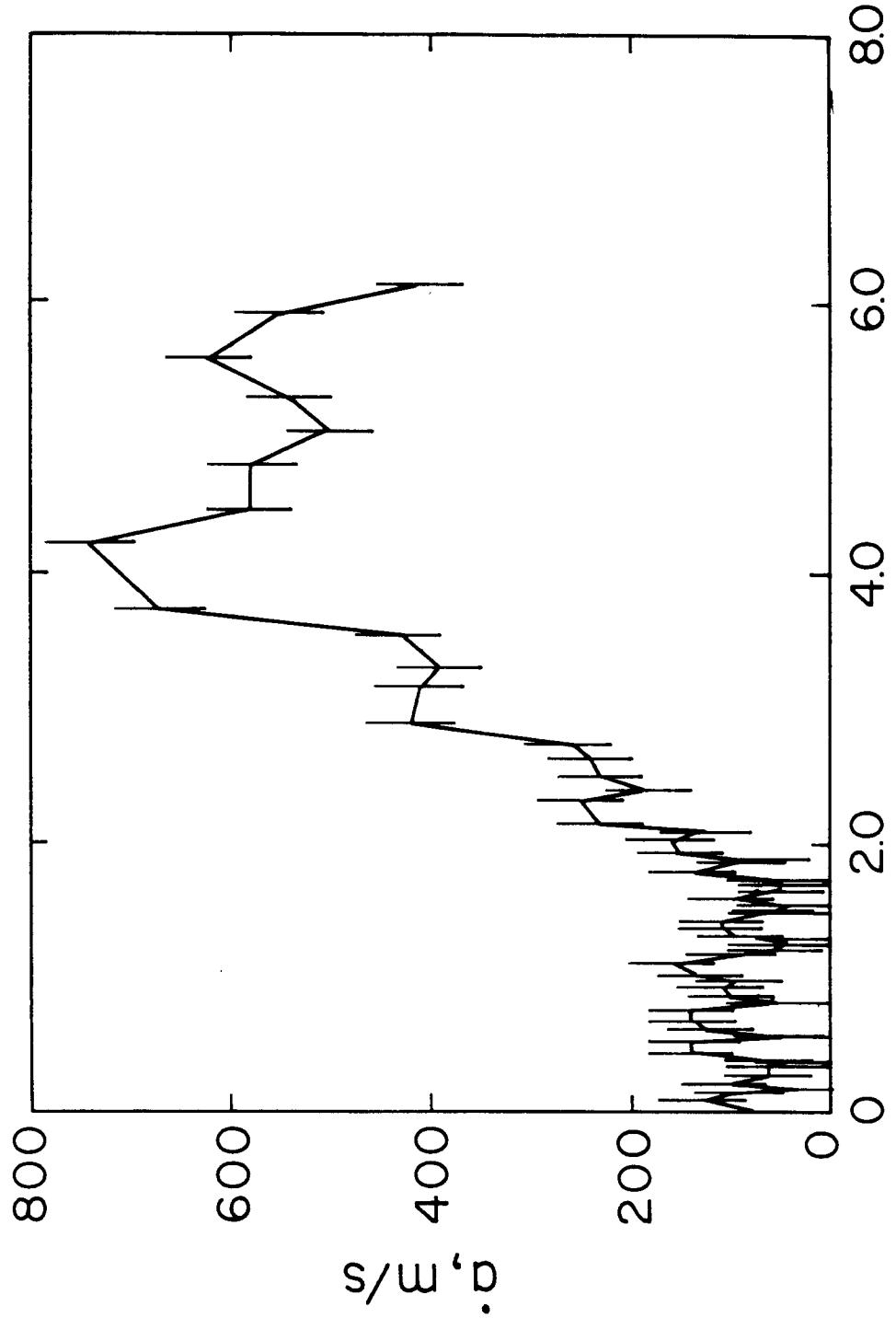

Figure 3.24 Crack tip speed vs. crack length for specimen 63.

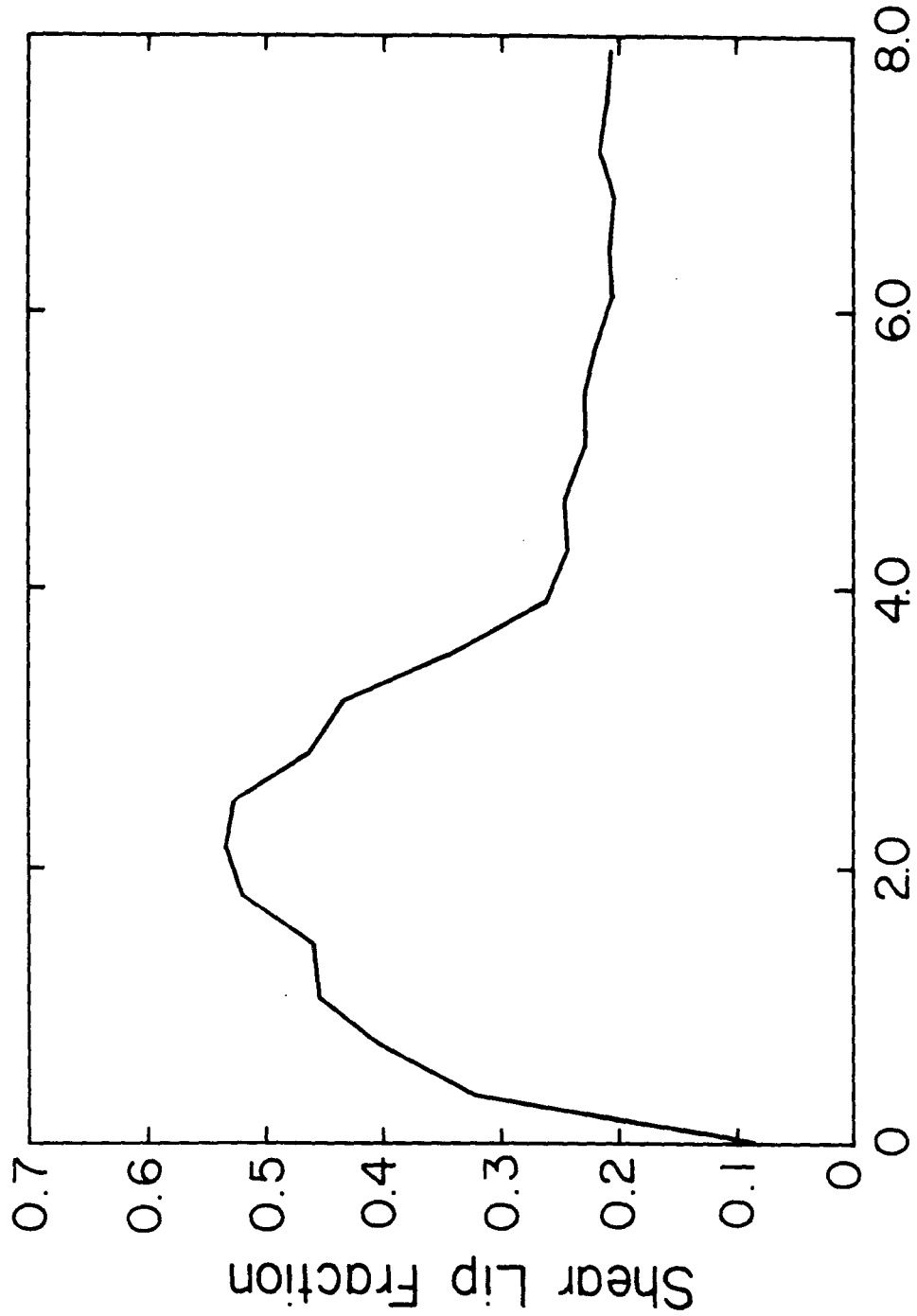

Figure 3.25 Shear lip fraction vs. crack length for specimen 63.

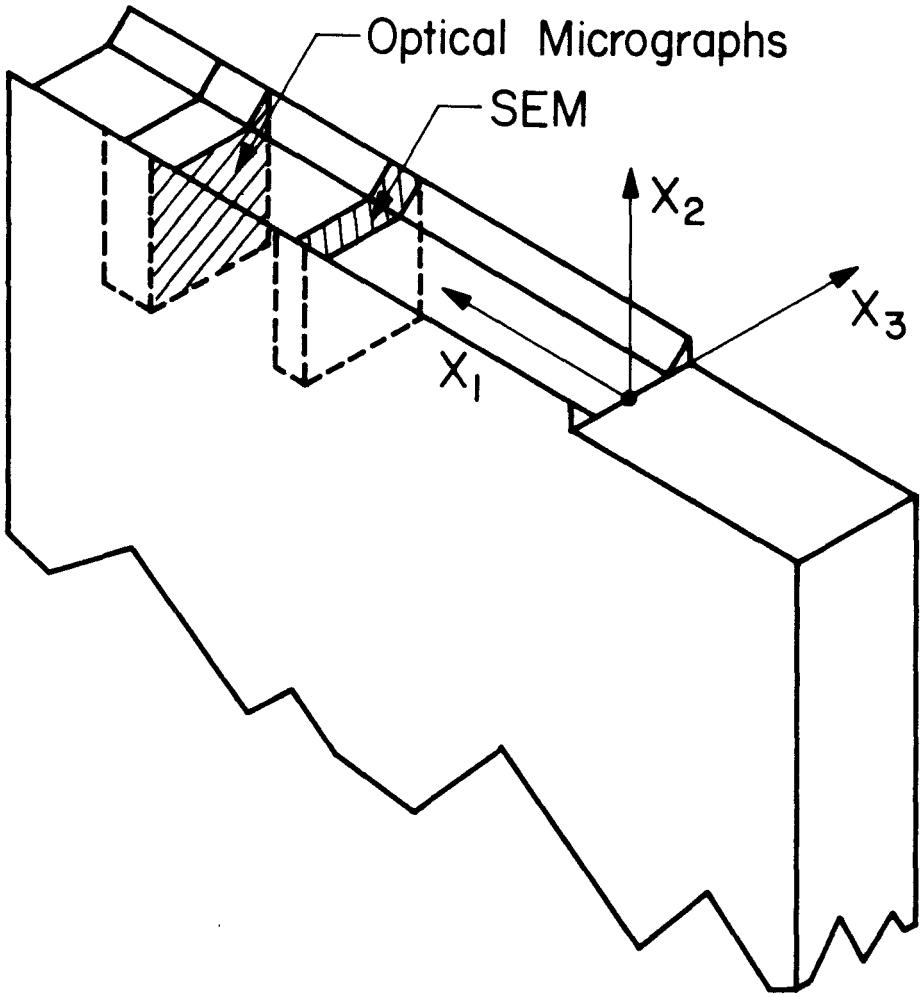

Figure 3.26 Orientation of samples for optical microscopy and SEM photographs.

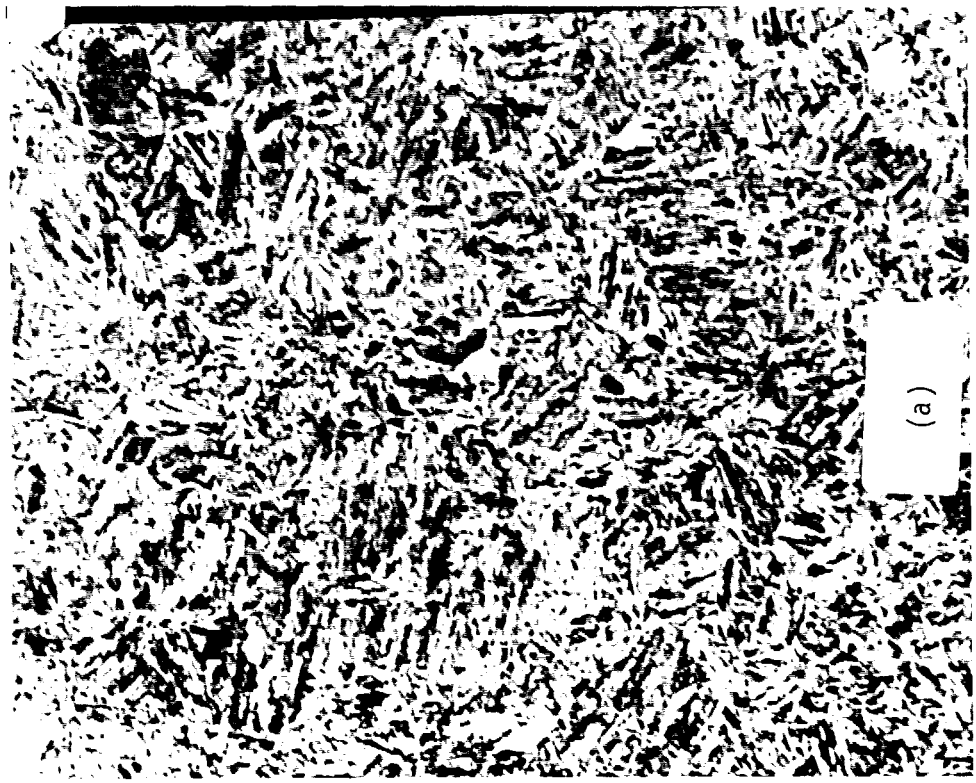

FIGURE 3.27 Microstructures of quenched and tempered 4340 steel. 1000 X. (a) Specimen 34 (b) Specimen 63.

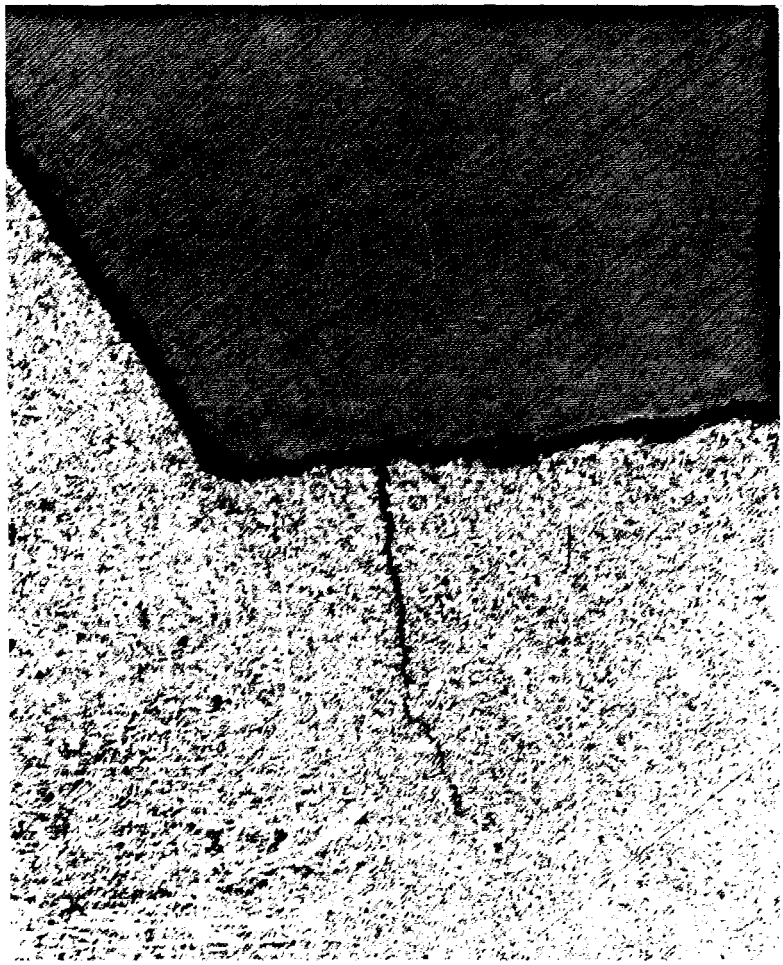

Figure 3.28 Crack perpendicular to the thickness direction. 200X.

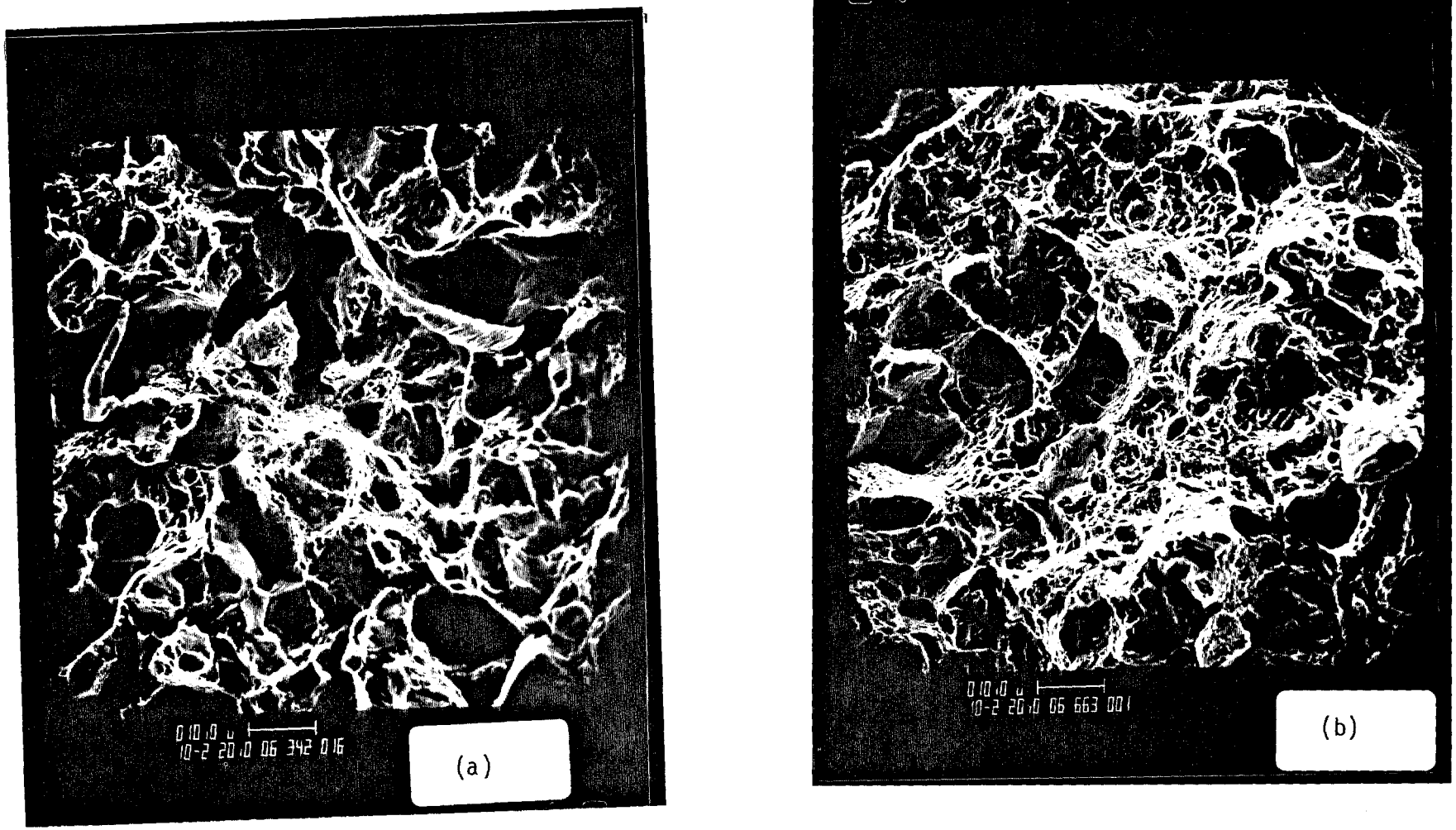

FIGURE 3.29 SEM photographs of the fracture surface. 1000 X.
Crack propagation speed approx. 600 m/s.
(a) Specimen 34 (b) Specimen 63.

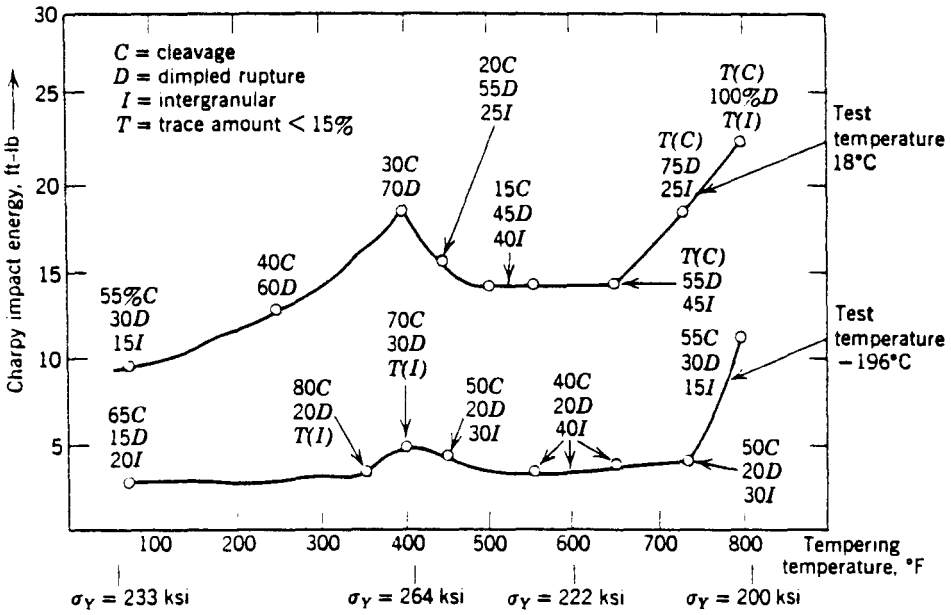

Figure 3.30 Estimated percentage of fracture modes, 4340 steel. (From Tetelman and McEvily [55].)

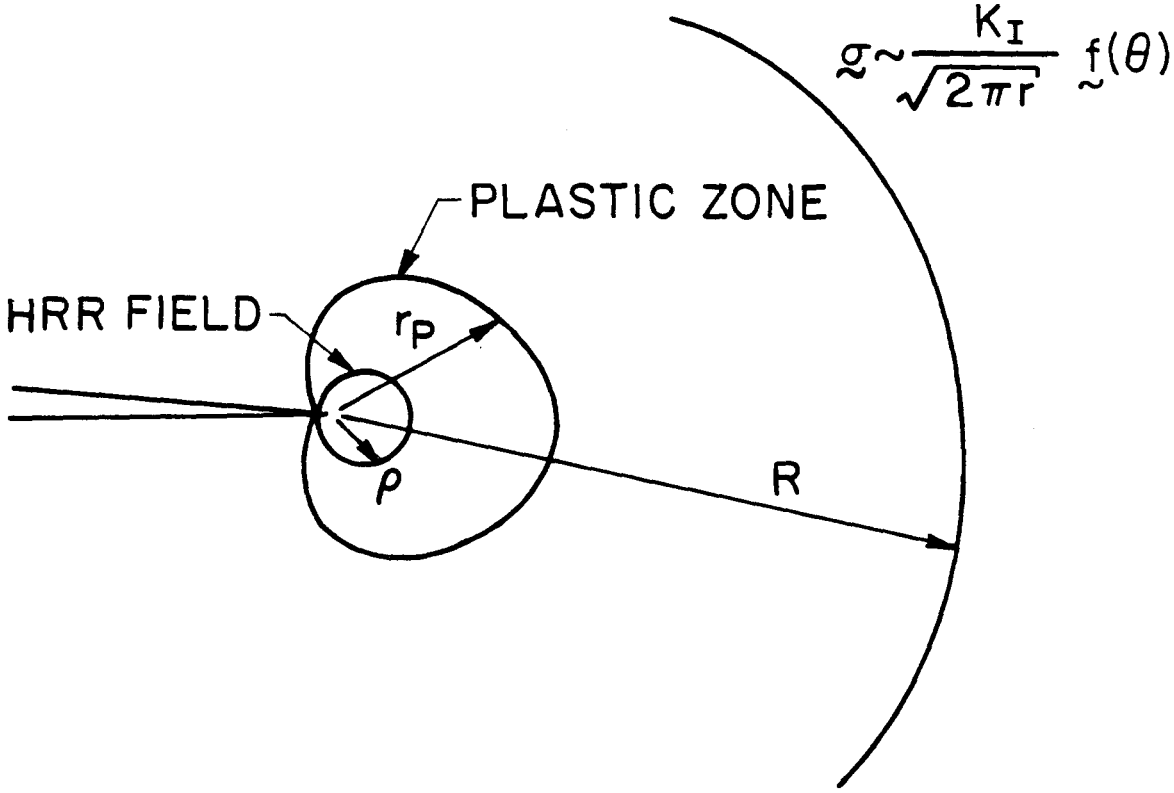

Figure 4.1 Small scale yielding idealization. Plastic zone lies within K dominated zone. HRR dominated field lies within plastic zone.

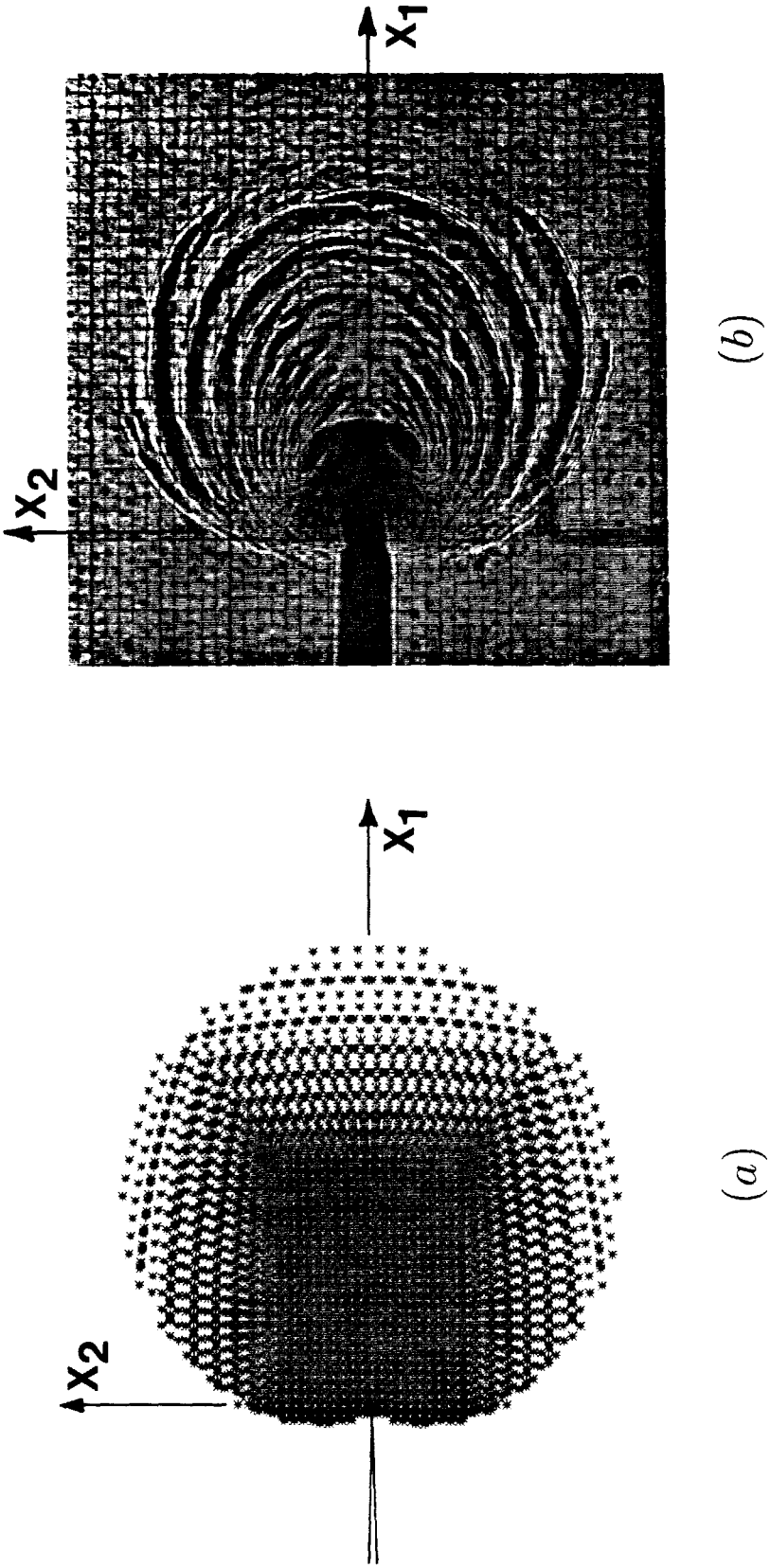

Figure 4.2 Plane stress plastic zone for n=9. (a) Numerical (b) Experimental.

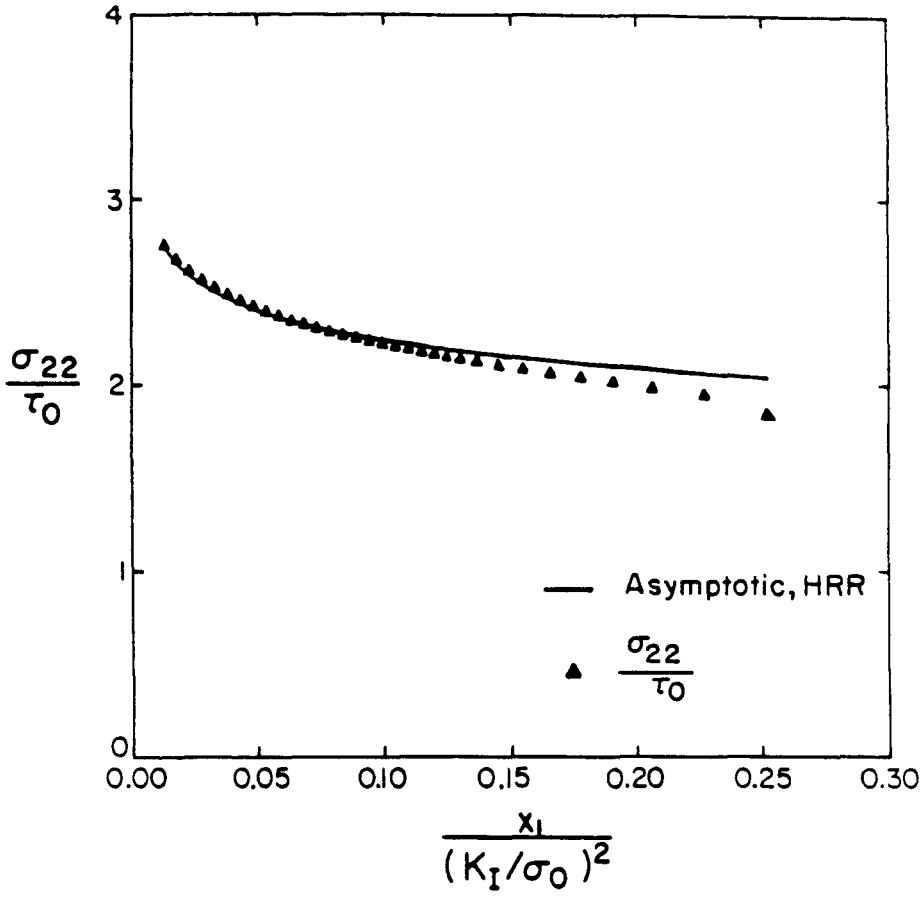

Figure 4.3 Normal stress distribution ahead of the crack tip. τ_0 is the yield stress in shear.

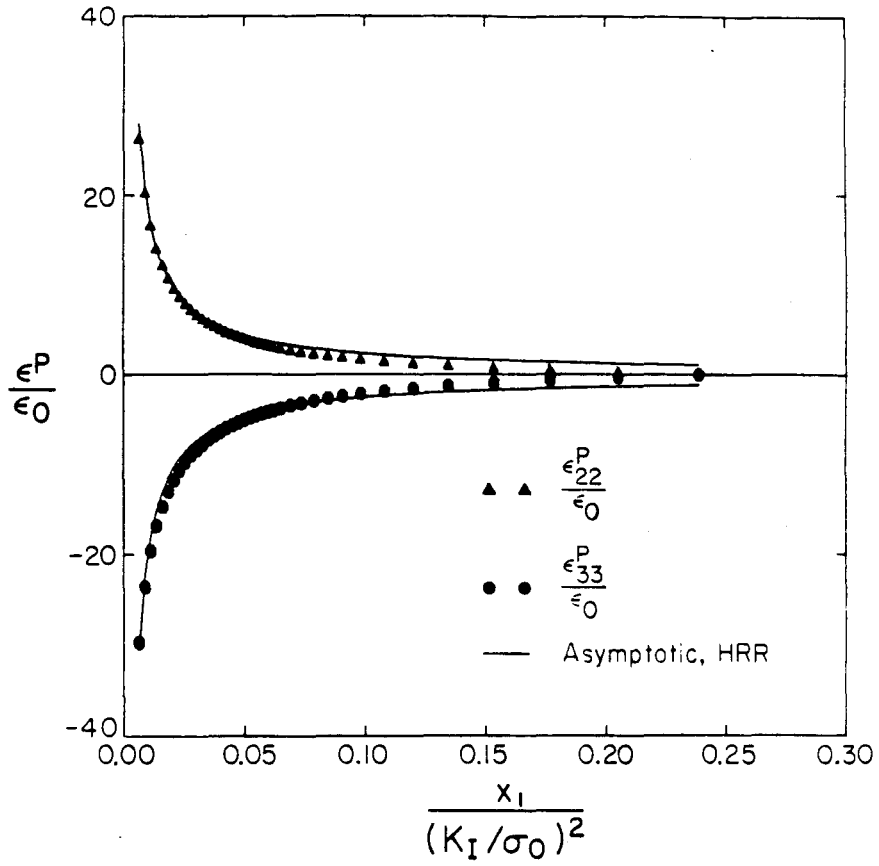

Figure 4.4 Plastic strain distribution ahead of the crack tip.

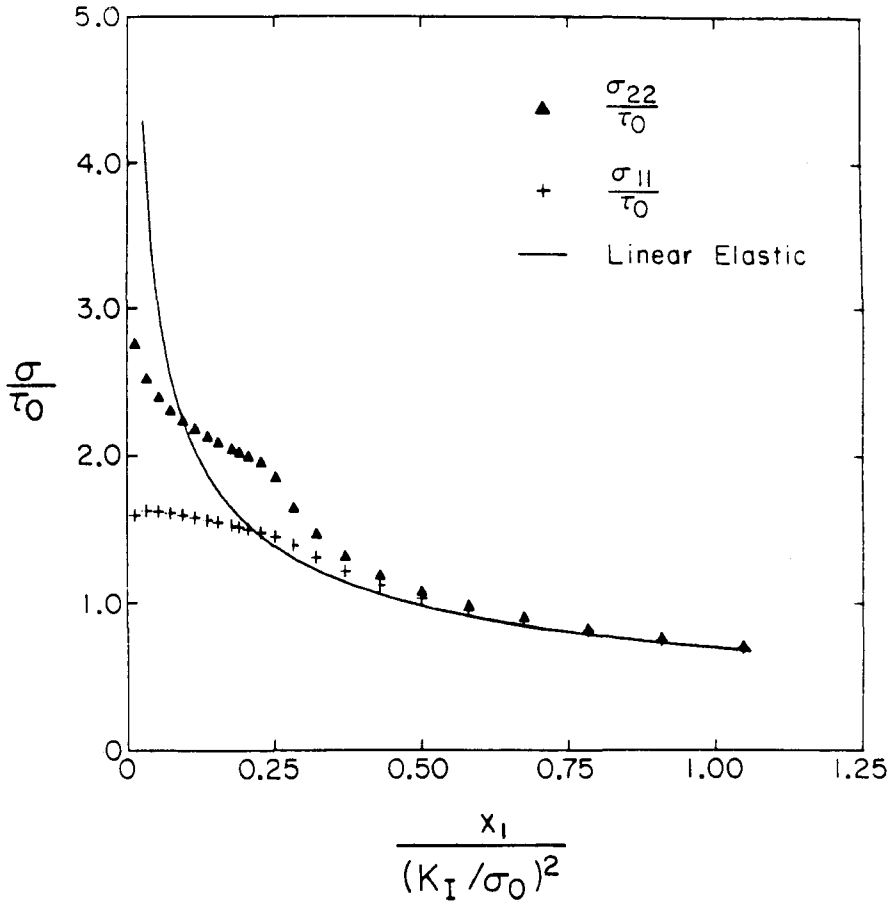

Figure 4.5 Normal stress distribution ahead of the crack tip compared to stresses from the linear elastic K_I field.

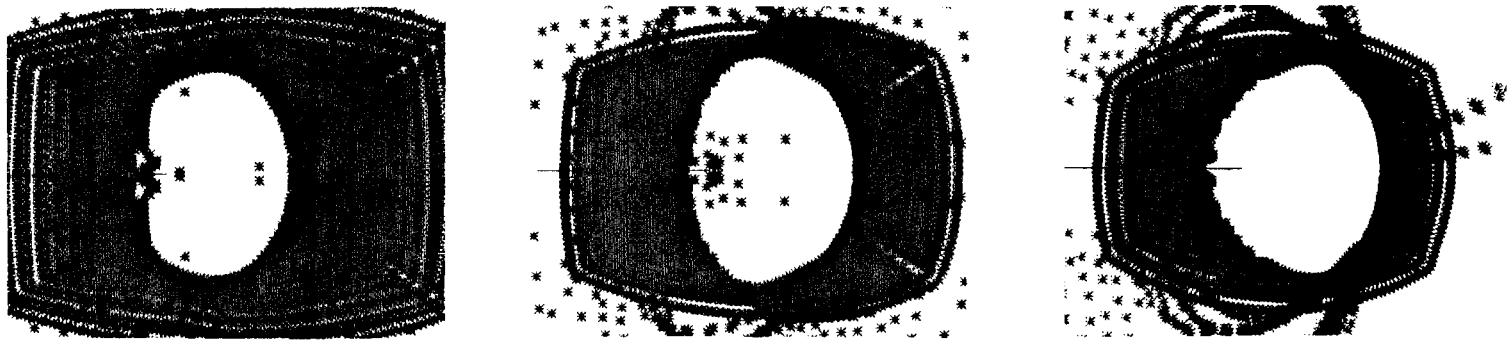

a) $\frac{r_0}{r_p} \approx 0.19$ b) $\frac{r_0}{r_p} \approx 0.30$ c) $\frac{r_0}{r_p} \approx 0.40$

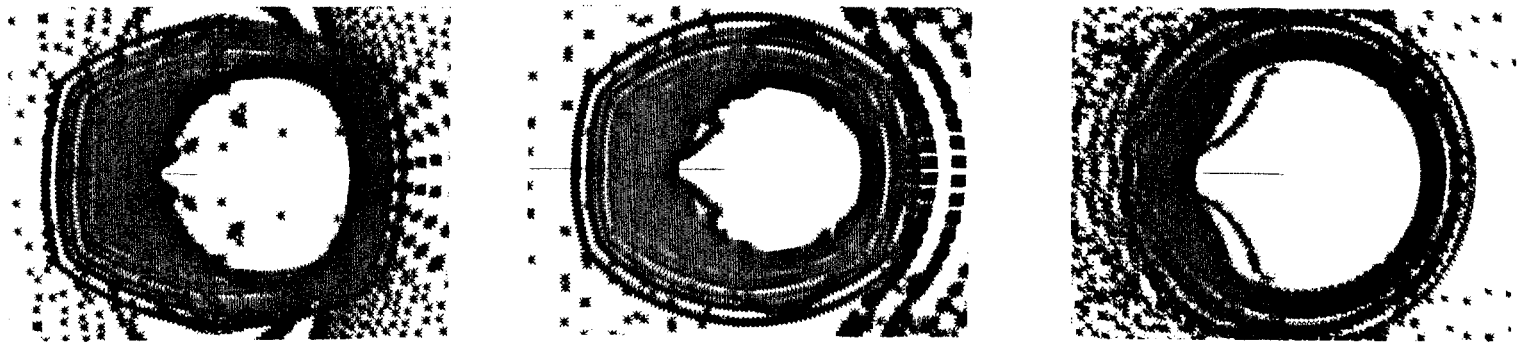

d) $\frac{r_0}{r_p} \approx 0.42$ e) $\frac{r_0}{r_p} \approx 0.51$ f) $\frac{r_0}{r_p} \approx 1.3$

Figure 4.6 Caustics generated by using the out of plane displacements calculated from the numerical model.

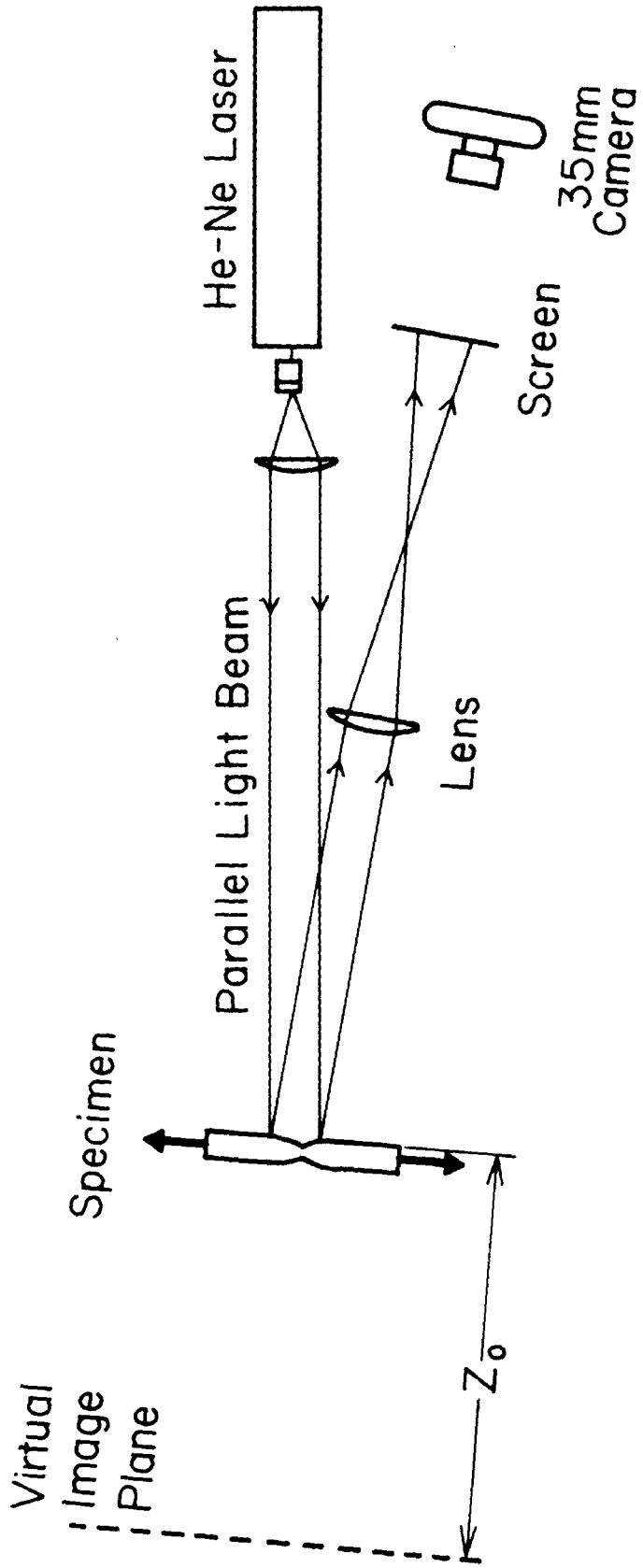

Figure 4.7 Experimental setup for photographing reflected caustics.

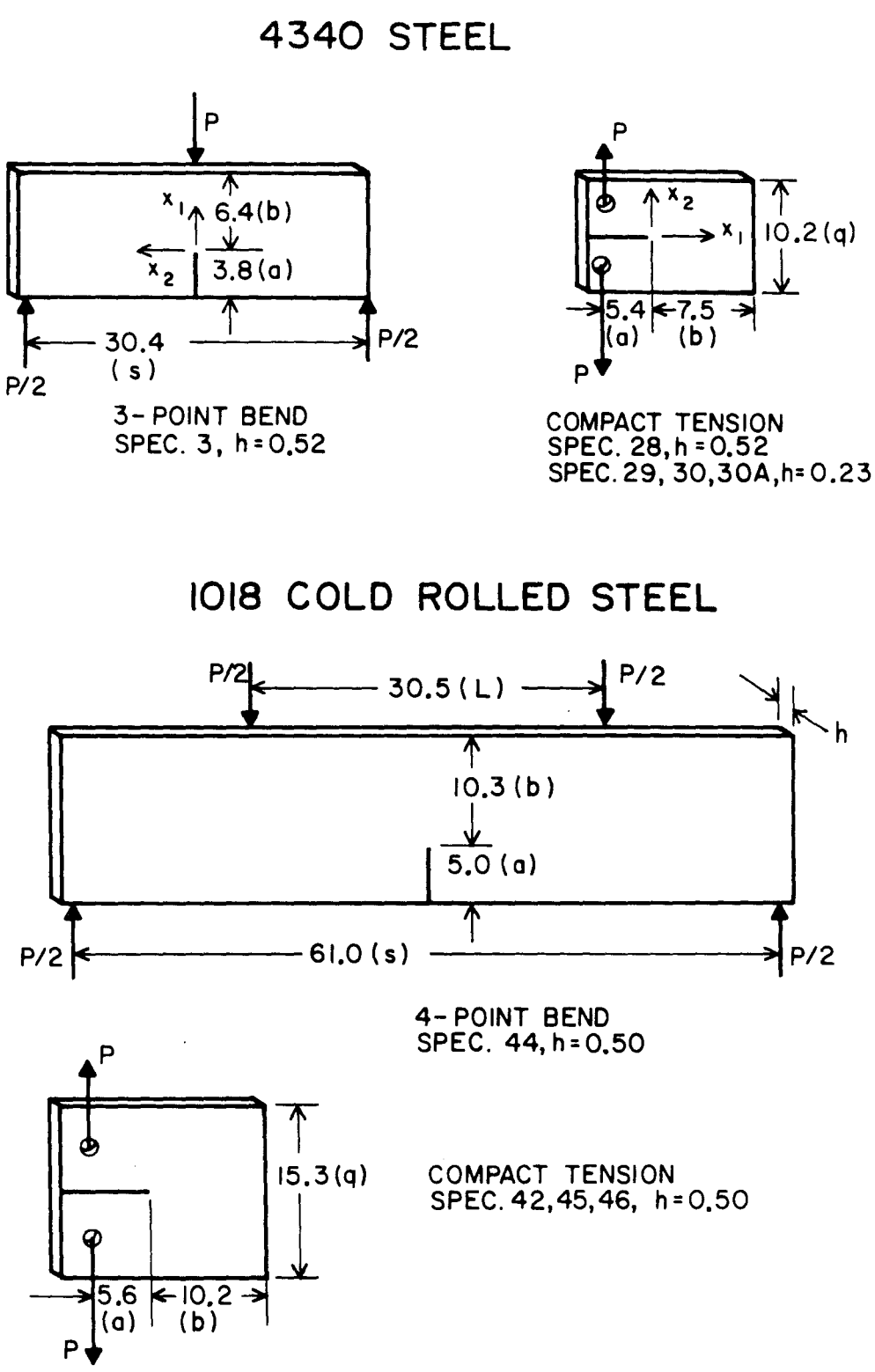

Figure 4.8 Specimen dimensions and geometries. All dimensions in cm.

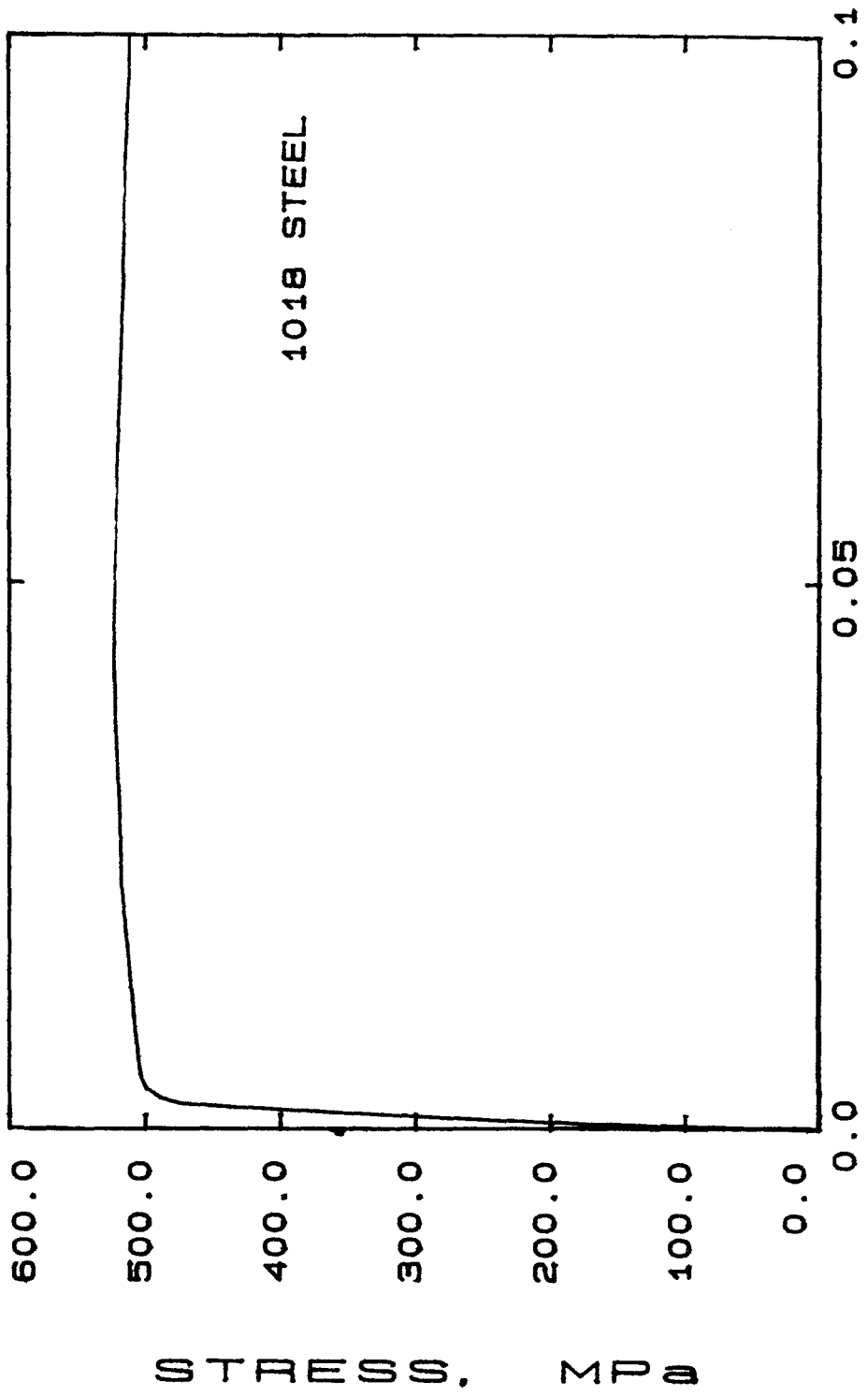

Figure 4.9 Uniaxial stress-strain relation for 1018 cold-rolled steel.

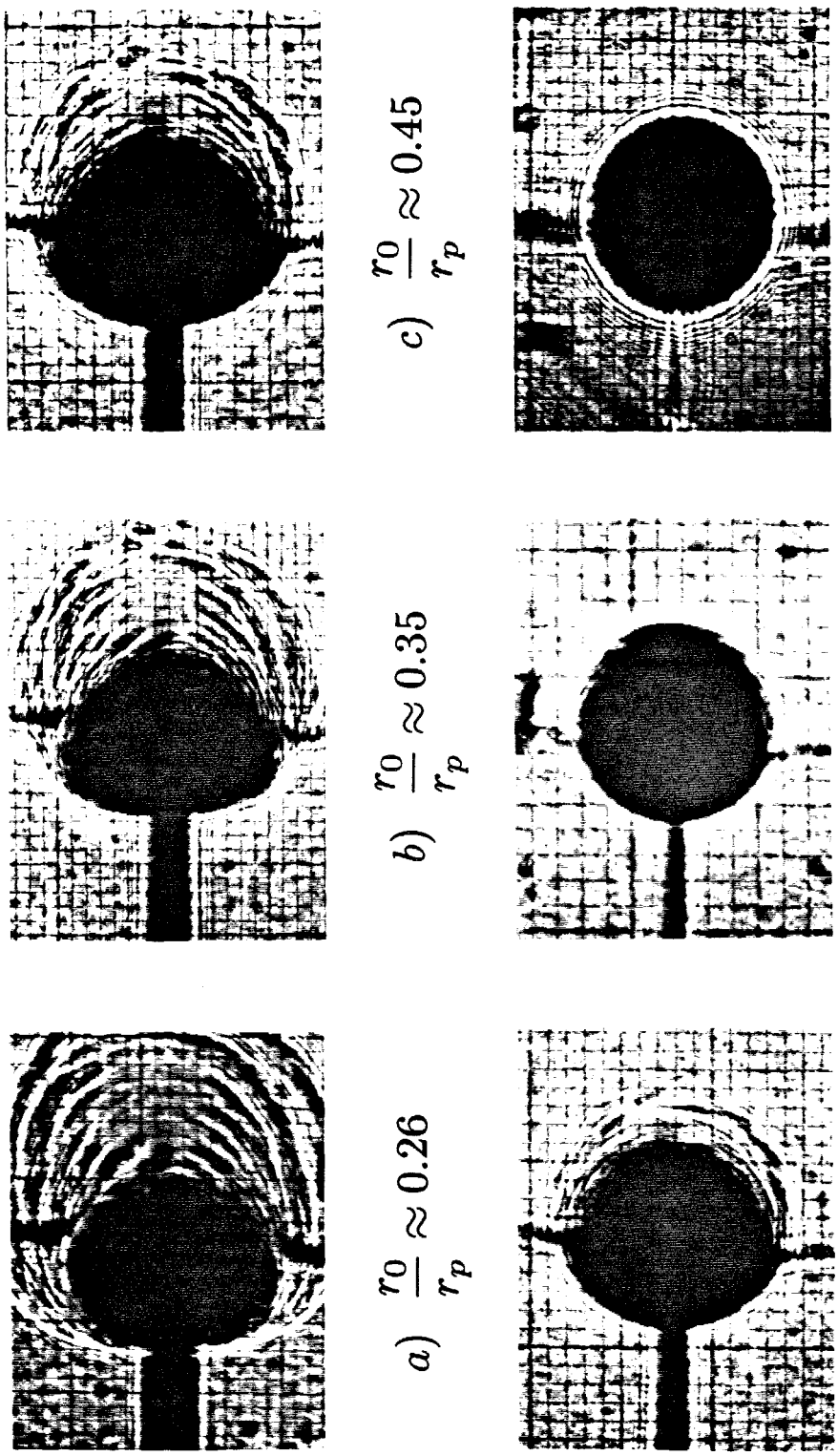

Figure 4.10 Sequence of caustics obtained for reflection of light from regions near a plastically deforming crack tip.

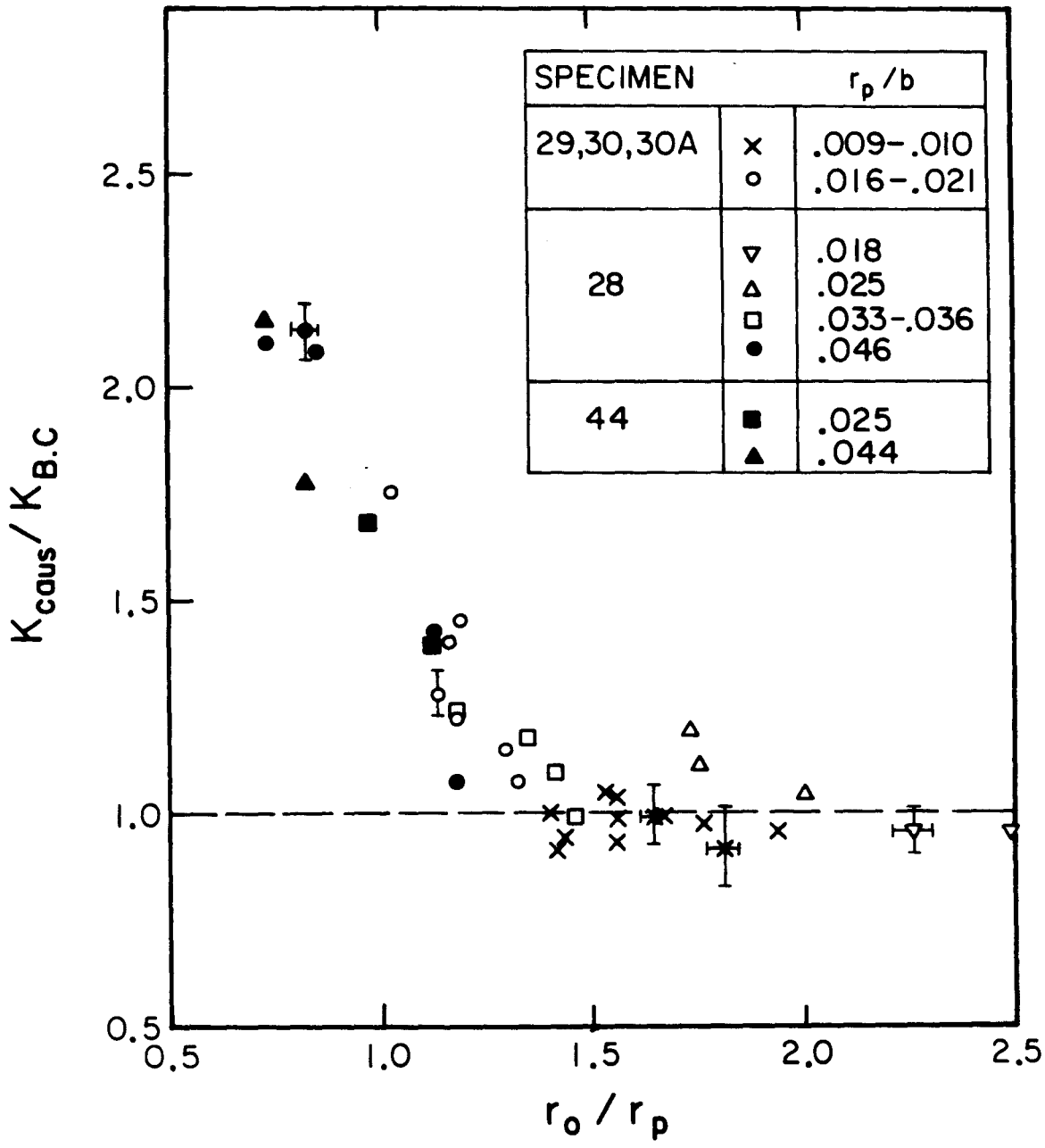

Figure 4.11 $\frac{K_{caus}}{K_{B.C.}}$ vs. $\frac{r_0}{r_p}$. Deviation from 1.0 indicates error caused by plasticity.

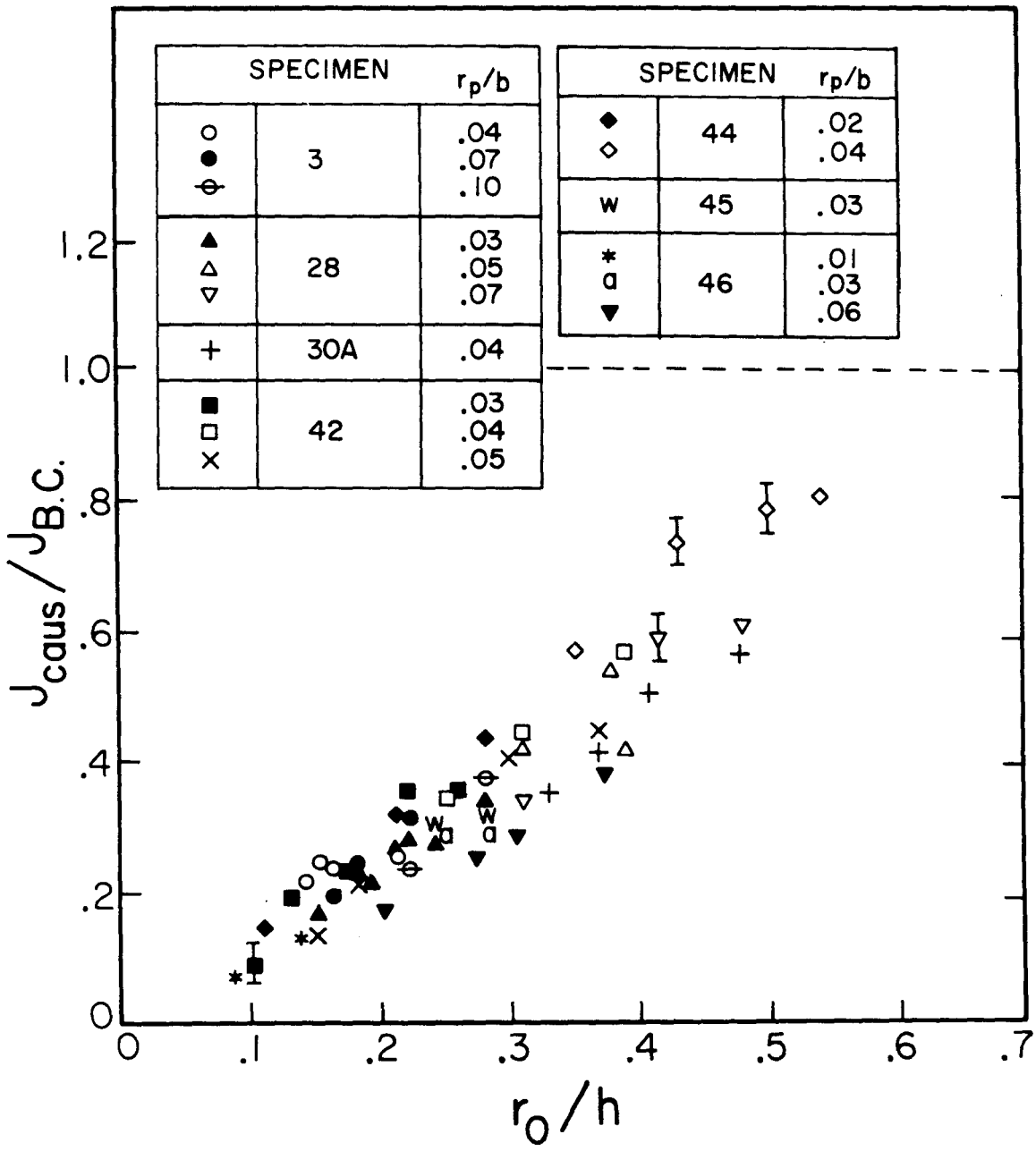

Figure 4.12 $\frac{J_{caus}}{J_{BC}}$ vs. $\frac{r_0}{h}$. Deviation from 1.0 indicates error due to three dimensionality for $\frac{r_0}{h} < 0.6$.

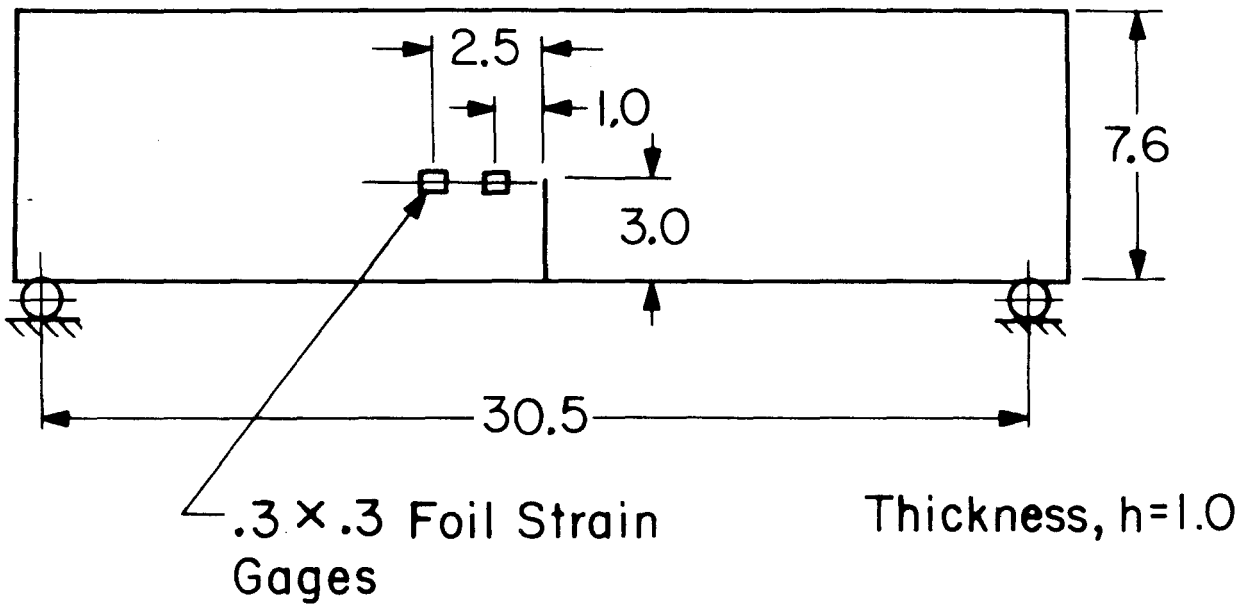

Figure 5.1 Specimen dimensions and geometry for specimens 67-71. All dimensions are in cm.

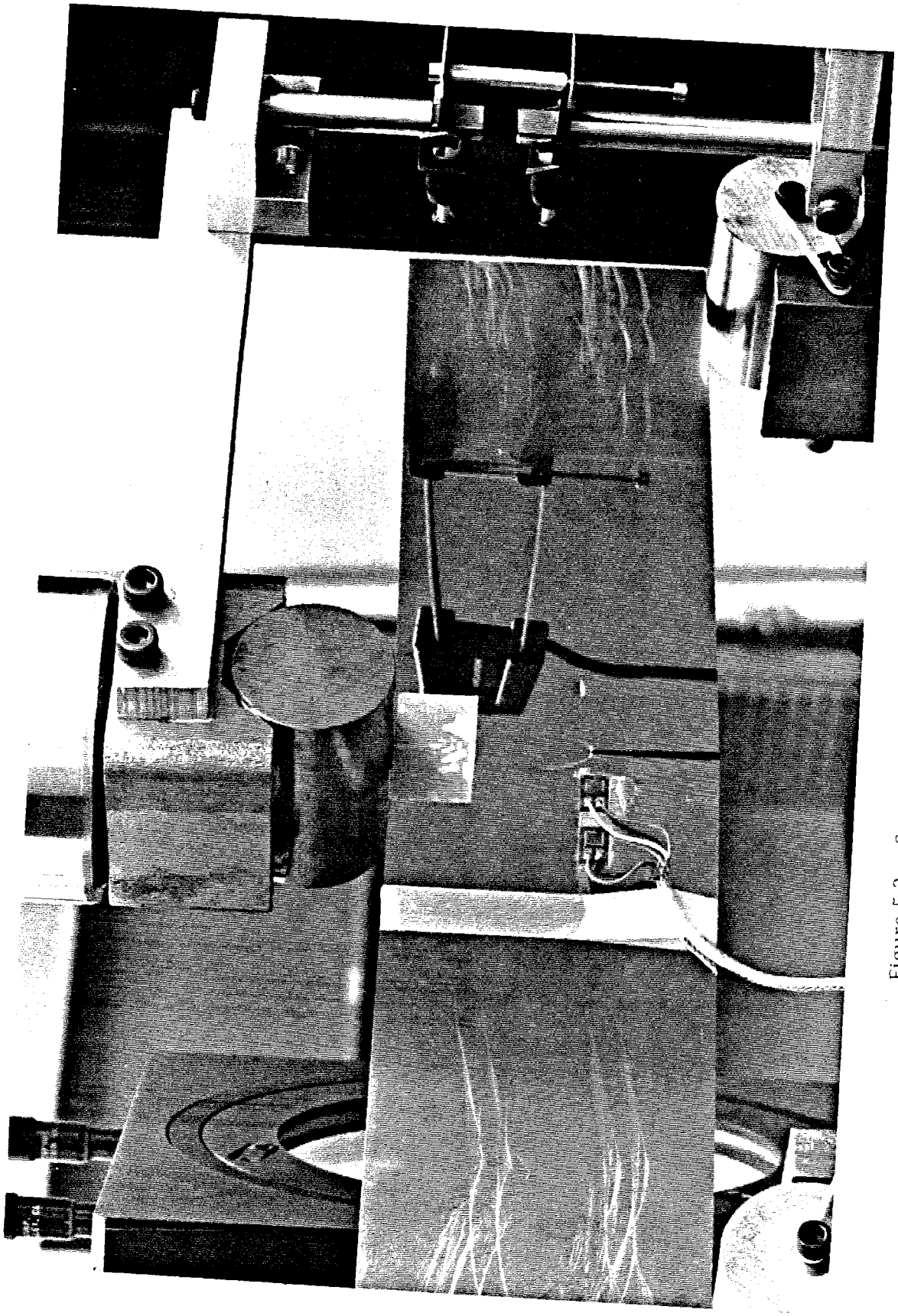

Figure 5.2 Specimen, loading fixtures, strain gages and extensometer.

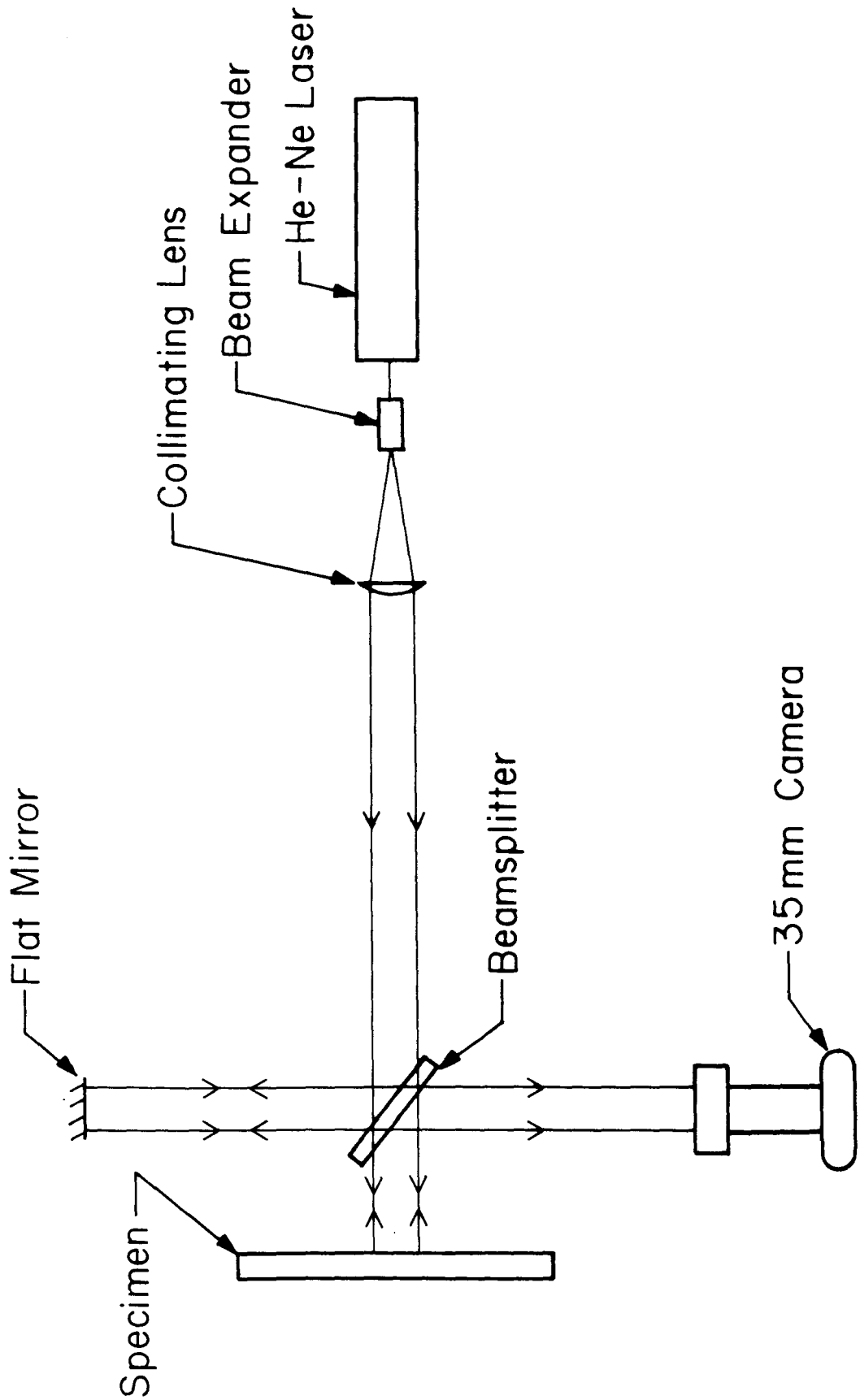

Figure 5.3 Diagram of optical setup for interferometry.

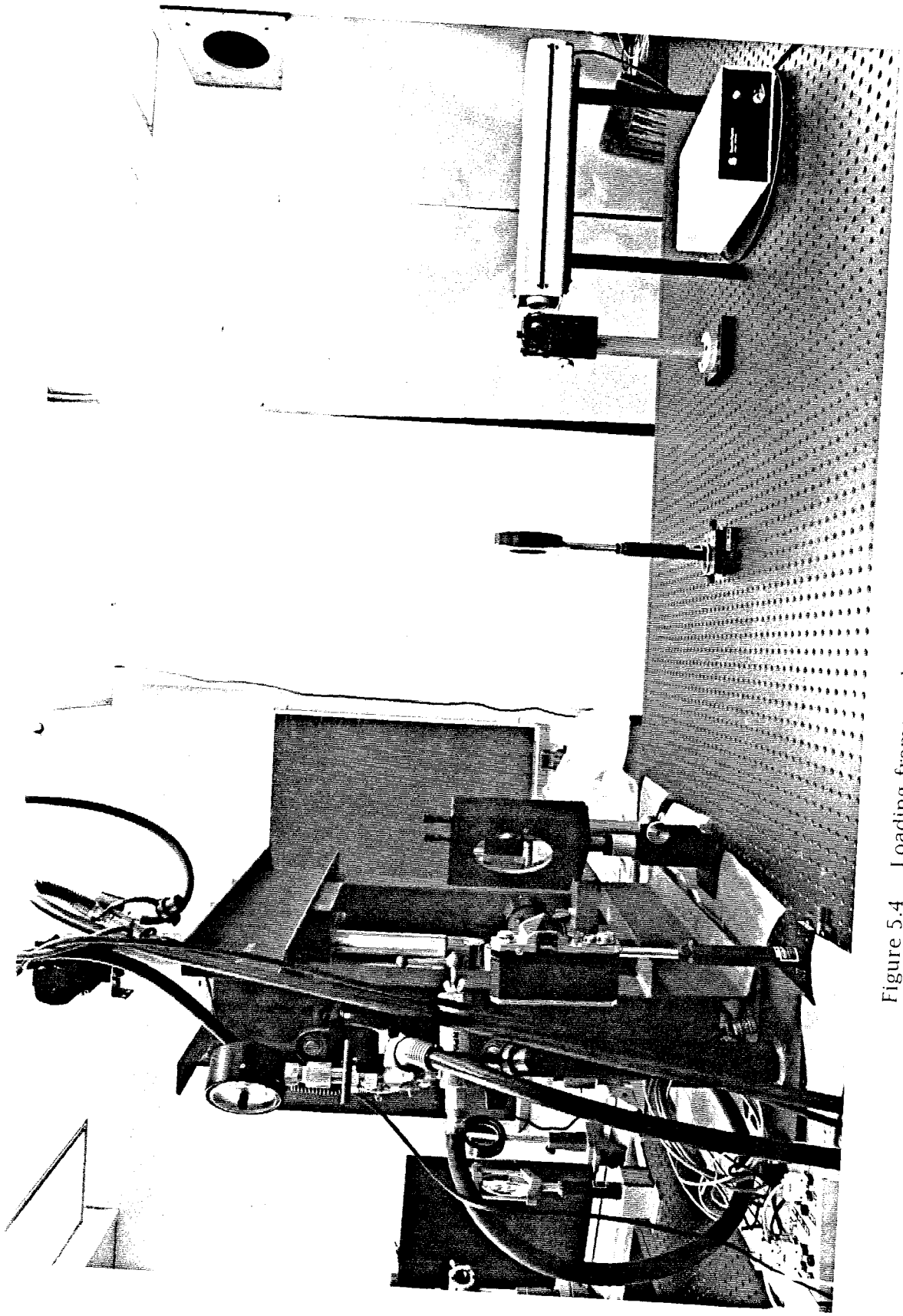

Figure 5.4 Loading frame and optics for interferometry mounted on optical table.

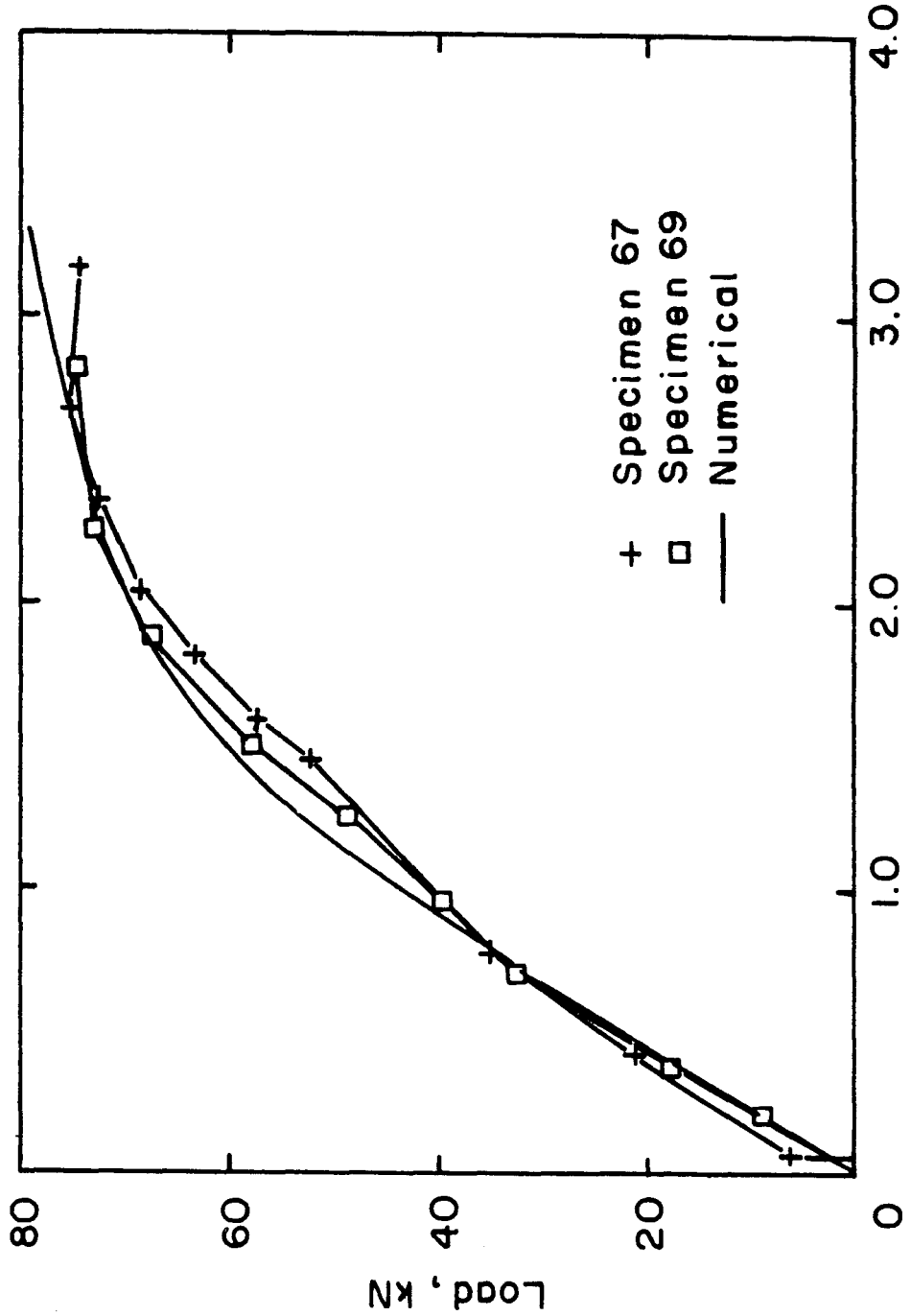

Figure 5.5 Load-load point displacement curves.

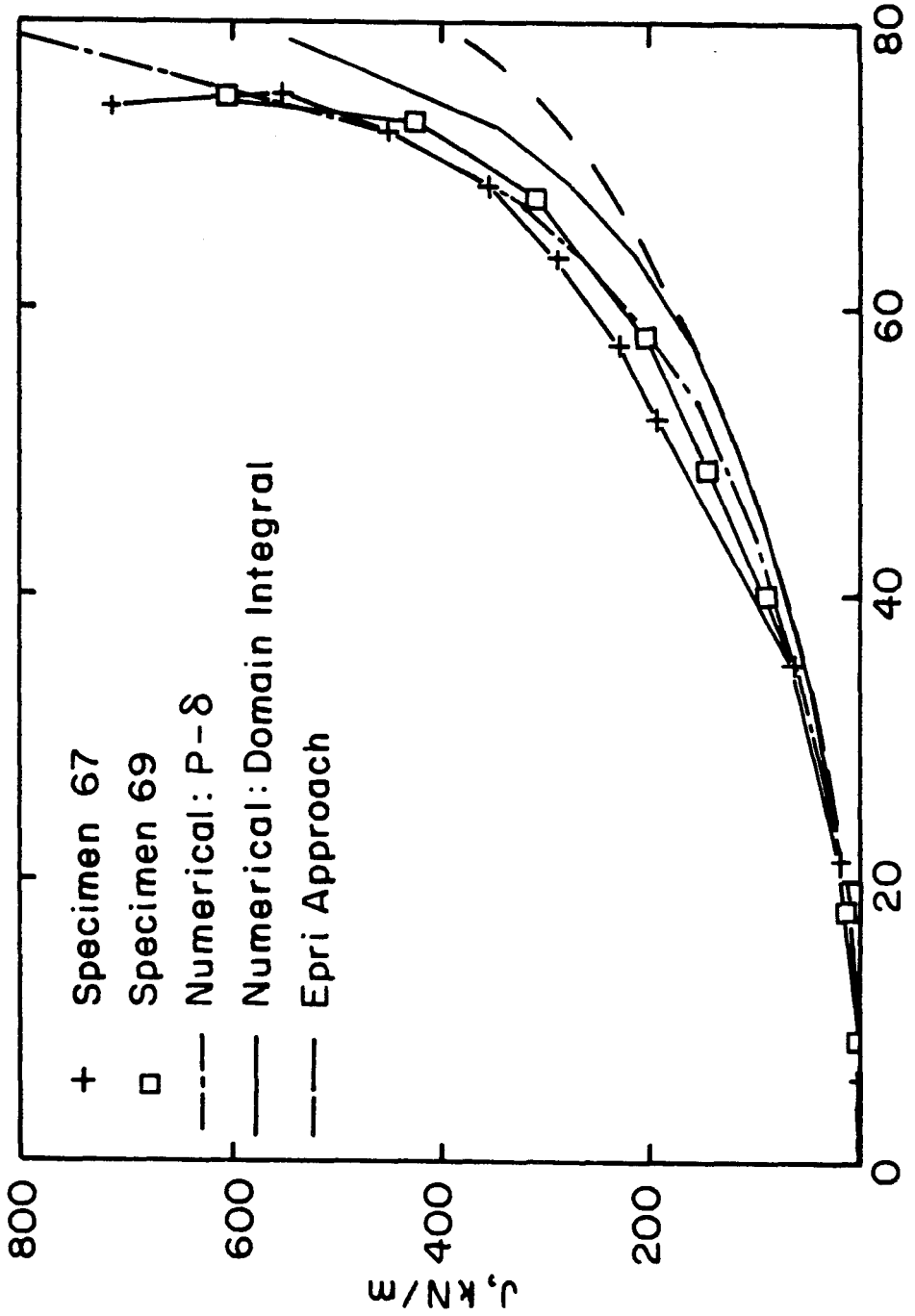

Figure 5.6 J versus P, experimental and numerical.

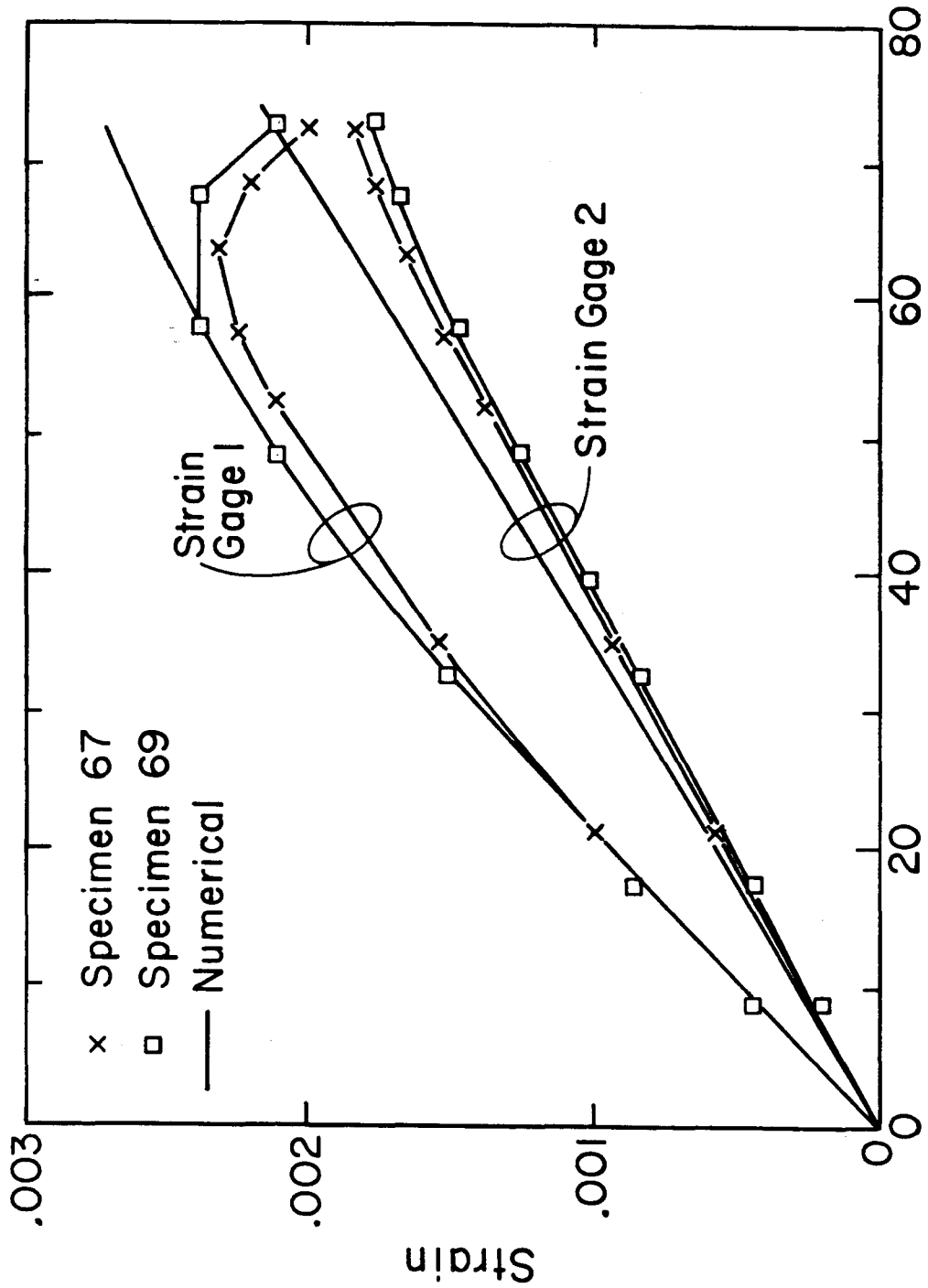

Figure 5.7 Strains versus P, experimental and numerical.

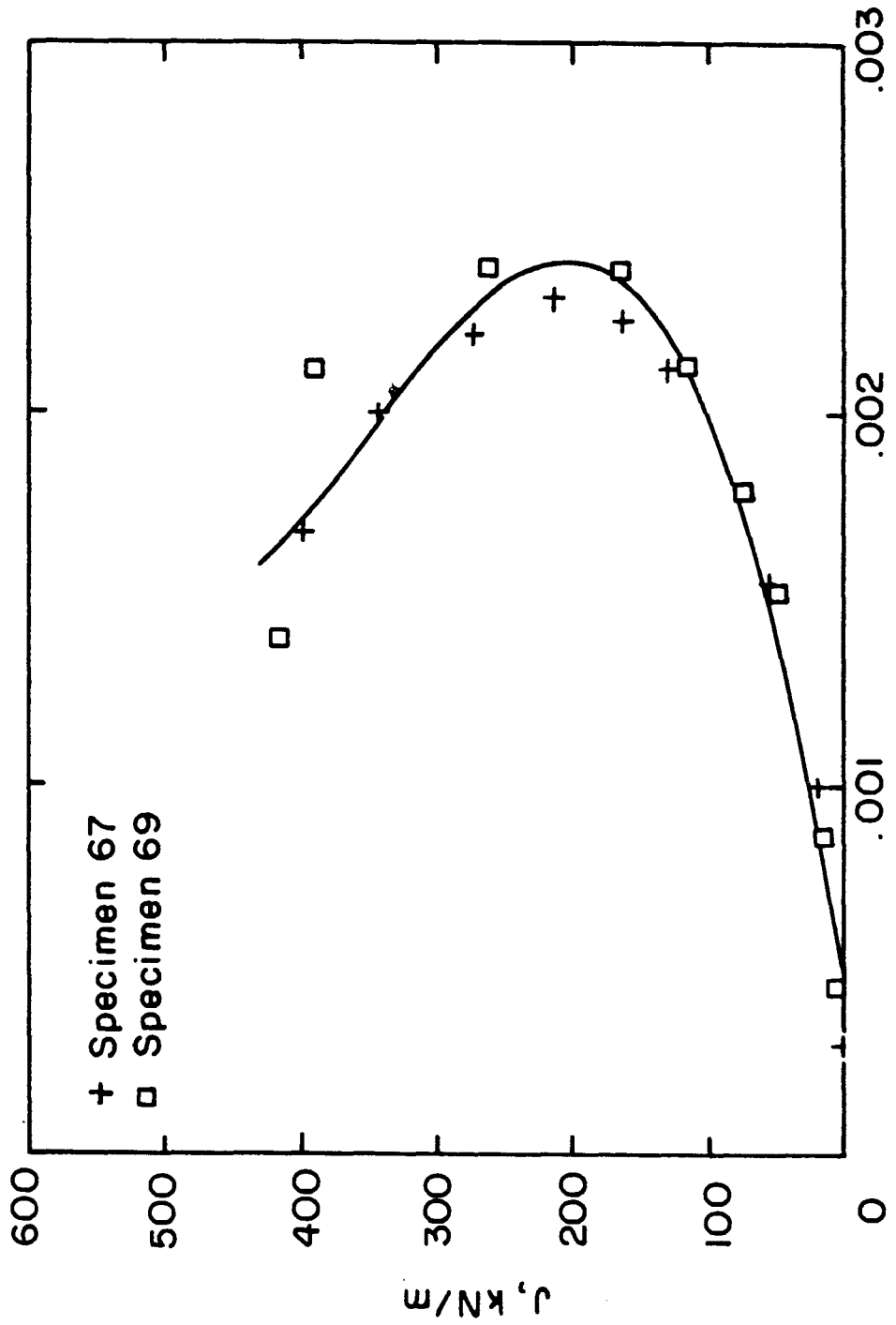

Figure 5.8 J versus strain at close gage, specimen 67 and 69 and best fit. (J from numerical domain integral)

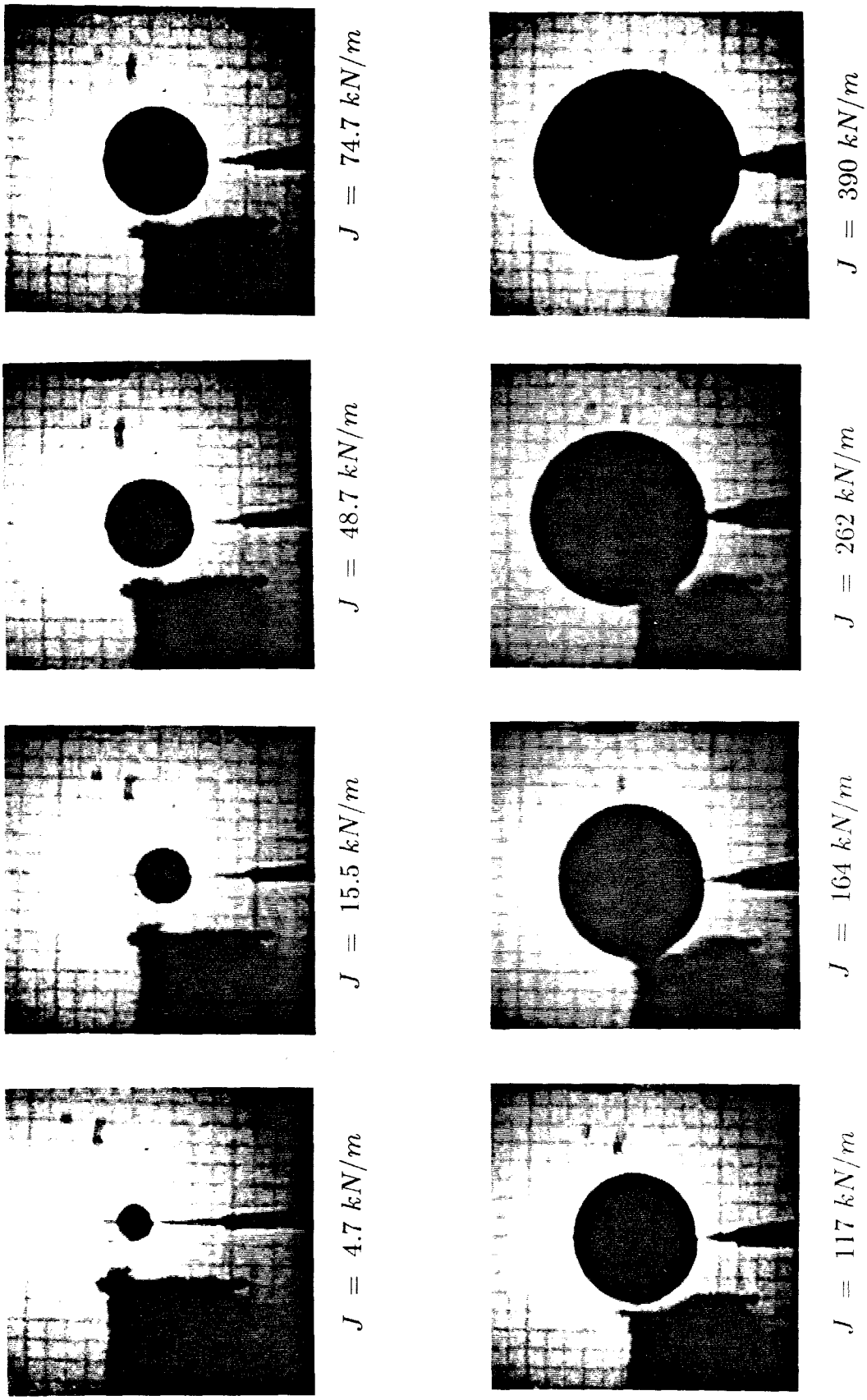

Figure 5.9 Sequence of static caustics, specimen 69, z_0=100 cm.

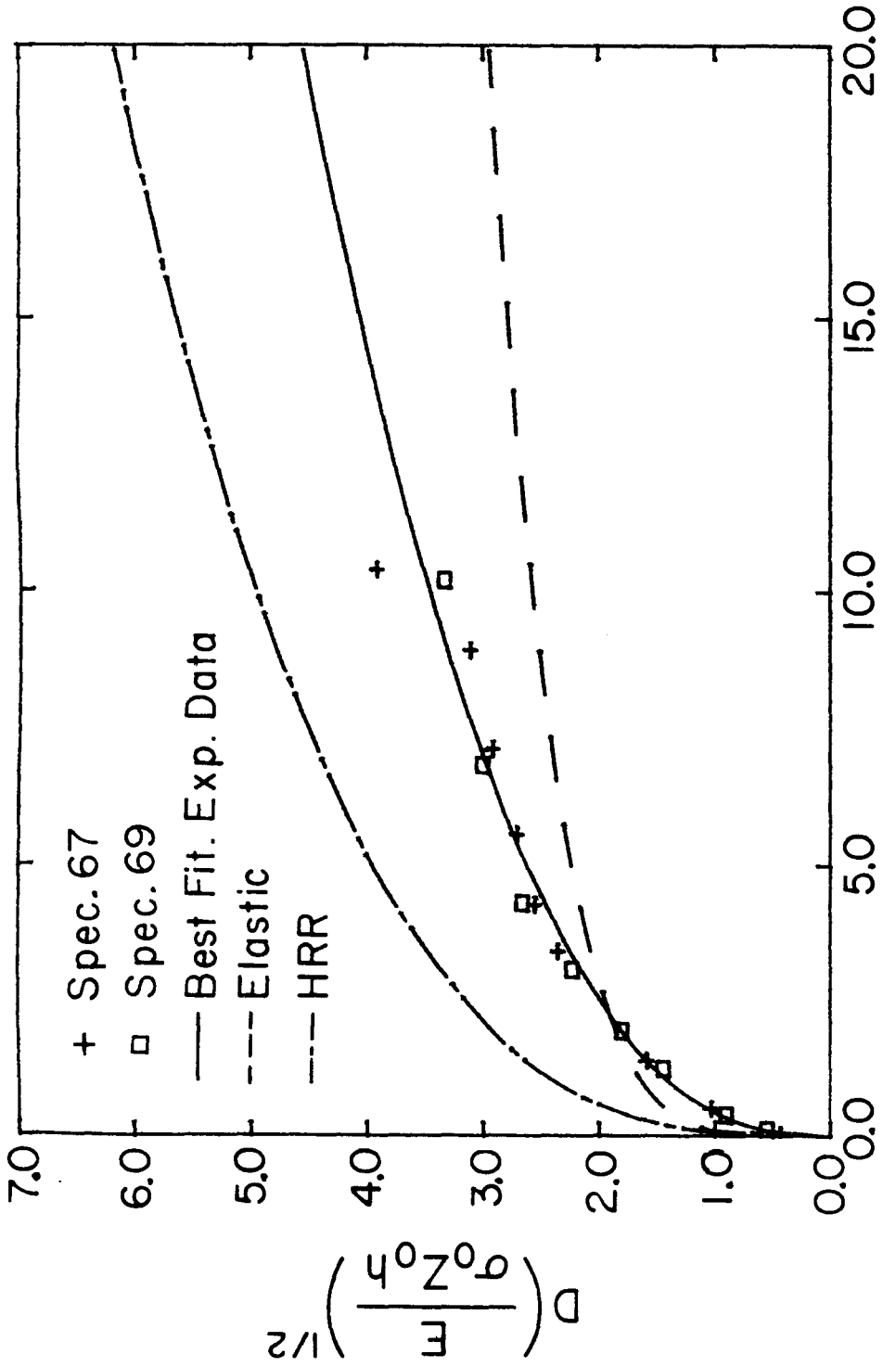

Figure 5.10 Nondimensionalized D versus J. Experimental results and best fit to results are shown along with analytical expressions for elastic caustics, equation (2.6) and HRR caustics, equation (2.9a).

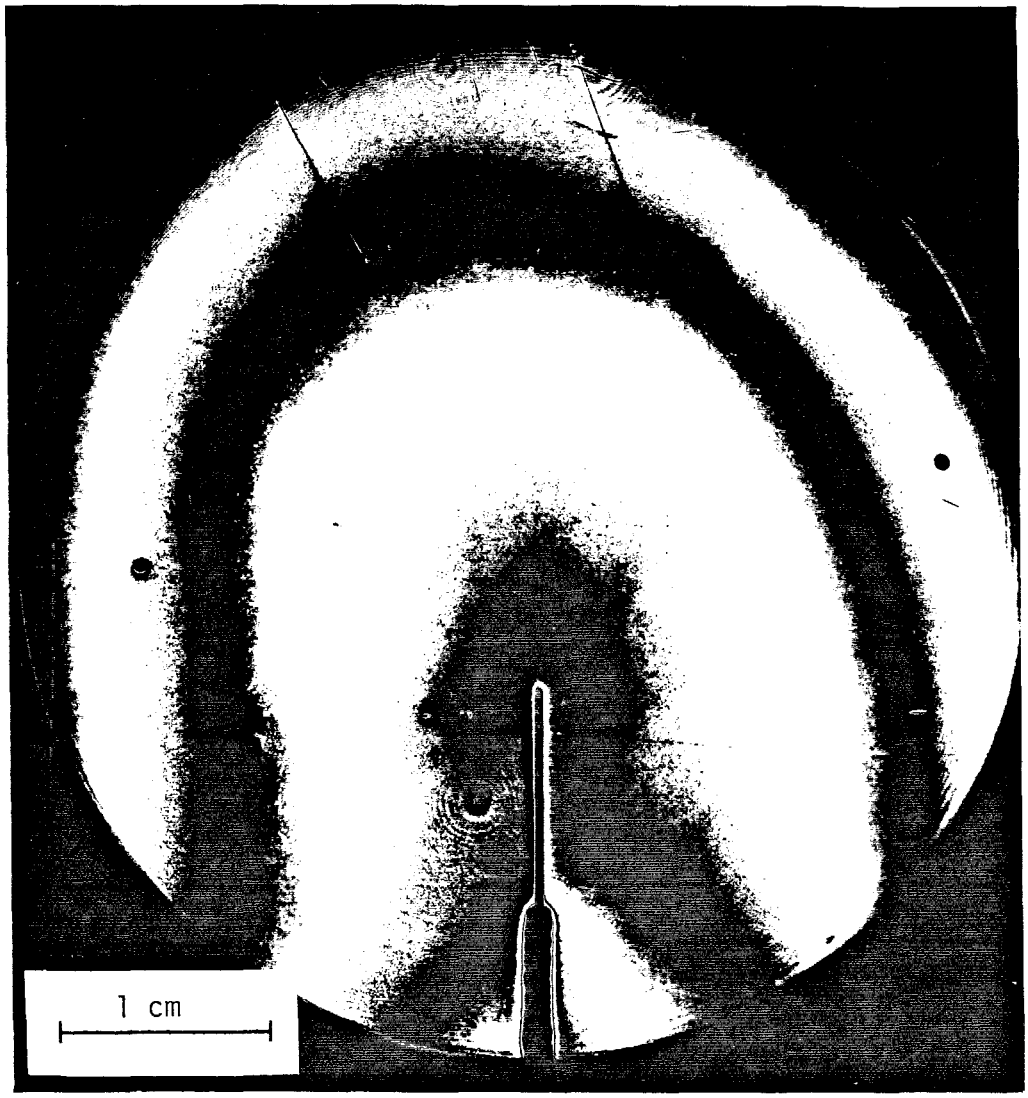

Figure 5.11 Interferogram showing initial flatness of test specimen. Area covered is 5 cm diameter.

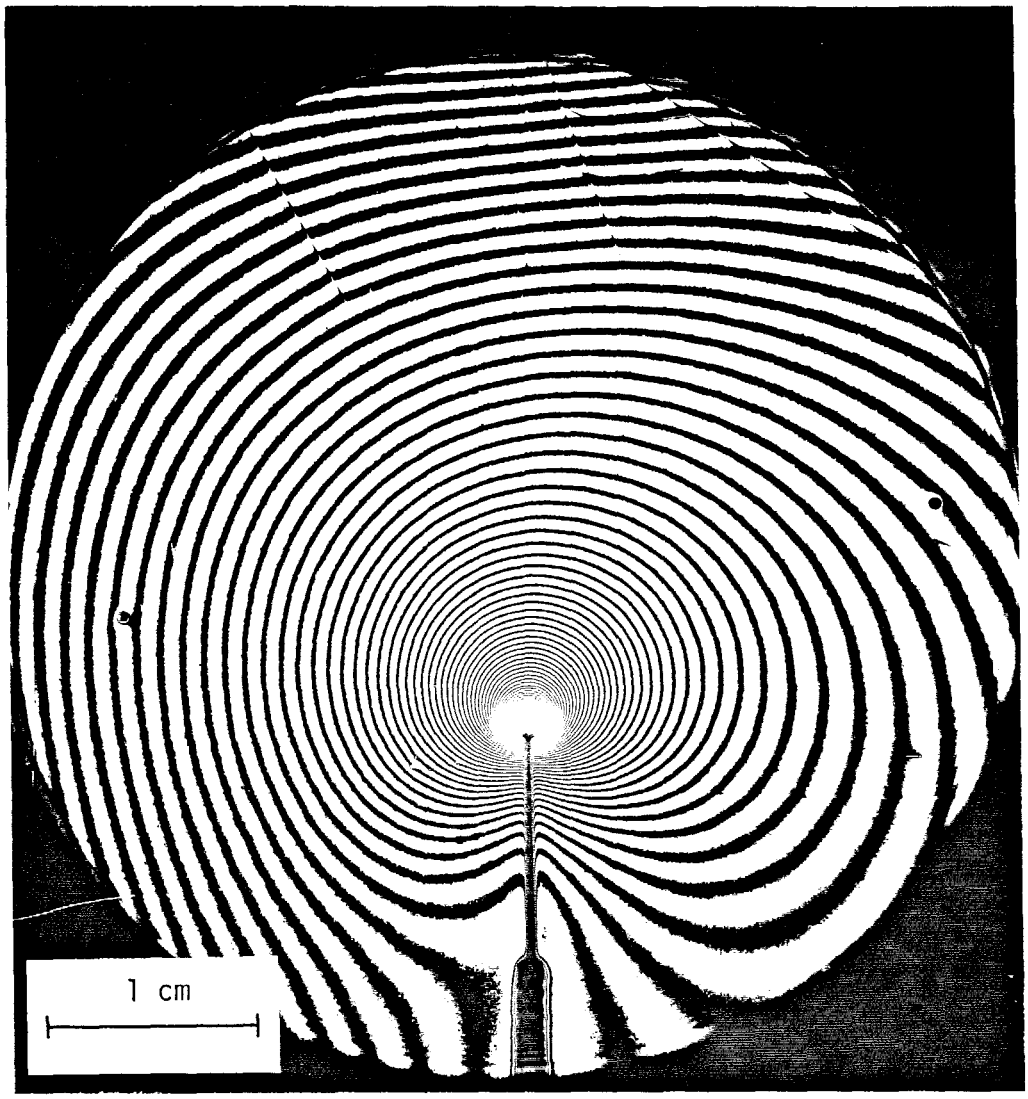

Figure 5.12 Interferogram corresponding to load of 35000 N.

Figure 5.13 Enlargement of crack tip region, 35000 N. Contrast is reverse of Figures 5.11 and 5.12.

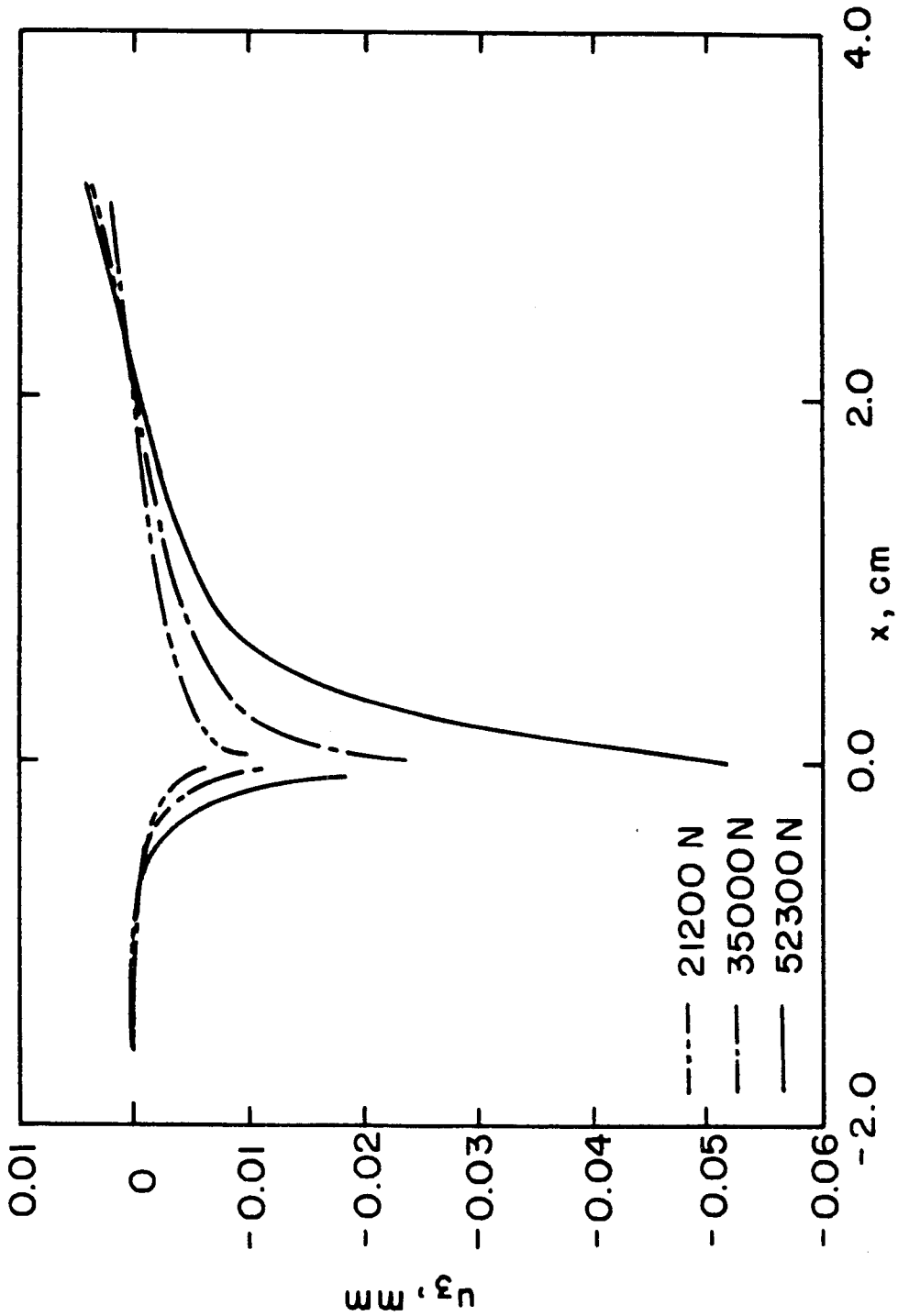

Figure 5.14 u_3 displacement along the line θ=0 for three loads.

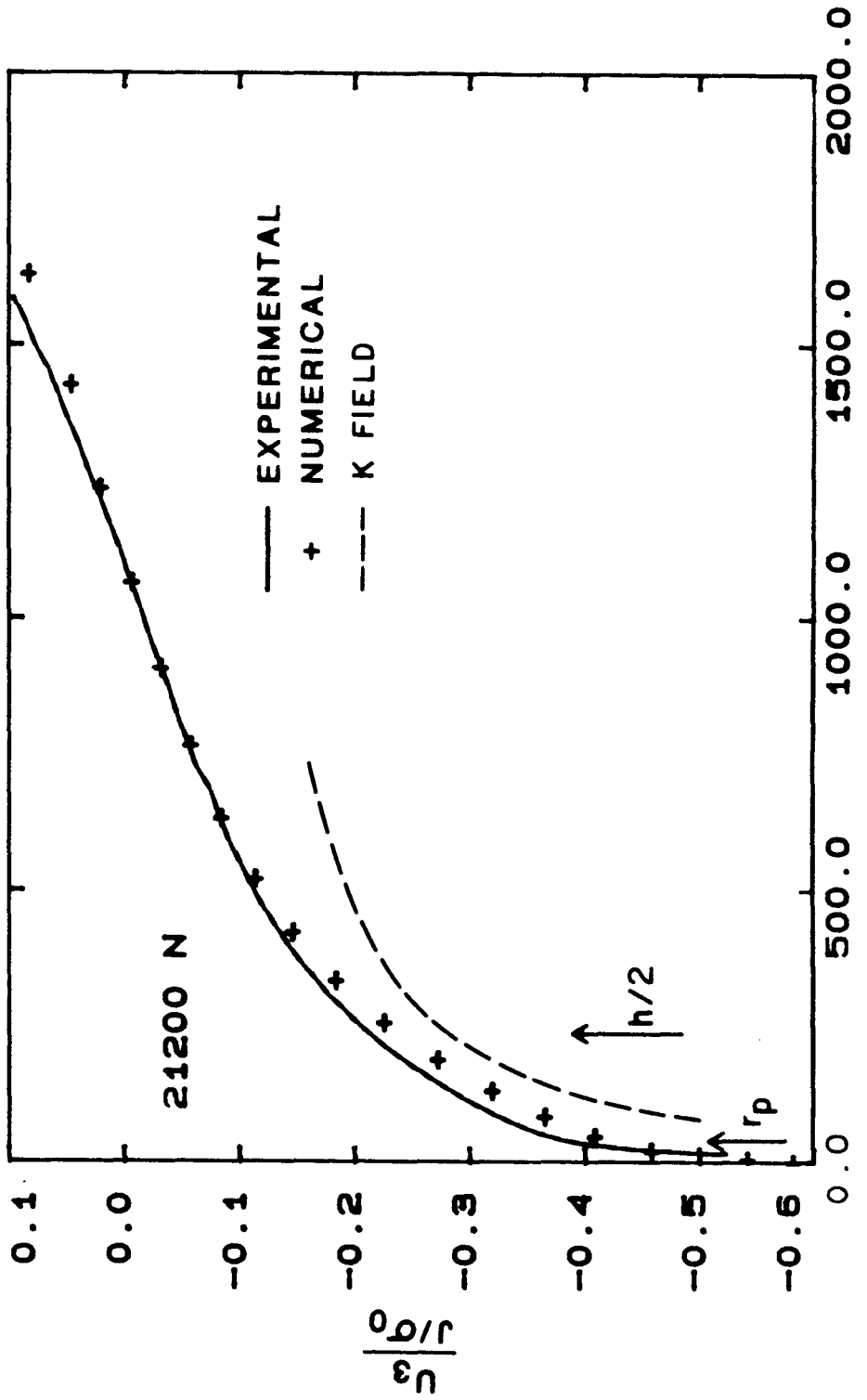

Figure 5.15 Nondimensionalized u_3 displacement on line θ=0. Comparison of experimental and numerical results for 21200 N. Also shown is K field.

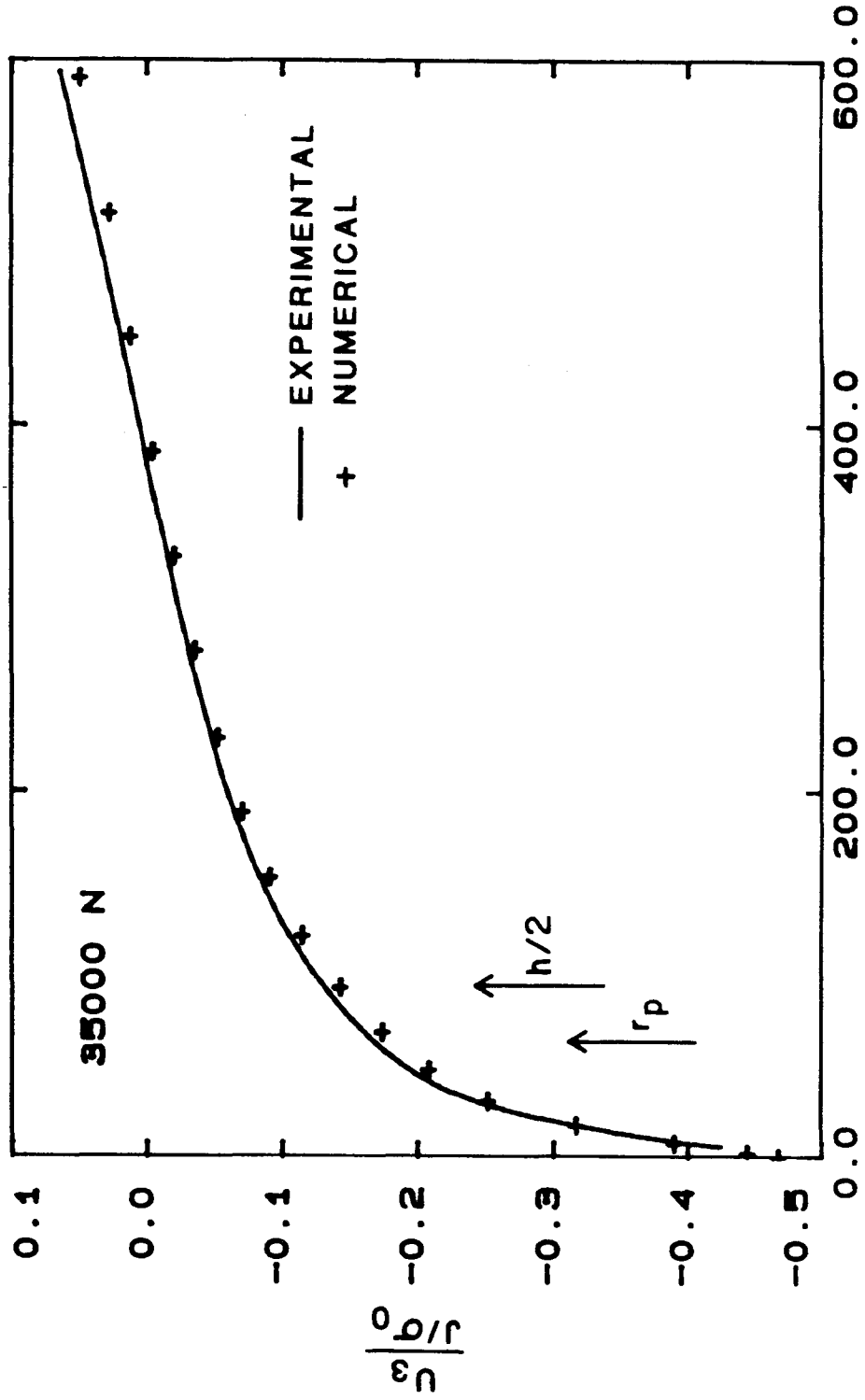

Figure 5.16 Same as Figure 5.15 for 35000 N load.

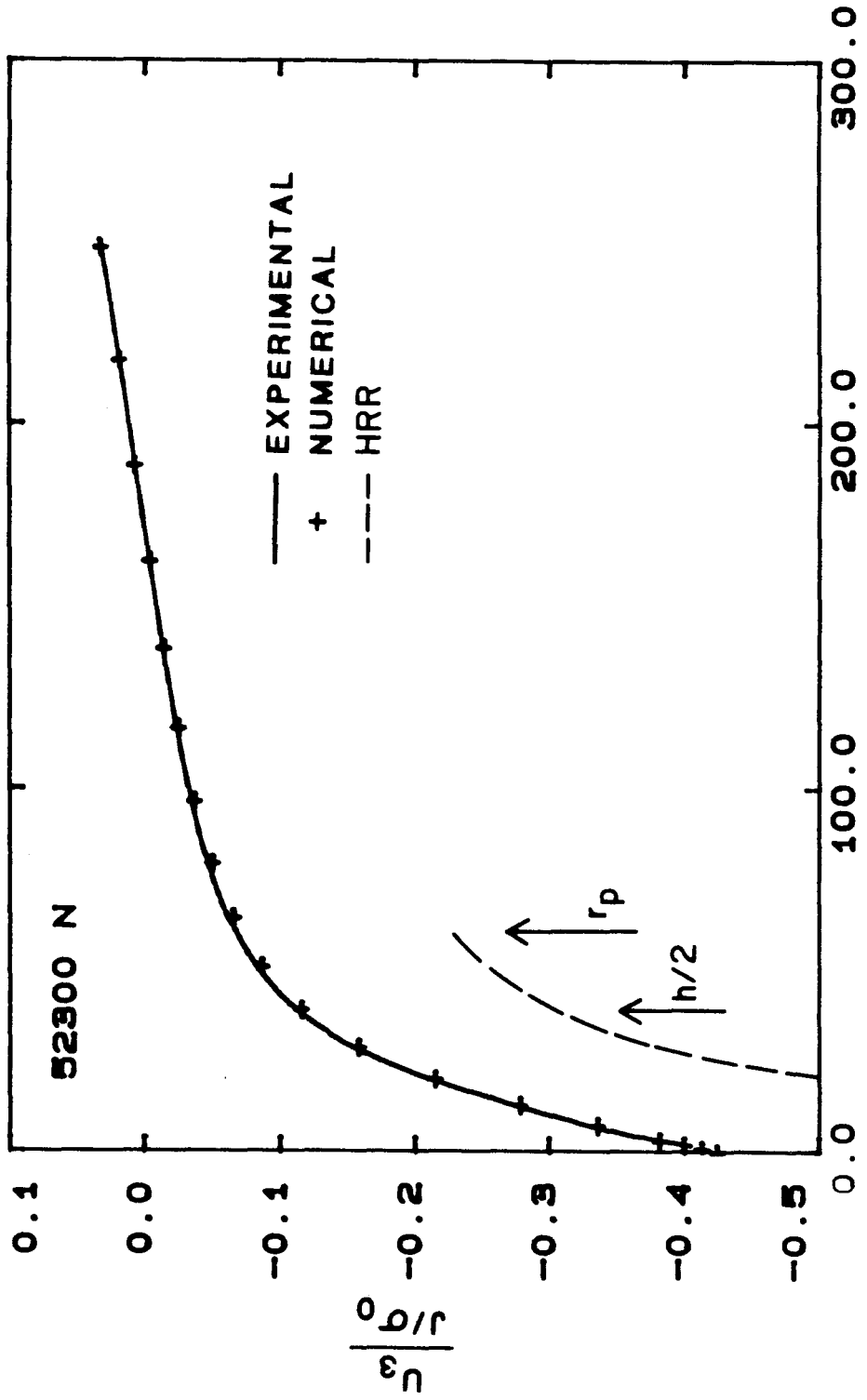

Figure 5.17 Same as Figure 5.15 for 52300 N load. Also shown is the HRR field within plastic zone.

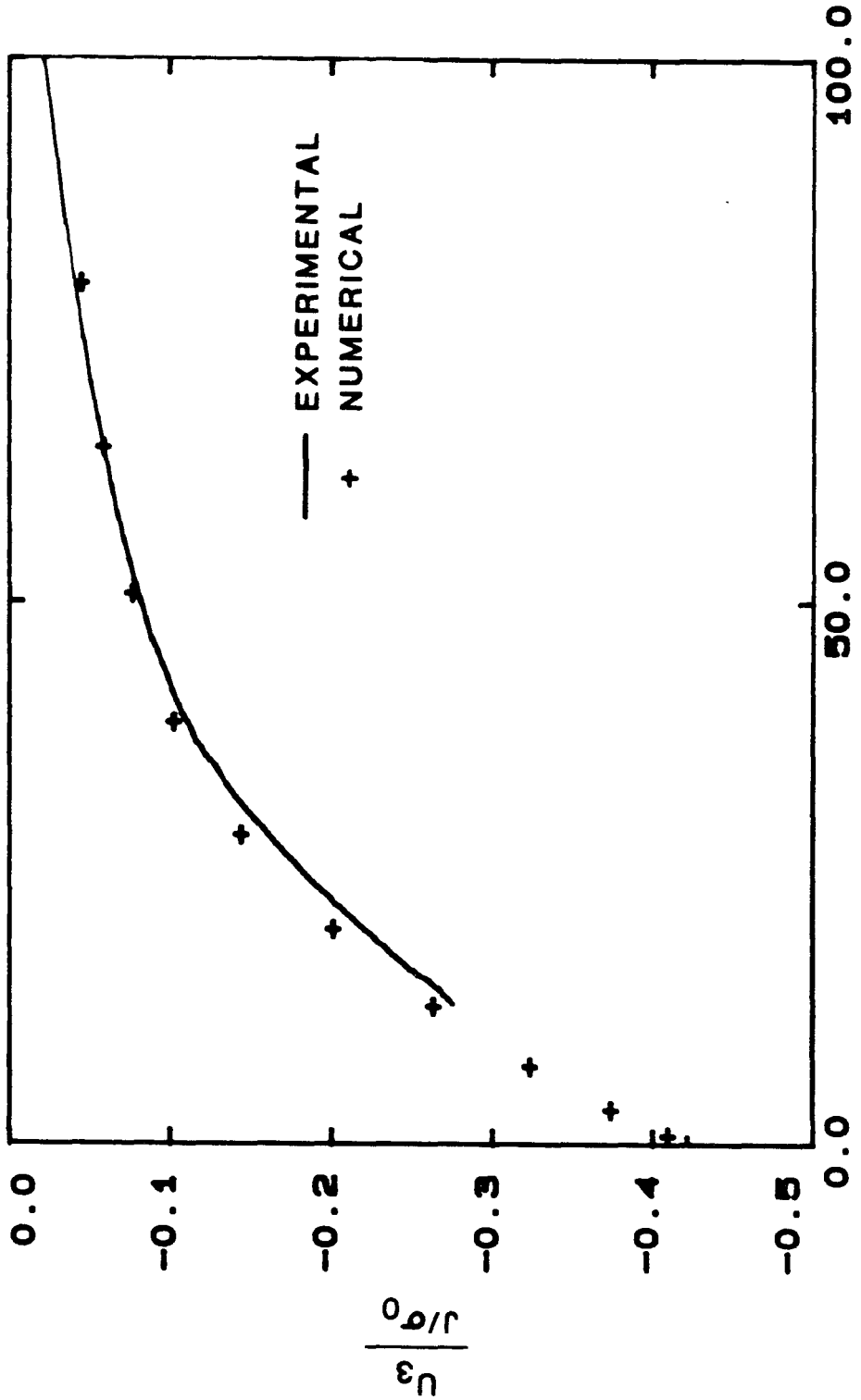

Figure 5.18 Same as Figure 5.15 for line θ=40°, for 52300 N.

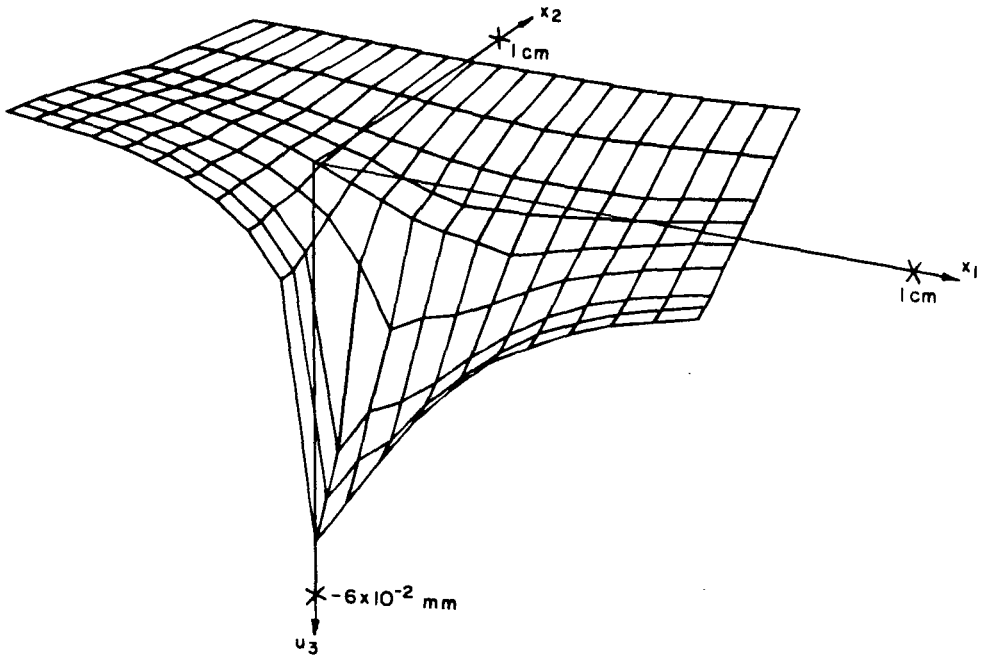

(a)

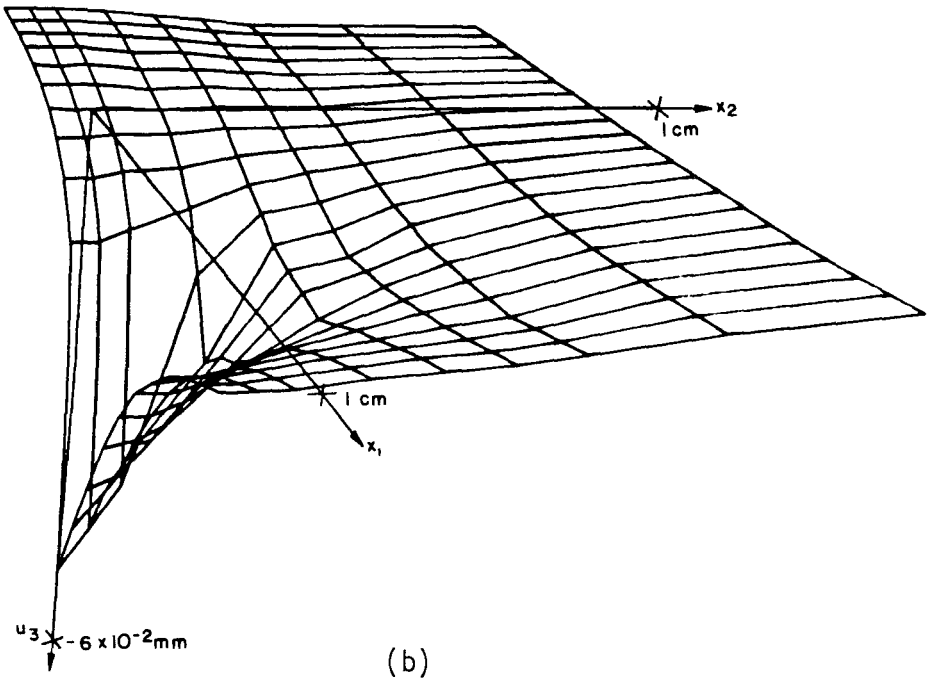

(b)

Figure 5.19 Experimental u_3 displacement for 52300 N. (a) and (b) are alternate views.

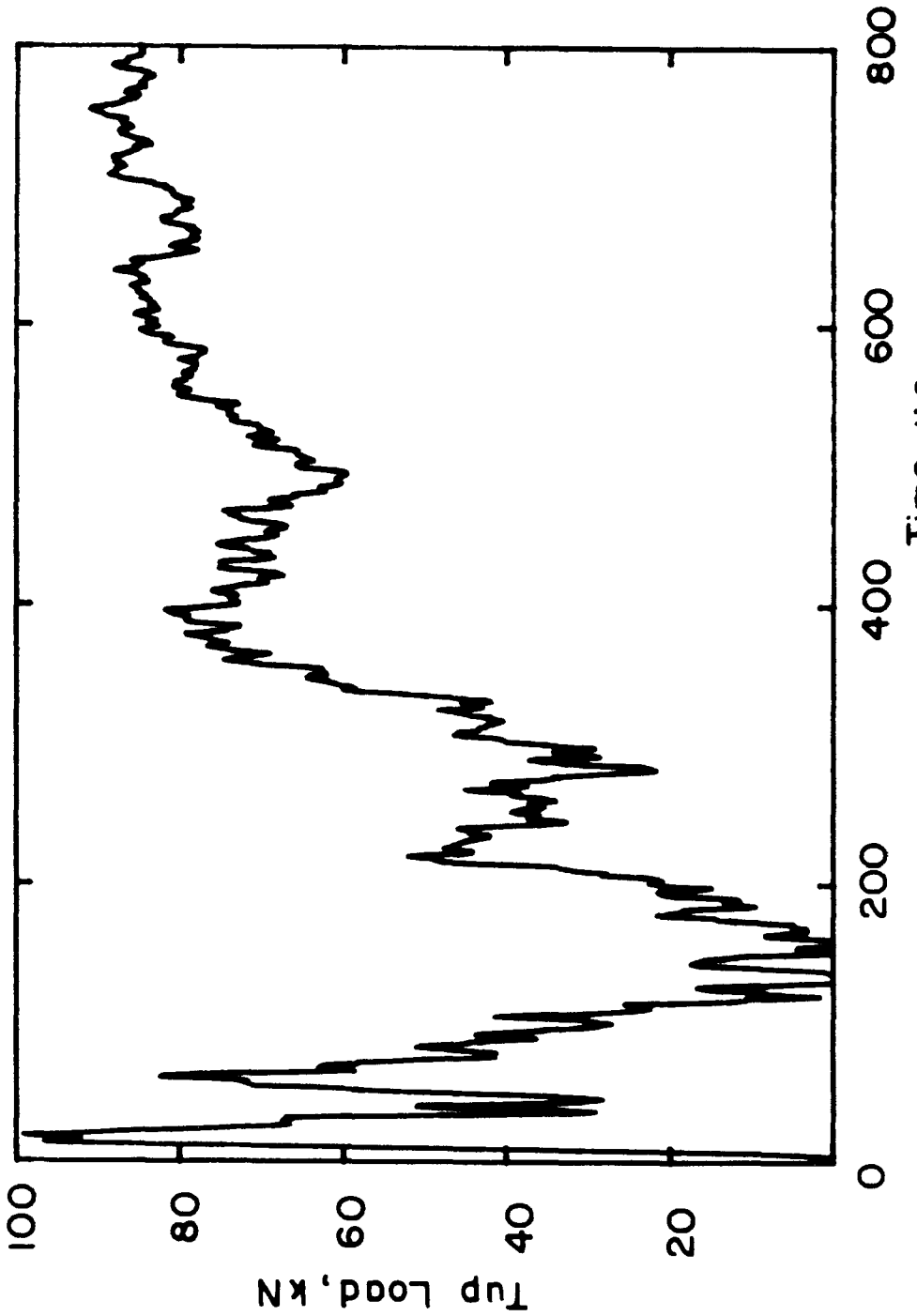

Figure 6.1 Tup load record for specimen 71.

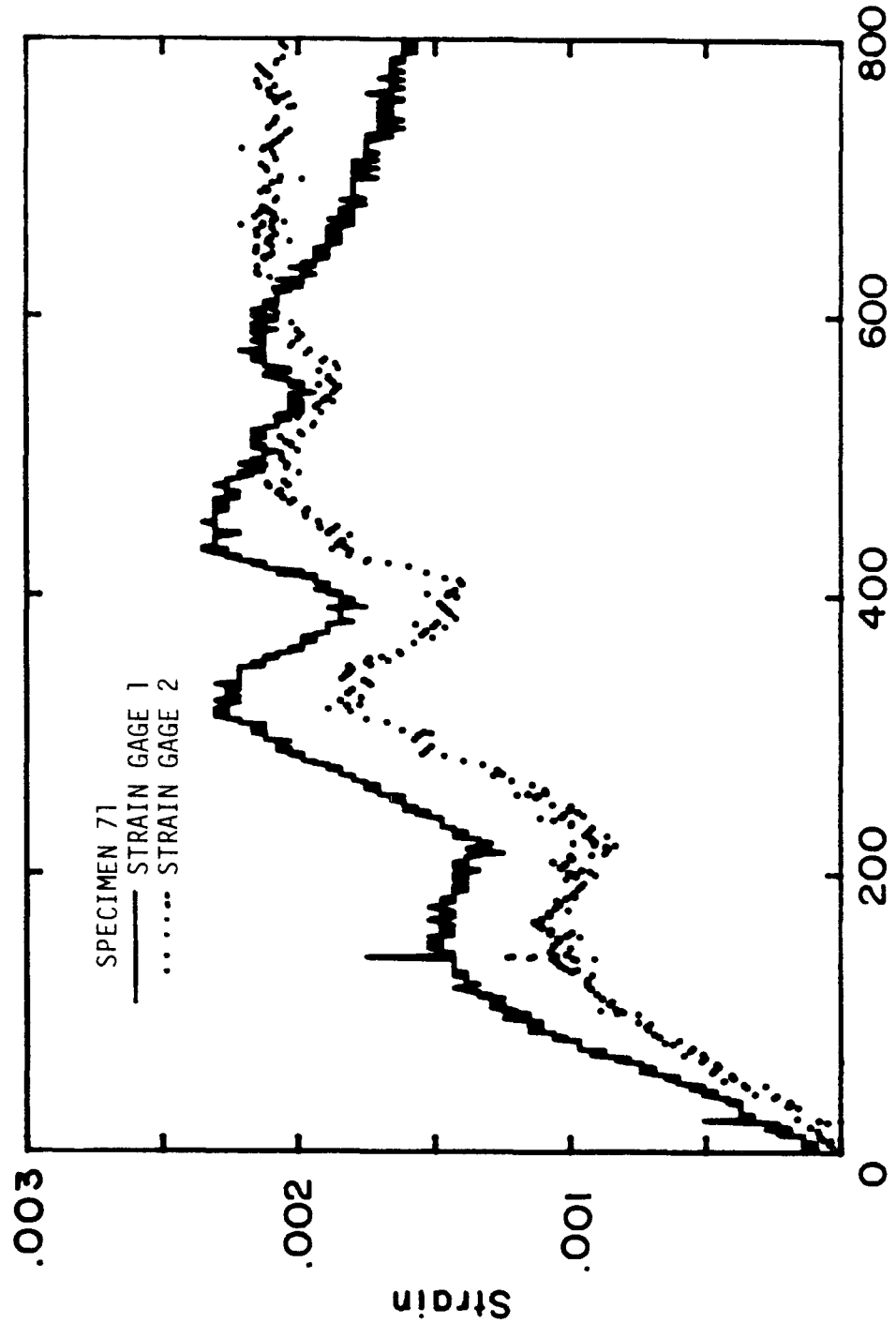

Figure 6.2 Strains measured near the crack tip, specimen 71.

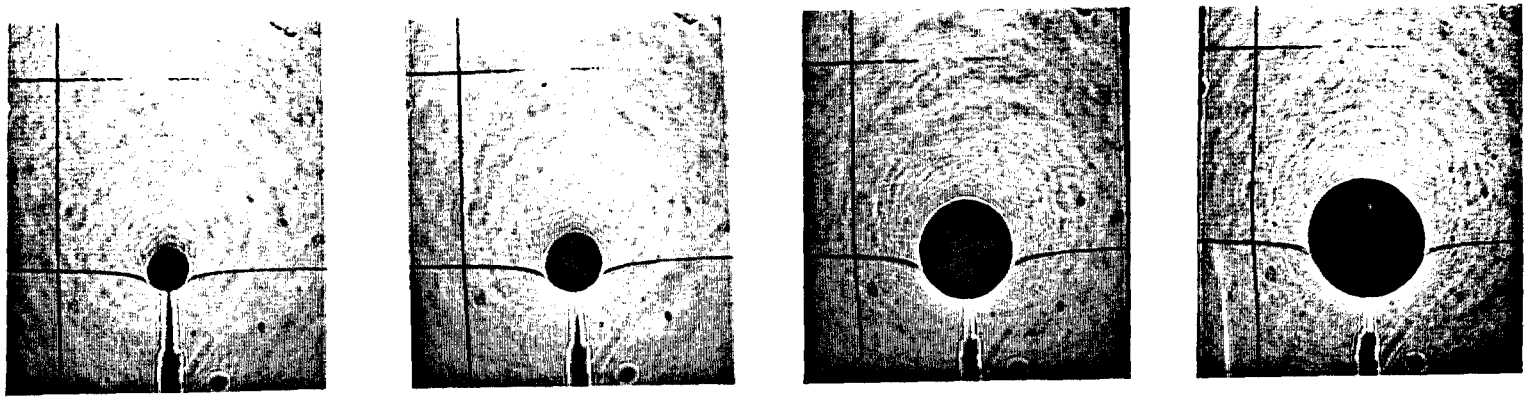

37 μs
$J = 5\ kN/m$

57 μs
$J = 11\ kN/m$

107 μs
$J = 38\ kN/m$

247 μs
$J = 70\ kN/m$

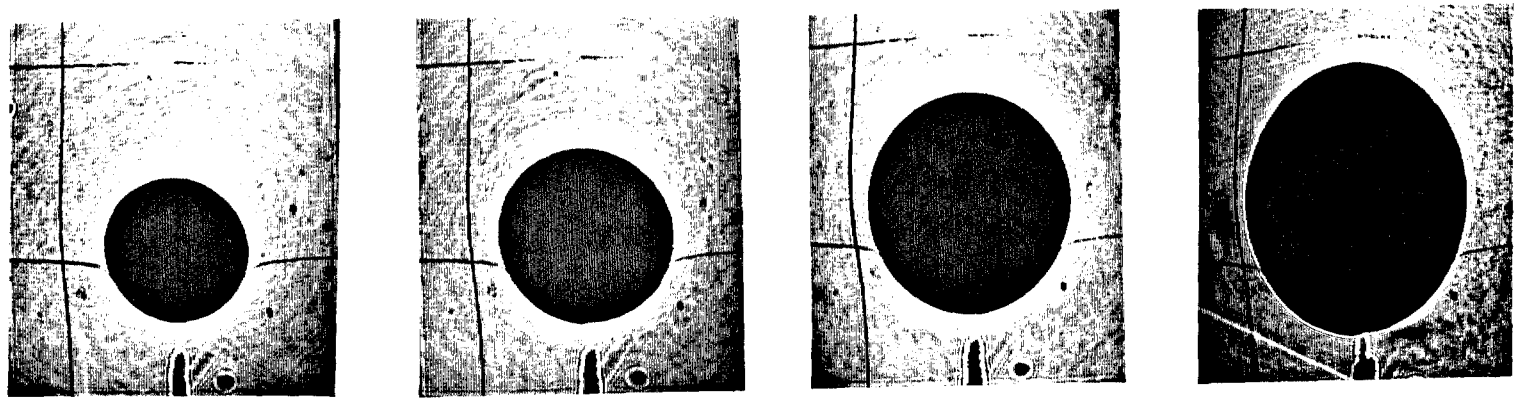

277 μs
$J = 120\ kN/m$

317 μs
$J = 196\ kN/m$

497 μs
$J = 284\ kN/m$

687 μs
$J = 345\ kN/m$

Figure 6.3 Selected caustics photographed during drop weight experiment, specimen 71.

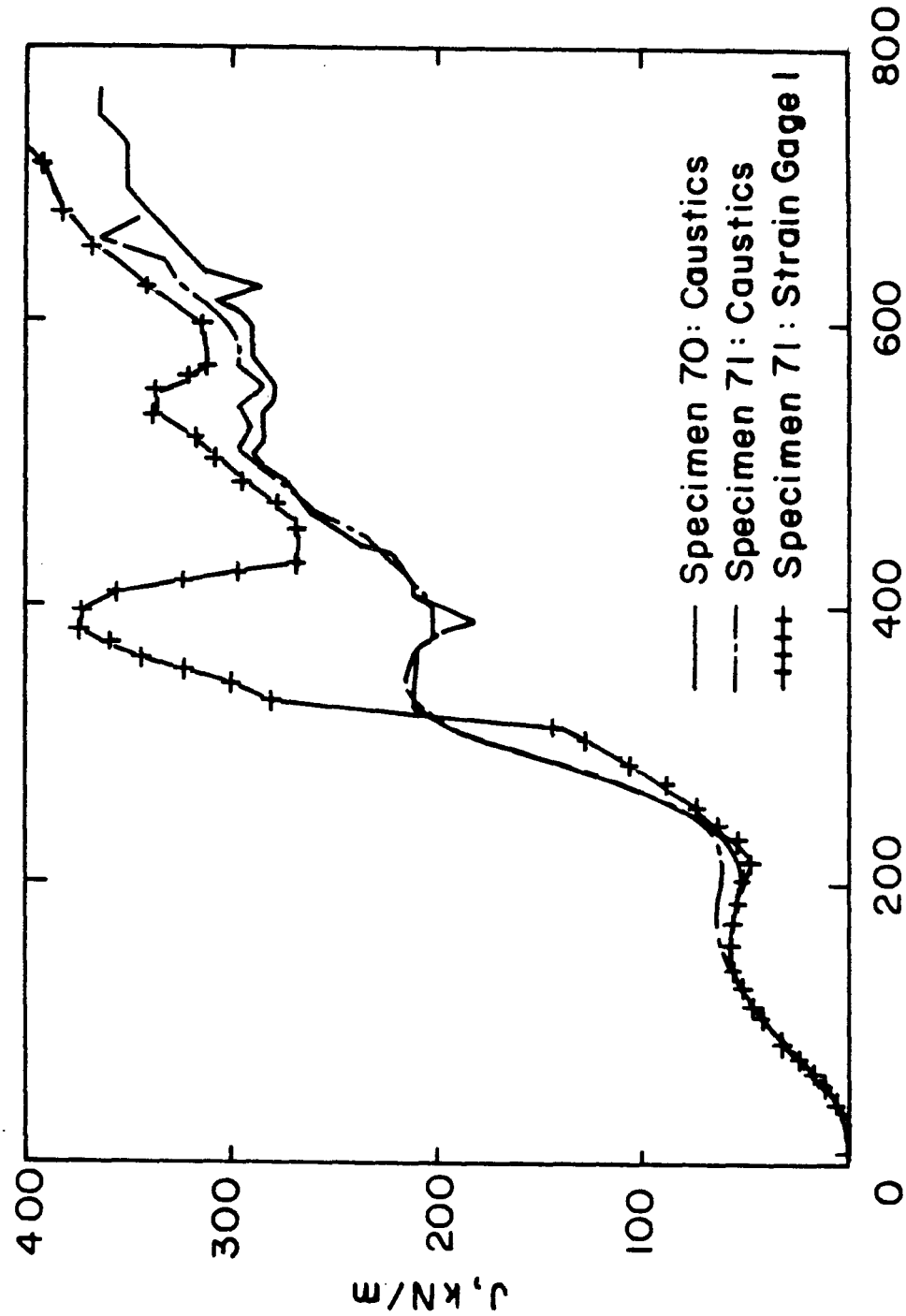

Figure 6.4 J(t) record from caustics and from strain gage. Caustics results given up to fracture initiation time.

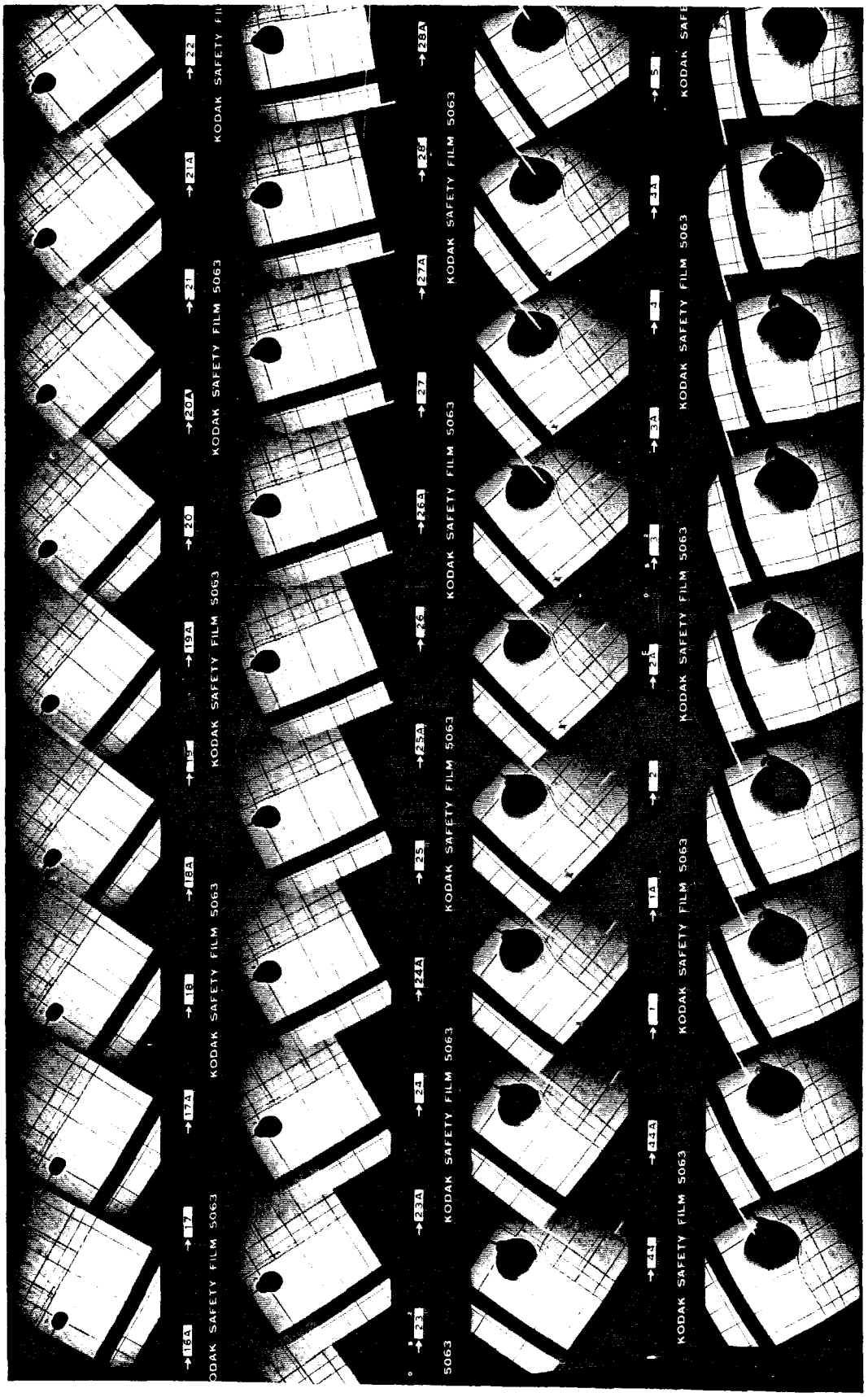

Figure 6.5 Caustics from test of a very ductile steel. Time between frames is 20 μs.

Appendix A

UNCERTAINTY IN CRACK TIP SPEED

An estimate of the precision of $\dot{a}$ is important in judging K_{IC}^{d} vs. $\dot{a}$ results. There are two factors that affect the uncertainty of the $\dot{a}$ results. One is related to the fitting used to differentiate the data and the other is related to the accuracy of the crack length measurements.

Suppose that the crack length vs. time record was measured exactly (an impossibility) at a finite number of points. One does not know for certain the crack length history between these points. Thus in order to differentiate the record a certain functional form to the a(t) record is assumed. Typical choices might be that a(t) is linear between any two points, or that it is quadratic for any three points, etc... The assumed form would then be fit to the data and differentiated to determine $\dot{a}(t)$. One way to estimate the uncertainty involved in choosing the form of the fit is to compare the $\dot{a}(t)$ results calculated from the same data but in different ways. This was done for the data from specimen 34. The results are displayed in Figure A.1 where $\dot{a}(t)$ for linear and quadratic fits are given. Also shown are uncertainty bars discussed in the following paragraphs. It is seen that in this case the choice of the fit is not critical.

Unfortunately the situation is not as simple as just choosing the proper fit. There is an uncertainty in the measured values of a and t that results in an uncertainty in $\dot{a}(t)$ no matter what fit is used. The incremental polynomial fit method used in this thesis recognizes the uncertainty in the measured data by allowing for least squares rather exact fits, causing a smoothing of the data which reduces oscillations in $\dot{a}$ due to erroneous data. Of course this procedure may also smooth out real oscillations in $\dot{a}$ in the process.

An analysis is presented here for determining the uncertainty in crack tip speed based on the uncertainty in the measured crack lengths and corresponding times. Using the analysis the uncertainty in $\dot{a}$ is calculated for two specific tests. Such estimates of the precision in $\dot{a}$ are important in judging K_{IC}^{d} vs. $\dot{a}$ results. At this time the author has never seen an estimate of the uncertainty in $\dot{a}$ given in any papers on dynamic fracture propagation.

The analysis uses the standard formulas for propagation of errors. Suppose it is required to determine the quantity g based on experimental measurements of parameters $x_1, x_2, \cdots$. If

$$g = g(x_1, x_2, \cdots)$$

where g is some known function, then the uncertainty in g is related to the uncertainties in the measured values of $x_1, x_2, \cdots$ by

$$\delta g = \left[\left(\frac{\partial g}{\partial x_1} \delta x_1 \right)^2 + \left(\frac{\partial g}{\partial x_2} \delta x_2 \right)^2 + \cdots \right]^{1/2} , \tag{A.1}$$

where δg is the uncertainty in g, and $\delta x_1, \delta x_2, \cdots$ are the uncertainties in $x_1, x_2, \cdots$.

In this thesis $\dot{a}$ was determined by using the incremental polynomial fit method. To determine $\dot{a}$ at a data point $a(t_i)$ a curve $a = C_1 + C_2 t + C_3 t^2$ is least squares fit to points $\{ a(t_{i-m}), \ldots, a(t_i), \ldots, a(t_{i+m}) \}$ where m is usually 1,2 or 3. The crack tip speed is then $\dot{a}(t_i) = C_2 + 2C_3 t_i$. When m=1 the fit becomes exact. The algebra involved for the exact fit is far simpler that for a least squares fit, thus the uncertainty was analyzed for the simpler three point fit (m=1) case.

Let a_0, a_1, a_2 be the crack lengths at times t_0, t_1, t_2. To fit the data to the assumed quadratic form the following equations must be satisfied:

$$\begin{bmatrix} 1 & t_0 & t_0^2 \\ 1 & t_1 & t_1^2 \\ 1 & t_2 & t_2^2 \end{bmatrix} \begin{bmatrix} C_1 \\ C_2 \\ C_3 \end{bmatrix} = \begin{bmatrix} a_0 \\ a_1 \\ a_2 \end{bmatrix} . \tag{A.2}$$

Only C_2 and C_3 are needed to determine $\dot{a}$. From equation (A.2) it can be seen that

$$C_{2,3} = C_{2,3}(a_0,a_1,a_2,t_0,t_1,t_2) \ ,$$

thus

$$\dot{a} = C_2+2C_3t_1 = \dot{a}(a_0,a_1,a_2,t_0,t_1,t_2) \ .$$

Let

$$\begin{array}{ll} x_1=a_0 & x_4=t_0 \\ x_2=a_1 & x_5=t_1 \\ x_3=a_2 & x_6=t_2 \end{array} .$$

Then

$$\delta\dot{a} = \left[\sum_{j=1}^{6} \left(\frac{\partial \dot{a}}{\partial x_j} \delta x_j \right)^2 \right]^{1/2} \ , \tag{A.4}$$

where

$$\frac{\partial \dot{a}}{\partial x_j} = \frac{\partial C_2}{\partial x_j}+2t_1\frac{\partial C_3}{\partial x_j} \quad j \neq 5, \tag{A.5}$$

$$\frac{\partial \dot{a}}{\partial x_5} = \frac{\partial C_2}{\partial x_5}+2t_1\frac{\partial C_3}{\partial x_5}+2C_3 \quad j=5.$$

It is useful to examine some specific cases of equation (A.4). Let Δt be the time interval between measurements, and let Δa be the increment in crack length during that time. For a constant $\dot{a}$,

$$C_2 = \frac{\Delta a}{\Delta t} = \frac{a_2 - a_0}{t_2 - t_0} \quad , \quad \text{and} \quad C_3 = 0.$$

In this case

$$\frac{\delta \dot{a}}{\dot{a}} = \frac{1}{\sqrt{2}} \left[\left(\frac{\delta a}{\Delta a} \right)^2 + \left(\frac{\delta t}{\Delta t} \right)^2 \right]^{1/2} \quad . \tag{A.6}$$

This relationship indicates the relative accuracy with which a and t must be measured in order to achieve a certain accuracy in $\dot{a}$.

Using equation (A.4) some specific results were analyzed. For test specimen 34 the crack length could be measured to an accuracy of between $\pm .02 mm$ and $\pm .06 mm$. The details of the data are given in Table A.1. For this test δt was taken as zero since the time intervals of measurement were fixed and known to an accuracy of better than 1 in 200. The uncertainty δa is not constant since there are differences in the clarity of the caustics photographs from frame to frame. The resulting $\dot{a}$ and the uncertainty $\delta \dot{a}$ are given in Figure A.1. The uncertainty in $\dot{a}$ is relatively large; within the experimental accuracy the crack tip speed can be considered constant for the first $40 \mu s$.

Techniques other than optical ones are available for recording crack length. In a series of tests performed at Caltech in cooperation with Southwest Research Institute wedge loaded DCB specimens were tested. Using techniques and materials developed by Southwest Research Institute crack length was measured by recording the breaking of conductive strips on the specimen surface. Twelve strips, each approximately 0.4 mm wide with a spacing of 5 mm were used as shown in Figure

A.2.

The uncertainty in a is taken as one-half the width of a strip (0.2 mm). The uncertainty in the time of breaking of each strip ranges from $\pm .05\mu s$ to $\pm .40\mu s$. The complete data are given in Table A.2. The resulting $\dot{a}$ and $\delta\dot{a}$ are given in Figure A.3. In this case $\delta\dot{a}$ is relatively small. These results show that careful use of conductive strips can produce data with approximately twice the precision of optical measurements using caustics. It is suggested that conductive strips be used in conjunction with optical caustics measurements in order to improve the precision of the results.

Table A.1 Specimen 34 Data

time μs	a cm	δa cm	$\dot{a}$ m/s	$\delta\dot{a}$ m/s
650	.39	.03	1020	
655	.89	.02	980	42
660	1.37	.03	1020	53
665	1.91	.05	1060	67
675	2.93	0.6	953	82
680	3.39	.04	949	78
685	3.88	.05	990	64
690	4.38	.05	990	70
695	4.87	.05	860	70
700	5.24	.05	739	70
705	5.61	.05	740	70
710	5.98	.05	740	

Table A.2 Specimen 52 Data

Time μs	δt μs	a cm	δa cm	$\dot{a}$ m/s	$\delta \dot{a}$ m/s
7.5	.20	1.00	.02	1220	
11.6	.15	1.50		1000	46
17.4	.10	2.00		799	29
24.3	.20	2.50		848	32
29.6	.10	3.00		870	33
36.0	.05	3.50		808	24
42.0	.05	4.00		744	28
50.0	.10	4.50		753	30
55.9	.15	5.00		791	30
62.8	.4	5.50		656	28
71.6	.25	6.00		474	30
88.7	.2	6.50	.02	110	

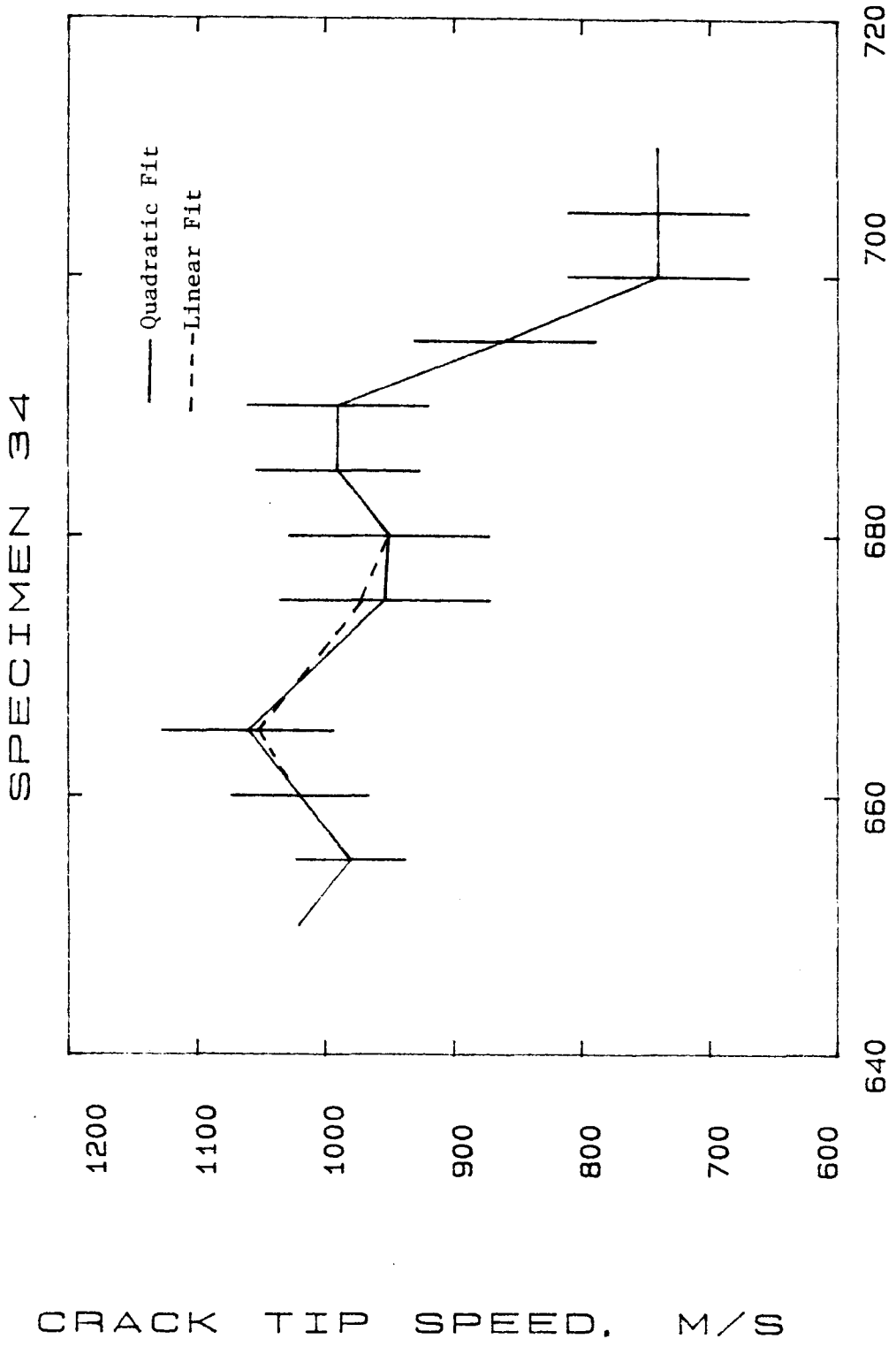

Figure A.1 Crack tip speed and uncertainty in crack tip speed for specimen 34. Uncertainty is indicated by error bars.

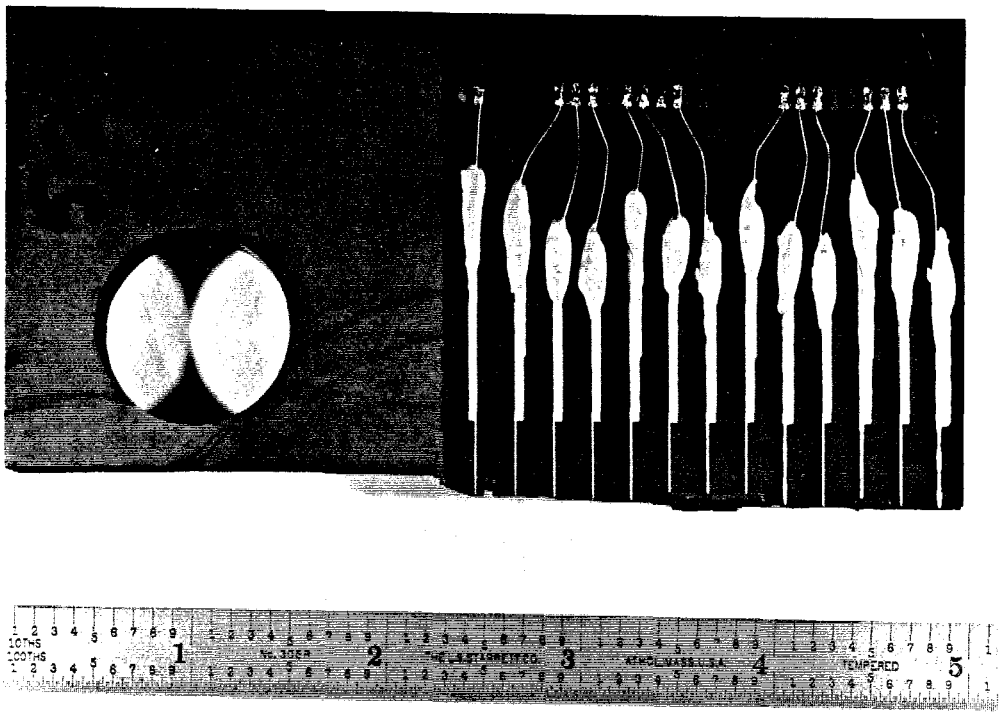

Figure A.2 Conductive strips used for testing specimen 52.

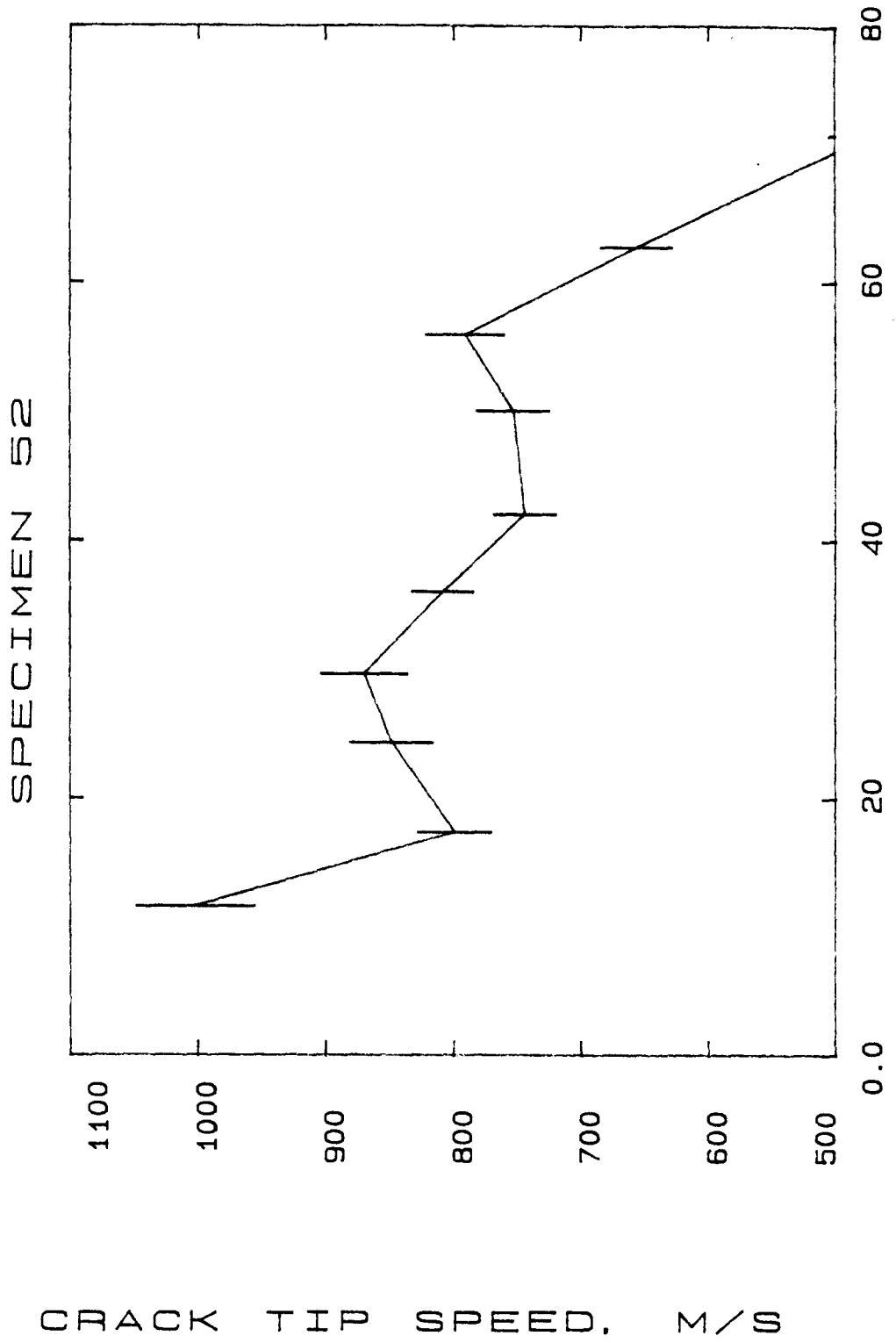

Figure A.3 Crack tip speed and uncertainty in crack tip speed for specimen 52.

Appendix B

ANALYSIS OF ERROR FOR INTERFEROMETRY

Due to the angular deflection of the reflected light rays, as seen in Figure B.1, there exists some error in interferometry when using the relation $S=2u_3$, where S is the optical path length and u_3 is the out of plane displacement. Additional error occurs because the angular deflection changes the location of the fringes.

The camera that photographs the interference pattern is focused on a reference plane located a distance z_0 behind the undeformed specimen surface, as sketched in Figure B.1. The mapping of light rays from the specimen surface (x_1,x_2 coordinates) to the reference plane (X_1,X_2 coordinates) was given in equation (2.2) as

$$\underline{X} = \underline{x} - 2(z_0 - f) \cdot \frac{\underline{\nabla} f}{1 - |\underline{\nabla} f|^2} \quad ,$$

where $x_3 = -f(x_1,x_2) = u_3(x_1,x_2)$ describes the deformed specimen surface. The error in fringe location is equal to the deflection of the light ray, that is if we call $\delta\underline{X}$ the "error vector" then

$$\delta\underline{X} = -2(z_0 - f) \cdot \frac{\underline{\nabla} f}{1 - |\underline{\nabla} f|^2} \quad . \tag{B.1}$$

The difference between the true optical path and the approximate optical path is the difference in magnitude of the vectors

$$\underline{S}_{true} = \left[(z_0 - f)^2 + \delta X_1^2 + \delta X_2^2\right]^{1/2} \cdot \frac{\underline{\nabla} f}{|\underline{\nabla} f|}$$

and

$$\underline{S}_{\approx} = -(z_0 - f)\underline{e}_3 \ .$$

Thus the error in optical path δS is

$$\delta S = \left[\delta X_1^2 + \delta X_2^2 + (z_0 - f)^2\right]^{1/2} - (z_0 - f) \ . \tag{B.2}$$

Since in the analysis of the interferograms it was assumed that $S = f = u_3$, the error in S, δS represents the absolute error in the measured values of u_3.

Equation (B.1) shows that to minimize the error, the product $(z_0 - f)\cdot\dfrac{\nabla f}{1 - |\nabla f|^2}$ must be minimized. This was done by focusing the camera on the crack tip so that $(z_0 - f) = 0$ at the crack tip, where ∇f is largest.

A quantitative estimate of the error can be obtained by putting the measured u_3 values into equation (B.1). This was done for the results corresponding to specimen 67 at a load of 52 300 N. Only data along the line $x_2 = 0$ were analyzed. In this case $\dfrac{\partial u_3}{\partial x_2} = 0$ due to symmetry, thus $\delta X_2 = 0$. The error is zero at the crack tip and is nearly constant but small for $x_1 > 1$ cm. The maximum error in fringe location is only $\approx 0.7\lambda$ and the maximum error in u_3 is only $\approx .01\lambda$. This represents an error in u_3 of approx. 0.02% and an error in x_1 of approx. 0.02%. With increasing deformation the errors will increase. However so will the fringe density, and when the fringe density surpasses the recording resolution no data can be obtained; so there is little point in worrying about the accuracy for very large deformations.

The main source of error is the uncertainty in the location of the crack tip and the accuracy limitations in digitizing the interferograms. As seen in the interference photographs, Figures 5.12 and 5.13, the crack tip is obscured by a small caustic, limiting how close to the crack tip fringes may be resloved. Enlargements (50 X) of the interferograms were digitized by hand using a computer digitizing pad. The

center of each dark fringe was estimated by eye. Clearly this can introduce an error much larger than the 0.7λ theoretical error. More accurate (and less tedious) computerized image processing could reduce even this error to almost zero.

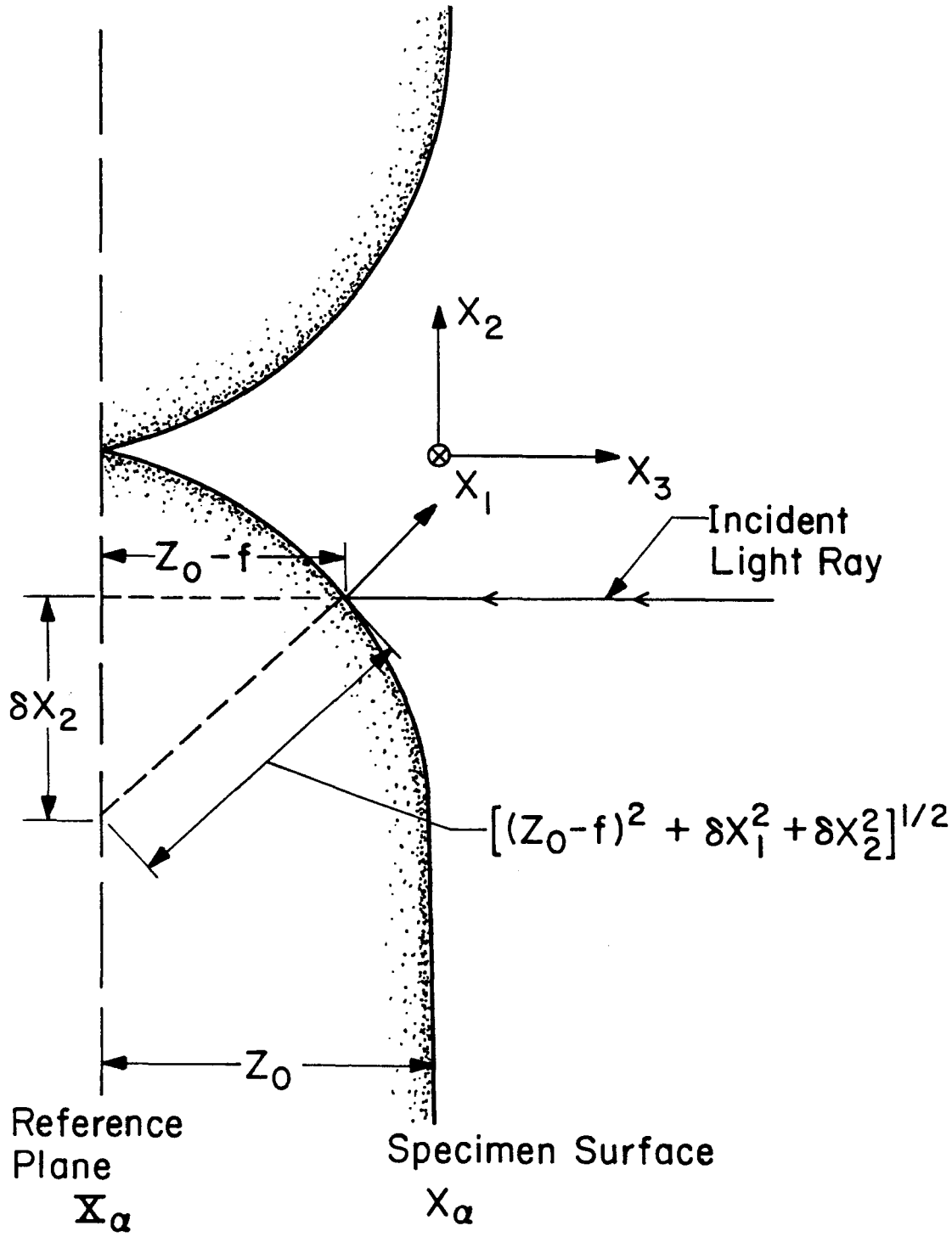

Figure B.1 Geometry of light reflection from deformed surface.

Appendix C

AN ESTIMATE OF THE INERTIAL EFFECTS FOR AN ANTIPLANE SHEAR CRACK

An estimate of the inertial effects for a dynamically loaded antiplane shear crack in an elastic-perfectly plastic material is obtained here. It will be shown that for elastic or elastic-plastic materials the asymptotic fields are unchanged by dynamic loading. This estimate is based on an analysis by L.B. Freund [75].

A dynamically loaded antiplane shear crack in an elastic material has the same asymptotic field statically and dynamically, except the stress intensity factor is a function of time for dynamic loading [81], i.e,

$$u_3 = \frac{K_{III}^d(t)}{\mu}\sqrt{\frac{2r}{\pi}}\sin\theta + O(r) \quad ,$$

where $K_{III}^d(t)$ is the mode III stress intensity factor, μ is the elastic shear modulus and (r,θ) are polar coordinates centered at the crack tip. The higher order terms are time dependent and depend on the loading. For a step, plane stress wave loaded crack $K_{III}^d \approx \sqrt{t}$.

Consider an antiplane shear (Mode III) crack in an elastic perfectly plastic material. For small scale yielding conditions, and quasi-static loading, using the geometry of Figure C.1, the solution is given by [82]

$$u_3(x,y) = 2R\frac{\tau_0}{\mu}\sin\theta \quad ,$$

$$\tau_x = -\tau_0\sin\theta$$

$$\tau_y = \tau_0 \cos\theta \quad ,$$

where R is the plastic zone size,

$$R = \frac{1}{2\pi}\left(\frac{K_{III}}{\tau_0}\right)^2 \quad ,$$

K_{III} is the mode III stress intensity factor, τ_x and τ_y are antiplane shear stresses, τ_0 is the yield stress in shear and μ is the elastic shear modulus.

In rate form the solution is

$$v \equiv \dot{u}_3 = 2\dot{R}\frac{\tau_0}{\mu}\sin\theta = \frac{1}{\pi}\frac{K_{III}\dot{K}_{III}}{\tau_0\mu}\sin\theta \equiv V(t)\sin\theta \quad , \tag{C.2}$$

where K_{III} is considered a function of time. The time variation of K_{III} represents the time variation of the loads applied to the body. If $\dot{K}_{III}$ is sufficiently large then the inertial effects must be considered.

Consider now the antiplane shear crack subjected to dynamic loading. The field equations that must be satisfied are (i) the equation of motion

$$\frac{\partial \tau_x}{\partial x} + \frac{\partial \tau_y}{\partial y} = \rho\ddot{u}_3 = \rho\dot{v} \quad , \tag{C.3a}$$

where ρ is the density of the material, (ii) the von Mises yield condition

$$\tau_x^2 + \tau_y^2 = \tau_0^2 \quad , \tag{C.3b}$$

and (iii) the constitutive law

$$\dot{\gamma}_{lx} = \frac{\dot{\tau}_x}{\mu} + \lambda \tau_x \quad , \tag{C.3c}$$

$$\dot{\gamma}_{ly} = \frac{\dot{\tau}_x}{\mu} + \lambda \tau_y \quad ,$$

where $\dot{\gamma}_{lx} = \frac{\partial v}{\partial x}$ and $\dot{\gamma}_{ly} = \frac{\partial v}{\partial y}$. Equation (C.3c) may be rearranged as

$$\frac{\frac{\partial v}{\partial x} - \frac{\dot{\tau}_x}{\mu}}{\tau_x} = \frac{\frac{\partial v}{\partial y} - \frac{\dot{\tau}_y}{\mu}}{\tau_y} \quad . \tag{C.4}$$

Defining ϕ as in Figure C.2, the yield condition (C.3b) can be written as

$$\tau_x = -\tau_0 \sin\phi \tag{C.5}$$

$$\tau_y = \tau_0 \cos\phi \quad .$$

Note that $\phi = \phi(x, y, t)$. Using equation (C.5) the equation of motion (C.3a) can be written as

$$\cos\phi \frac{\partial \phi}{\partial x} + \sin\phi \frac{\partial \phi}{\partial y} + \frac{\rho \dot{v}}{\tau_0} = 0 \quad . \tag{C.6}$$

Similarly equation (C.4) can be written as

$$\cos\phi \frac{\partial v}{\partial x} + \sin\phi \frac{\partial v}{\partial y} + \frac{\tau_0}{\mu} \dot{\phi} = 0. \tag{C.7}$$

Equations (C.6) and (C.7) along with the boundary conditions $\tau_y=0$ on $\theta=\pm\pi$, are a pair of differential equations for $\phi(x, y, t)$ and v(x, y, t).

The quantities ϕ and v can be written as

$$\phi(x,y,t) = \theta+\Delta\phi(x,y,t)$$

$$v(x,y,t) = V(t)\sin\theta+\Delta v(x,y,t) \quad ,$$

that is, ϕ and v are written as the static solutions, equations (C.1) and (C.2) plus dynamic terms. The time derivatives of ϕ and v are

$$\dot{\phi} = \Delta\dot{\phi}$$

$$\dot{v} = \dot{V}(t)\sin\theta+\Delta\dot{v} \approx \dot{V}\sin\theta \quad .$$

Expanding the terms $\cos\phi$ and $\sin\phi$ we can write

$$\cos\phi \approx \cos\theta(1-\frac{\Delta\phi^2}{2}) - \sin\theta(\Delta\phi)$$

$$\sin\phi \approx \sin\theta(1-\frac{\Delta\phi^2}{2}) + \cos\theta(\Delta\phi) \quad .$$

Substitution of the above into equation (C.6) produces an equation for $\Delta\phi$,

$$\frac{\Delta\phi}{r} + \Delta\phi_{,x}\left[\cos\theta-\Delta\phi\sin\theta-\frac{\Delta\phi^2}{2}\cos\theta\right] + \Delta\phi_{,y}\left[\sin\theta+\Delta\phi\cos\theta-\frac{\Delta\phi^2}{2}\sin\theta\right] = -\frac{\rho\dot{V}\sin\theta}{\tau_0} \quad . \tag{C.8}$$

Assuming $\Delta\phi << 1$, the $\Delta\phi^2$ and $\Delta\phi$ terms are neglected in the brackets multiplying $\Delta\phi_{,x}$ and $\Delta\phi_{,y}$, leaving the equation

$$\cos\theta\Delta\phi_{,x}+\sin\theta\Delta\phi_{,y} = \frac{-\rho\dot{V}}{\tau_0}\sin\theta - \frac{\Delta\phi}{r} \quad .$$

This has the solution

$$\Delta\phi = \frac{-\rho\dot{V}r\sin\theta}{2\tau_0} \quad . \tag{C.9}$$

Using equation (C.7) and the same approximations, the equation for Δv is

$$\cos\theta\ \Delta v_{,x}+\sin\theta\ \Delta v_{,y} = -\frac{\tau_0}{\mu}\dot{\phi} + \frac{V\dot{V}\rho\sin\theta\cos\theta}{2\tau_0} \quad ,$$

where $\dot{\phi} = \Delta\dot{\phi} = -\rho\dot{V}r\sin\theta/2\tau_0$. The above equation has the solution

$$\Delta v = \frac{r\rho V\dot{V}}{2\tau_0}\sin\theta\cos\theta + \frac{\rho}{2\mu}r^2\dot{V}\sin\theta \quad . \tag{C.10}$$

Let us estimate the term $\frac{r\rho\dot{V}}{2\tau_0}$. From [82] the crack opening displacement δ is related to the plastic zone size, R, by

$$\delta = 4\gamma_0 R \quad .$$

Assuming that R at fracture initiation is 2 cm, and $\gamma_0 = .005$, δ at fracture initiation is 0.4 mm. Assuming constant acceleration, the estimate $\dot{V} \approx 10^5\ m/s^2$ is obtained. For steel $\tau_0/\rho = \gamma_0\mu/\rho = \gamma_0 C_s^2 \approx 0.5x10^5 m^2/s^2$. Consistent with the assumption of constant acceleration, the term $\dot{V}$ will be negligible. Thus

$$\frac{\Delta v}{V} = \frac{r\rho\dot{V}}{2\tau_0}\sin\theta\cos\theta \approx \frac{r}{50cm}$$

Thus $\frac{\Delta v}{V} < \frac{1}{50}$ if r < 1 cm. Similarly $\Delta\phi < \frac{1}{50}$ if r < 1 cm.

For a plastic zone of 2 cm this analysis shows that the inertial effects are small throughout the plastic zone.

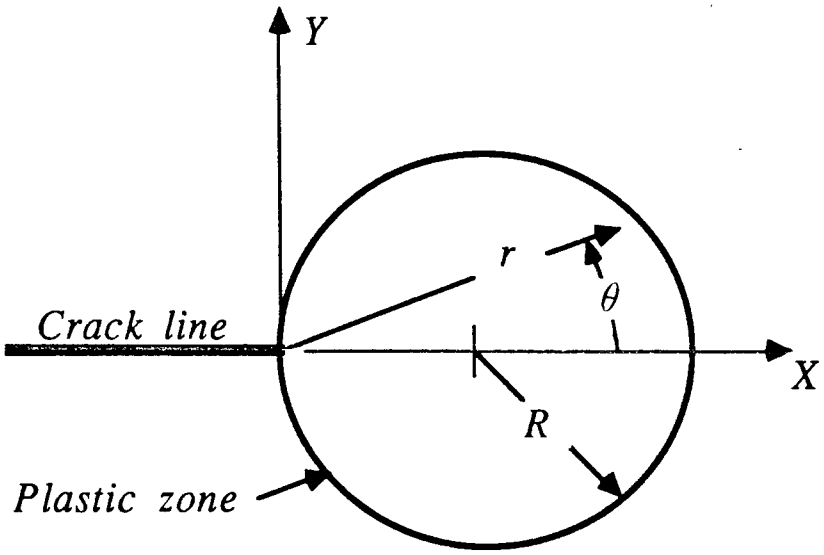

Figure C.1 Antiplane shear crack in elastic-perfectly plastic material.

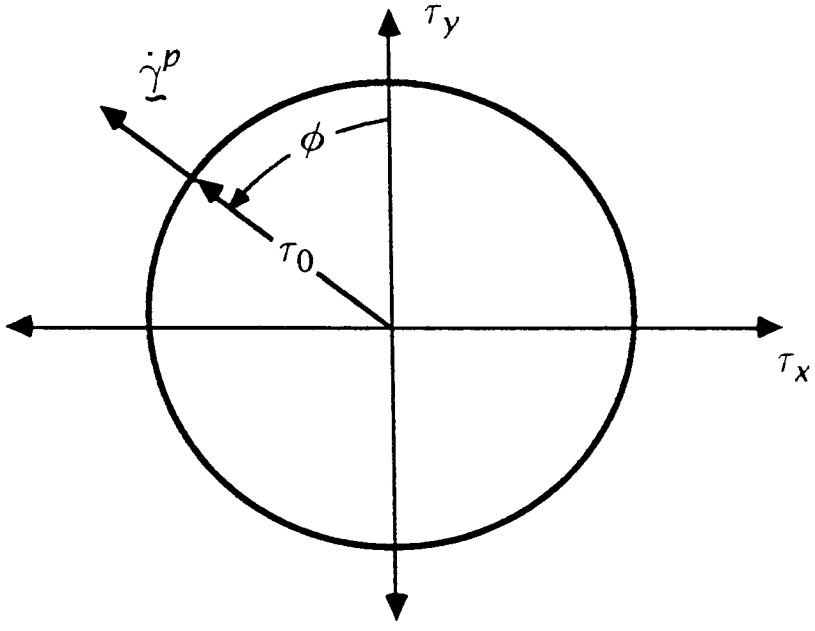

Figure C.2 Yield surface for antiplane shear loading.